Magnetic Transport and Bose-Einstein Condensation of Rubidium Atoms

Benjamin Thomas Sheard

A thesis submitted in partial fulfilment of
the requirements for the degree of
Doctor of Philosophy at the University of Oxford

Merton College
University of Oxford
Trinity Term 2010

Abstract

Magnetic Transport and Bose-Einstein Condensation of Rubidium Atoms

Benjamin Thomas Sheard, Merton College, Oxford University
D.Phil. thesis, Trinity Term 2010

This thesis describes the design, construction and optimisation of a new apparatus to produce Bose-Einstein condensates (BECs) of ^{87}Rb atoms. The main aim in building this system was to include a high resolution imaging system capable of resolving single atoms. Optical access for the imaging system was created by including a stage of atom transport in which the atoms are magnetically transferred $\sim 50\,\mathrm{cm}$ from a magneto-optical trap (MOT), where they are initially collected, to a glass science cell where experiments are carried out and imaging takes place. Two magnetic transport schemes have been demonstrated, based on approaches first used in other laboratories. First, a scheme in which the atoms are transferred in a moving pair of magnetic trapping coils. Second, a hybrid scheme where the atoms are translated part of the distance in the moving coils, and the rest of the way by switching the current in a chain of fixed coils. This second scheme was designed to allow optical access for a high numerical aperture microscope objective to be placed immediately next to the science cell for high resolution imaging.

The atoms were first collected in a large pyramid MOT which can be loaded with 3×10^9 atoms in a time of 20 s. Around half of these atoms – those in the $|\mathrm{F} = 1, m_F = -1\rangle$ magnetic substate – were then magnetically trapped prior to transport. The typical fraction of the trapped atoms transferred to the science cell was $\sim 30\%$ and $\sim 18\%$ for the moving coils and hybrid schemes respectively.

Evaporative cooling was carried out on the atom cloud following transport with the moving coils and loading into a time-orbiting potential trap. The optimised cooling sequence lasted for 28 s and consistently produced a pure condensate with 5×10^5 atoms. A BEC has also been produced by evaporative cooling following hybrid transport. The next experimental steps will be to optimise the hybrid transfer approach further and install the high resolution imaging system.

The system is well-placed to continue an ongoing series of experiments in which ultracold atoms are trapped in RF-dressed potentials. These potentials will be used to study low-dimensional quantum gases as well as in experiments where small atom number BECs are rapidly rotated to enter the fractional quantum Hall regime.

Acknowledgements

I would firstly like to thank my supervisor, Prof. Chris Foot, for giving me the opportunity to work in the fascinating field of ultracold atoms. I have greatly appreciated his patient guidance and the time he has always taken to offer me advice and answer my questions.

I am also very much indebted to the other members of the group I've had the privilege to work with. First, to Will Heathcote and Eileen Nugent who introduced me to the workings of the original -174 experiment. Eileen has also been able and willing to answer pretty much every question I asked her in her latest role as postdoc.

On the new experiment, I was very fortunate to be working with such a motivated and talented crew. Ben Sherlock and Marcus Gildemeister have both brought enormous skill and energy to the lab while being great company. And Ed Owen continues this trend. I wish them many Lab Whisky-worthy successes in the coming months! Thanks as well to our postdocs Marcin Kubasik and Dave Crosby for providing invaluable experience and assistance. I am also grateful to the two visiting summer project students, Gerhard Zürn and Rémi Blandino, who helped in the construction of the apparatus.

Other current and past group members have helped me in various ways and made the basement a relaxed and friendly place to work in – thanks to Ben Fletcher, Ross Williams, Giuseppe Smirne, Sarah Al-Assam, Amita Deb, Min Sung Yoon, Herbert Crepaz, Rachel Godun, Andrian Harsono, Dmitris Trypogeorgos and Martin Shotter. Thanks as well to Duncan England and Dave McCabe for keeping the sabotage merely whimsical.

I would also like to thank Dr. Simon Cornish at Durham University for generously allowing me to visit his group on two occasions.

On the technical side, big thanks to Graham Quelch for his help with various aspects of the experiment and for keeping things in the basement in good working order. I am grateful to Mike Tacon and Simon Moulder in the physics workshops for all their assistance in getting the various bits for the new apparatus made. Also, Rob Harris gave me a great deal of valuable advice and assistance in the research workshop.

My friends in Oxford have made the time here a special one. Thanks to Nick, Patrick, Artemis, George and Benoit & Jess for the good times. And a special thank you to Linda for her amazing support during my thesis writing months.

Finally, I would like to dedicate this thesis to my family for their constant love and encouragement throughout my studies.

Contents

List of Figures

List of Tables

Chapter 1

Introduction

The development of atomic physics has been driven by ever-increasing control over atoms and by the ever more precise measurements performed upon them. The interplay of these two advances has resulted in modern atomic physics experiments in which the degrees of freedom of atoms can be controlled to an extremely high level, and in which measurements on single atoms can be carried out. These advances in the control of atoms culminated in the production in 1995 of the first dilute gas Bose-Einstein condensate (BEC), a state of matter in which all atoms are in the ground energy state. The atoms in a BEC are described by a common, many-body, macroscopic wavefunction and thus have superfluid properties. As such, BEC in dilute gases represents a crossover between atomic physics and condensed matter physics and offers a controlled and theoretically accessible system from which insights into condensed matter counterparts such as superfluid helium and superconductors may be gained.

In the following, a brief historical overview is given of the development of the cooling and trapping techniques that led to the production of a BEC. This

concludes with a discussion of the latest trapping techniques that may be used to go beyond the mean-field regime and study systems of strongly correlated bosons. The plan for implementing these techniques in the new apparatus is then outlined. Finally, an outline of the rest of the thesis is given.

Historical Overview

The early development of atomic physics in the first thirty years of the last century is closely linked to that of quantum mechanics, and the experiments performed during that period confirmed the inherently quantum mechanical nature of atoms and characterised their gross structure. In the 1940s and 1950s, more sophisticated experiments used radio-frequency spectroscopy of atoms in beams to probe fine and hyperfine structure in the atom. Explanation of this new structure necessitated the development of quantum electrodynamics, a theory which still provides the most accurate description of the atom available. In addition, these new high precision measurements gave rise to the caesium atomic clock, which became a new standard in precision time-keeping.

Further progress in studies of atoms required more precise control over their degrees of freedom. More specifically, it was necessary to control the internal degrees of freedom: the magnetic spin state and electronic configuration, and the external degrees of freedom: the position and momentum of the atom.

In 1953, Kastler gave the first demonstration of control over the internal states of atoms by optically pumping a collection of atoms into a single, common magnetic substate and then inducing a transition of the atoms to a different substate(s) by applying radio-frequency radiation [1]. During a similar period, Paul was carrying out experiments to control the external degrees of freedom by guiding and focussing ions using electric and magnetic fields. This culminated in the development of the

Paul trap which uses a combination of DC and AC electric fields to confine ions tightly [2]. This work was built upon some years later to produce traps for neutral atoms using static magnetic fields [3].

Alongside these developments in magnetic trapping, another key development for controlling both the internal and external degrees of freedom of atoms was the advent of the laser in 1960 [4]. The development of widely-tunable lasers allowed Doppler-free spectroscopy, increasing precision in the measurement of spectral line frequencies by removing the Doppler line-broadening associated with traditional spectroscopy [5]. Studies using intense laser fields and magnetic traps allowed more accurate fundamental measurements of atomic structure.

In the 1970s it was proposed that the radiation force of light could be used to cool and trap atoms [6, 7]. With the significant increase in light intensity afforded by lasers this already well-known force was now strong enough to be used to reduce the velocity, and thus temperature, of room temperature atoms by several orders of magnitude. The first demonstration of laser cooling of atoms was made by Phillips and Metcalf in 1982 when they slowed a beam of sodium atoms in one dimension using a counter-propagating laser beam and a spatially varying magnetic field, in so-called Zeeman slowing [8]. Following this, in 1985, Chu *et al* demonstrated 3D cooling of sodium atoms using three pairs of counter-propagating laser beams [9]. Atoms were cooled at the intersection of the beams in 'optical molasses', so named because of the analogous nature of the radiation force and traditional mechanical frictional forces. Additional sub-Doppler cooling mechanisms were found to be present in optical molasses, leading to temperatures on the order of 10μK. The addition of a quadrupole magnetic potential centred on the intersection of the optical molasses laser beams allowed the laser-cooled atoms to be trapped in what has become the starting point for almost all ultracold atomic physics experiments:

the magneto-optical trap (MOT) [10]. The MOT allows over 10^{10} atoms to be cooled from room temperature to the microkelvin range purely by radiative forces.

These rapid developments in atom trapping and cooling have allowed the realisation of a long-standing goal in the atomic physics community: the creation of a Bose-Einstein condensate (BEC) in a low density vapour. Bose-Einstein condensation is the macroscopic occupation of the ground energy state of a system of bosonic particles, first predicted by Bose in 1924 for a system of photons [11]. Later, in 1925, Einstein extended this prediction to an ideal gas of bosonic atoms [12]. The transition to BEC occurs when the phase space density of the system is increased to the point where the de Broglie wavelength of the atoms becomes larger than the interatomic separation. The atoms are then described by a single macroscopic wavefunction. The BEC transition is unusual in that it arises purely from the quantum statistics of bosons which follow from their indistinguishable nature, and is predicted to occur even in the absence of interatomic interactions.

The interest in Bose-Einstein condensation stemmed from the understanding that it was the underlying phenomenon responsible for other macroscopic quantum mechanical phenomena of interest such as superfluidity and superconductivity. However, whilst these phenomena had been studied for some time in condensed matter systems, the strong inter-particle interactions in these systems precluded their accurate theoretical modelling. By contrast, a dilute gas BEC is weakly-interacting and can therefore be accurately modelled using mean-field theory. This makes it an ideal test-bed for studies of many-body theory and superfluidity.

Initial experimental efforts focused on Bose-condensing spin-polarised hydrogen, however it was in the parallel field which employed dilute alkali metal vapours that Bose-Einstein condensation was first achieved using the new techniques of laser cooling and magnetic trapping. BEC was achieved in dilute vapours of ru-

bidium, sodium, and lithium in close succession [13–15]. Since then, BEC has been achieved in several other bosonic elements, and 2003 saw the creation of both a molecular condensate composed of bound fermionic atoms [16] and a fermionic condensate composed of correlated pairs of fermions [17].

In the fifteen years since the creation of the first BEC many studies have been carried out on the collective modes and superfluidity of BECs, and confirmed that mean-field theory provides a very accurate description in such weakly-interacting regimes. Following this thorough study of the mean-field regime, the increasing trend in cold atom research is towards the study of strongly correlated states analogous to the strongly correlated states in superfluids and superconductors. Mean-field theory is no longer sufficient to model these states, for which a true many-body description is necessary. However, the interatomic interactions are still sufficiently weak to make theoretical calculations possible, something that is not true for the condensed matter counterparts.

Many-Body Physics

Recently, several new techniques for trapping atoms have been developed that allow entry into regimes where the interactions between the atoms can no longer be considered weak and where mean-field theory must be replaced with a true many-body theory. Central among these techniques is optical dipole trapping in which atoms are trapped by forces arising from the gradient of the light shift. This technique gives increased confinement over standard magnetic trapping, and allows one to freeze out directions of atom motion to produce effectively 2D or 1D quantum gases which exhibit markedly different properties to the 3D case. Interfering optical dipole trapping beams in three dimensions gives rise to an *optical lattice* – a crystal-like array of optical potentials in which single atoms can be

trapped. Such potentials give the ultimate control over the external degrees of freedom of individual atoms, with all atoms in their ground state and located at precise, distinct points in space. By controlling the separation and depth of the separate potential wells in the optical lattice, the strongly correlated Mott insulator state can be engineered, in which the atom number per site tends to an exact integer value throughout the lattice [18].

Strongly correlated states also arise in rapidly rotating condensates. Mathematically, a rapidly rotating BEC is directly analogous to a two-dimensional electron gas in a strong magnetic field. In such a system, at sufficiently fast rotation rates (that is, at rotation frequencies $> 99\%$ of the radial trapping frequency), the atoms enter into a series of strongly correlated states analogous to the fractional quantum Hall regime observed in semiconductors. In this regime, fractionally charged quasi-particle charge carriers emerge from the many-body description without being postulated *a priori*, giving rise to a rich array of new physics.

Another recent method of trapping atoms is to use a radio-frequency (RF) field to dress static magnetic potentials. The resulting adiabatic RF-dressed potentials can take on a large array of different geometries, and can be morphed adiabatically by dynamically changing the trapping parameters. RF-dressing was used in an earlier apparatus in this group to produce toroidal [19, 20] and ellipsoidal [21] potentials for ultracold atoms. The increased trapping frequencies afforded by these potentials allows entry into the quasi 1D and 2D trapping regimes, which offers the possibility of studying the superfluid properties in these regimes.

New Apparatus

The key feature in the new apparatus design is a high resolution imaging system. This was designed with two principal experiments in mind. First, the continuation

of the series of experiments using RF-dressed potentials begun in the old apparatus. The intention is to use RF-dressed potentials in the new apparatus to study the superfluid properties of low dimensional systems. The second planned experiment involves rapidly rotating a small cloud of atoms to enter into the strongly correlated, fractional quantum Hall regime described above. The proposed trapping potential that will be used in this experiment is the TAAP trap that combines RF-dressing with time-averaging. High resolution imaging facilitates both these experiments by allowing the direct imaging of the necessarily small atom numbers, and small condensate features such as vortices. In order to create the optical access required for the imaging system, the experiment was designed to include a stage of atom transport. This approach was pioneered in Munich, in the first optical lattice experiments [22], and has become common in the latest generation of experiments where greater optical access is required. In addition to requiring better imaging, the proposed experiments necessitated an improved set of magnetic trapping coils at the site of BEC production. This will increase the accessible parameter space for RF-dressing experiments.

Thesis Outline

This thesis is structured as follows. Chapter 2 introduces some of the background theory of laser cooling and magnetic trapping and concludes with a theoretical description of the phenomenon of Bose-Einstein condensation. This is followed in chapter 3 by an overview of the theory of RF-dressed potentials for ultracold atoms, and a discussion of the physics that we intend to study using these potentials. Chapter 4 contains a discussion of the design criteria for the new apparatus, and an overview of the important physical considerations in implementing a system for transporting atoms. The technical details of this new apparatus are then presented

in chapter 5. Chapter 6 reports the optimisation of the magneto-optical trap and atom transport stages of the experiment, and chapter 7 the optimisation of the evaporative cooling ramps used to cool the atoms to produce a BEC. Finally, in chapter 8 conclusions are drawn about the new apparatus and the outlook for future experiments is discussed.

Chapter 2

Laser Cooling, Magnetic Trapping and BEC theory

This chapter contains the theoretical basis of the techniques used to cool and trap atoms in the experiment. First, an overview of laser cooling is given, leading to a description of the magneto-optical trap that is used to trap and cool atoms from a room temperature vapour to the 100 μK temperature range. This is followed by an overview of the purely magnetic trapping that is used to contain the atoms in the further cooling stages which are used to reach the Bose-Einstein condensation transition temperature. A theoretical description of the phenomenon of Bose-Einstein condensation is then given.

2.1 Laser Cooling

2.1.1 Light-Atom Interaction

The force of radiation on matter was predicted by Maxwell's classical theory of electromagnetic radiation and was confirmed experimentally at the beginning of the twentieth century [23, 24]. Further understanding of this interaction of radiation with matter was gained from the Bohr model of the atom and then from Einstein's phenomenological treatment of absorption and emission of radiation by atoms.

The dynamics of a two-level atom in a near-resonant light beam can be understood using a semi-classical model that treats the energy of the atom as quantised and the light as a classical electric field [25]. The oscillating electric field couples the two atomic energy levels resulting in transfer of population between ground and excited states at a characteristic frequency, the Rabi frequency. In addition to its effect on the atomic level populations the light produces a shift in the energy of these levels referred to as the light shift (or a.c. Stark shift). This light shift arises from the interaction of the electric field of the light with the induced electric dipole of the atom, and changes the energy of the levels of the atom by:

$$\Delta_{light} = \frac{\hbar\Omega^2}{4\delta} \tag{2.1}$$

where Ω is the Rabi frequency for transitions between the ground and excited states; and $\delta = \omega - \omega_0$ is the frequency detuning of the light, of angular frequency ω, from the atomic resonance frequency, ω_0. It is assumed that $|\delta| \gg \Gamma$, where Γ is the natural linewidth of the upper level of the atom. The sign of the light shift depends on the detuning: for $\delta < 0$ it is positive for the excited state and negative for the ground state. A full treatment of the light-atom interaction, including spontaneous emission, requires quantum electrodynamics [26].

The radiation forces on atoms can be divided into two categories: dissipative forces involving spontaneous emission such as the scattering force on atoms in a near resonant light beam, and the dipole forces arising from the gradient of the light shift. For a large frequency detuning the dipole force is conservative, but closer to resonance there arise the so-called Sisyphus mechanisms for an atom moving through a standing wave that involve dissipation and light shifts.

The scattering force produces a radiation pressure on the atom which can be understood from the conservation of momentum as follows. An atom in a beam of near-resonant light will be excited through the absorption of a photon and receive a momentum kick equal to $\hbar k$ in the direction of propagation of the light beam, where $k = 2\pi/\lambda$ is the wavenumber of the photon of wavelength λ. The subsequent relaxation of the atom results in the spontaneous emission of a photon in a random direction. The atom receives a momentum kick equal and opposite to the momentum of the emitted photon. The isotropic nature of the emission means that over many scattering cycles these momentum kicks average to zero. Thus, the effect of many scatterings is to produce a net force on the atom in the direction of propagation of the light beam. The magnitude of this scattering force on an atom in a single light beam is given by the rate at which momentum is imparted to the atom:

$$\mathbf{F_s} = \hbar \mathbf{k} R_s \tag{2.2}$$

where R_s is the scattering rate of the atom, which for a two-level atom has the Lorentzian form [27]:

$$R_s = \frac{\Gamma}{2} \frac{\Omega^2/2}{\delta^2 + \Omega^2/2 + \Gamma^2/4} = \frac{\Gamma}{2} \frac{I/I_{sat}}{1 + I/I_{sat} + 4\delta^2/\Gamma^2} \tag{2.3}$$

where I_{sat} is the saturation intensity of the transition.

The width of R_s is set by the power-broadening of the upper level in the atom, and is thus approximately equal to the natural linewidth of this level, Γ. The natural linewidth (FWHM) of the $5^2S_{1/2}$ to $5^2P_{3/2}$ transition in ^{87}Rb, $\Gamma \sim 2\pi \times 6.1\,\text{MHz}$. For the scattering force to be significant the linewidth of the light must be less than this value. In addition, the light must be sufficiently intense to give a non-neglible value for I/I_{sat}. These conditions were only met with the advent of narrow-band tunable lasers in the 1970s. In 1975, Hänsch and Schawlow and independently Wineland and Dehmelt proposed that such a light source could be used to cool atoms and ions respectively [6, 7]. This Doppler cooling scheme is outlined below.

2.1.2 Doppler Cooling

The distribution of atom velocities in a classical ensemble is given by the Maxwell-Boltzmann distribution. The theorem of equipartition of energy states that the atoms' thermal energy is equal to their translational energy, giving the following relation between the root-mean-squared atom velocity, v_{rms}, and the temperature, T:

$$\frac{3}{2}k_BT = \frac{1}{2}mv_{rms}^2 \tag{2.4}$$

where k_B is Boltzmann's constant, and m is the atomic mass. In a 3D gas, the root-mean-squared velocity relates to the mean velocity, $\bar{v}$, as: $v_{rms} = \sqrt{\frac{3\pi}{8}}\bar{v}$. Therefore, reducing the average temperature of the atoms is equivalent to reducing their average velocity. In terms of the Maxwell-Boltzmann distribution this corresponds to reducing the width of this distribution about zero velocity.

In Doppler cooling, the scattering force given in equation 2.2 is used to reduce the average atom velocity and temperature. The key point to achieving this reduction is to use a *negative* value for detuning in equation 2.3 (that is, laser light

which is *red*-detuned relative to the atomic transition). The scattering force then has the required dissipative form.

Consider an atom moving in two counter-propagating, red-detuned beams of light. The atom sees the light it is moving towards Doppler-shifted toward resonance, and therefore preferentially absorbs photons from this beam. With each absorption the atom receives a momentum kick of magnitude $\hbar k$ in the direction opposing its motion. The subsequent spontaneous emission occurs in a random direction and therefore over many absorption-emission cycles its effect on the atom's momentum averages to zero. Thus, the light beams produce a net slowing force on the atom which cools it along the direction of propagation of the laser beams. In the limit of small intensity, $I/I_{sat} \ll 1$, the force of each beam on the atom can be considered independent, so that the total force on the atom is just the sum of these forces:

$$\mathbf{F_{1D}} = \hbar\mathbf{k}\frac{\Gamma}{2}\left[\frac{I/I_{sat}}{1+I/I_{sat}+4(\delta-\mathbf{k}\cdot\mathbf{v})^2/\Gamma^2}\right] - \hbar\mathbf{k}\frac{\Gamma}{2}\left[\frac{I/I_{sat}}{1+I/I_{sat}+4(\delta+\mathbf{k}\cdot\mathbf{v})^2/\Gamma^2}\right]. \tag{2.5}$$

In the limit of small velocity, $kv \ll \Gamma$, $\mathbf{F_{1D}}$ can be approximated by:

$$\mathbf{F_{1D}} \simeq -\alpha\mathbf{v} \tag{2.6}$$

where

$$\alpha = -4\hbar k^2 \frac{I}{I_{sat}} \frac{2\delta/\Gamma}{[1+I/I_{sat}+4\delta^2/\Gamma^2]^2}. \tag{2.7}$$

With red-detuned light, $\alpha > 0$, the force has the same dissipative form as that of a particle in a viscous medium. The variation of $\mathbf{F_{1D}}$ with atom velocity is shown in figure 2.1. In addition to this dissipative force the atoms experience smaller forces which arise from the stochastic nature of photon absorption and emission

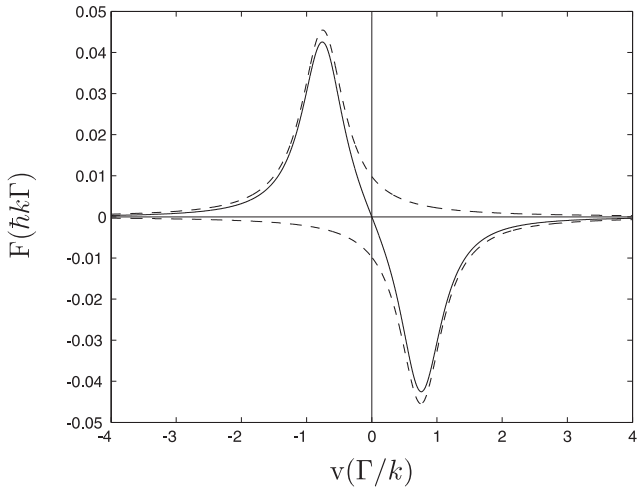

Figure 2.1: The Doppler force on an atom in a counter-propagating pair of laser beams versus atom velocity for: $I/I_{sat} = 0.1$ and $\delta = -\Gamma$. The dashed lines show the forces from each beam and the solid line shows the sum of these two forces.

and produce a momentum diffusion of the atoms. The balance of the cooling and heating forces results in a lower limit to the final temperature attainable through Doppler cooling alone. In the low intensity limit, $I/I_{sat} \ll 1$, this minimum temperature, the Doppler limit, T_D, is given by [27]:

$$k_B T_D = \frac{\hbar\Gamma}{2}, \tag{2.8}$$

which is obtained when $\delta = -\Gamma/2$. For the $|\mathrm{F}' = 3\rangle$ state of ^{87}Rb, T_D is equal to $146\,\mu$K.

In the above two laser beam example, cooling of the atoms takes place along only one direction: the axis of propagation of the beams. However, a cloud of atoms has an isotropic three-dimensional distribution of velocities, and therefore must be cooled in all three dimensions. This can be achieved by using three orthogonal pairs of counter-propagating laser beams centred upon the atoms (as shown in figure 2.2 (a)). This configuration is referred to as 'optical molasses' because the atoms' dynamics in the resulting light field is analogous to that of particles in a viscous

fluid. The optical molasses configuration was first demonstrated by Chu *et al* in 1985 [9]. Later studies showed that the behaviour of atoms in optical molasses cannot be completely described by the Doppler cooling picture, and additional sub-Doppler cooling mechanisms must be invoked to account for observations.

2.1.3 Sub-Doppler Cooling

Early studies of atoms in optical molasses found that the atom dynamics could not be completely described by the Doppler picture discussed above. In particular, the measured temperature of the atoms was considerably lower than the predicted Doppler temperature when the external magnetic field in the vicinity of the atoms was small ($B < 0.1\,\mathrm{G}$) [28, 29]. This shortcoming of the Doppler theory is due to the fact that it does not take into account the multiple levels of the atom or the polarisation gradients created by the interfering beams. In any 3D configuration of overlapping laser beams, such as the optical molasses configuration, there will always exist polarisation gradients. When these features are taken into consideration new, sub-Doppler cooling mechanisms arise [30, 31]. The predicted temperature limit of these cooling processes matches very well the typical temperatures observed in experiments with optical molasses [29].

The exact form of the sub-Doppler cooling mechanisms present in optical molasses depends on which polarisations are used for the counter-propagating laser beams. Typically one of two configurations is used. The first employs orthogonal linearly polarised beams (lin$\perp$lin), and the second orthogonal circularly polarised beams ($\sigma^+ - \sigma^-$). In both cases the polarisation of the resulting light field varies in space: for lin$\perp$lin the ellipticity changes periodically in space, and for $\sigma^+ - \sigma^-$ the polarisation is everywhere linear but the direction of the electric field vector changes in space. These two configurations provide cooling by different mecha-

nisms. In many experiments with cooling in more than one dimension, the relative phase between counter-propagating beams is not fixed and so the light field contains all types of polarisation and therefore both mechanisms can occur [32].

In the lin⊥lin configuration atoms are cooled by the Sisyphus mechanism; this arises when the coupling strengths between the various atomic sublevels vary as the atom moves through the light field. This variation in coupling is brought about by the changing ellipticity of polarisation of the light field in space, and leads to the spatial variation of two further atomic properties. First, the populations of the atomic ground state sublevels vary in space. Second, the light shifts of the various sublevels in the atom are different at different points in space. For an atom such as ^{87}Rb (with nuclear spin, $I = 3/2$) with a ground state momentum, $J = 1/2$, the light shifts of the $m_F = \pm 1$ sublevels are equal and opposite at all points. The resulting sublevel potentials are sinusoidal, reflecting the periodic ellipticity of the light fields, and 180° out of phase with each other.

The spatial variation in the light shift and the ground state populations conspires to cool moving atoms in the following way. Atoms moving through the light field at a rate that is fast compared to their optical pumping rate cannot adjust their internal state to the changing form of the light field, which leads to a change in the atoms' potential energy as they move on the sinusoidal potentials. Atoms with a particular velocity range will tend to climb the hills of this potential in the time between optical pumping cycles. In the lin⊥lin configuration the light shifts and the optical pumping rates of the different magnetic sublevels are correlated such that atoms are more likely to be optically pumped when at the top of one of these potential hills into the potential valley formed by the other ground state sublevel. The energy of the spontaneously emitted photon is then larger than that of the absorbed photon by an amount equal to the kinetic energy lost by the atom

in climbing the potential hill. As this cycle is repeated the kinetic energy of the atoms is progressively radiated away as photon energy. This dissipative mechanism is active for the typical atom velocities given by Doppler cooling, and hence will automatically take over from Doppler cooling when temperatures on the order of the Doppler limit are reached. The minimum temperature given by the Sisyphus mechanism is achieved when the kinetic energy of the atoms is no longer sufficient to allow them to climb the hills of the potential, and is therefore on the order of the light shift of the atoms' sublevels.

In the $\sigma^+ - \sigma^-$ configuration the polarisation is everywhere linear so the light shift of the magnetic sublevels of the atom does not vary in space, which means that Sisyphus cooling cannot occur. A different cooling mechanism, referred to as *motion-induced orientation*, arises from a combination of the optical pumping between different sublevels and the rotation of the optical electric field vector in space [30]. The combination of these results in an imbalance in the ground state populations of an atom moving through the light field. This leads to preferential absorption of photons from the laser beam whose direction of propagation opposes the atom's motion. The atom is cooled since the absorbed photon has an energy which is lower than that of the emitted photon due to the Doppler shift produced by the atom's velocity.

The sub-Doppler cooling mechanisms outlined above produce a much stronger damping of the atomic motion than that given by the Doppler cooling mechanism. This damping cools the atoms to a final temperature set by the relationship:

$$T \propto \frac{I}{|\delta|}. \tag{2.9}$$

This relationship reflects the dependence of Sisyphus cooling on the light shift of the atom. A limit to sub-Doppler cooling is set by the momentum recoil from a

single photon. The resulting lowest attainable temperature, the recoil temperature, T_R, is given by:

$$k_B T_R = \frac{\hbar^2 k^2}{m}. \tag{2.10}$$

Typical final temperatures observed in experiments with optical molasses are approximately an order of magnitude larger than T_R ($T_R \sim 362\,\mathrm{nK}$ in $^{87}\mathrm{Rb}$) in agreement with the predictions of sub-Doppler theory [33].

In addition to its dependency on the parameters of the light field, the final temperature in optical molasses is also very sensitive to the presence of static magnetic fields [29]. At magnetic field strengths of between approximately 0.1 and 1 G the Zeeman shift of the ground state sublevels becomes approximately the same as their light shift. In addition, at these field strengths the Larmor precession frequency of the atom is of the same order as the optical pumping rate [34]. These two effects result in the suppression of the sub-Doppler cooling mechanisms described above so that the final temperature of the molasses increases with increasing magnetic field. At field strengths that give a Zeeman shift equal to the light shift of the atom, sub-Doppler processes can no longer take place and the molasses temperature is on the order of the Doppler limit [29].

Larger magnetic fields also limit the final temperature given by the Doppler cooling mechanism. The atoms tend to be cooled toward a finite velocity for which the Doppler shift of the light is equal to the Zeeman splitting of the excited state of the atom. This minimum velocity becomes larger as the magnetic field is increased resulting in increasing cloud temperatures above the Doppler limit [35].

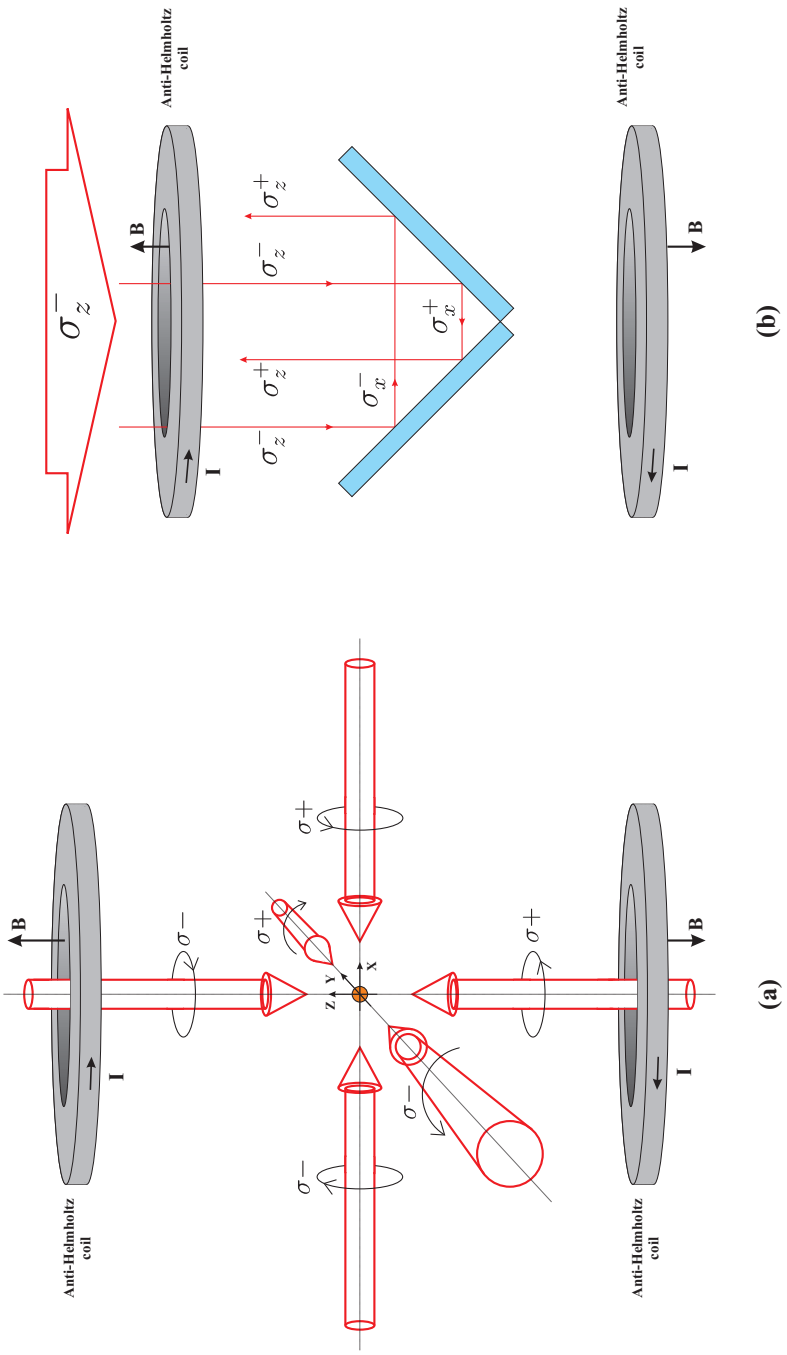

Figure 2.2: The configurations of a) a standard 6-beam MOT and b) the pyramid MOT used in the experiment in this thesis.

2.2 Magneto-Optical Trap

2.2.1 Principle of Operation

The optical molasses configuration provides efficient atom cooling but does not provide atom confinement. The atoms' momentum diffusion means that they eventually diffuse out of the region of overlap of the laser beams and are lost. A solution which provides this necessary confinement is the magneto-optical trap (MOT), which was first demonstrated in 1987 [10]. In the MOT a spherical quadrupole field is added to the 3D optical molasses configuration, with the centre of the field positioned at the intersection of the six trapping beams. The $\sigma^+ - \sigma^-$ configuration is used for the laser beams. The standard MOT configuration uses six individual MOT beams as for 3D molasses (figure 2.2 (a)). In the experiment in this thesis an alternative arrangement – the pyramid MOT – is used. In this form of the MOT, first demonstrated by Lee *et al*, the six individual MOT beams are formed by the reflections of one large beam from the inside faces of an inverted pyramid (figure 2.2 (b)) [36]. Further details of the pyramid MOT design and construction are given in section 5.3.

The principle of the MOT is illustrated in figure 2.3. For small displacements from the field centre, the magnitude of the quadrupole field increases linearly with distance in all directions. The result is that the energies of the Zeeman sublevels of the excited state increase linearly, as shown in figure 2.3 for one dimension. The selection rules for transitions between Zeeman substates dictate that the σ^+ (σ^-) beam can only excite transitions to the $\mathrm{M_e} = +1$ ($\mathrm{M_e} = -1$) excited substate from the $M_g = 0$ ground state. Thus, an atom at negative (positive) positions in figure 2.3 scatters more photons from the σ^+ (σ^-) beam and feels a net force moving it towards the trap centre. This restoring force, originating purely from radiation

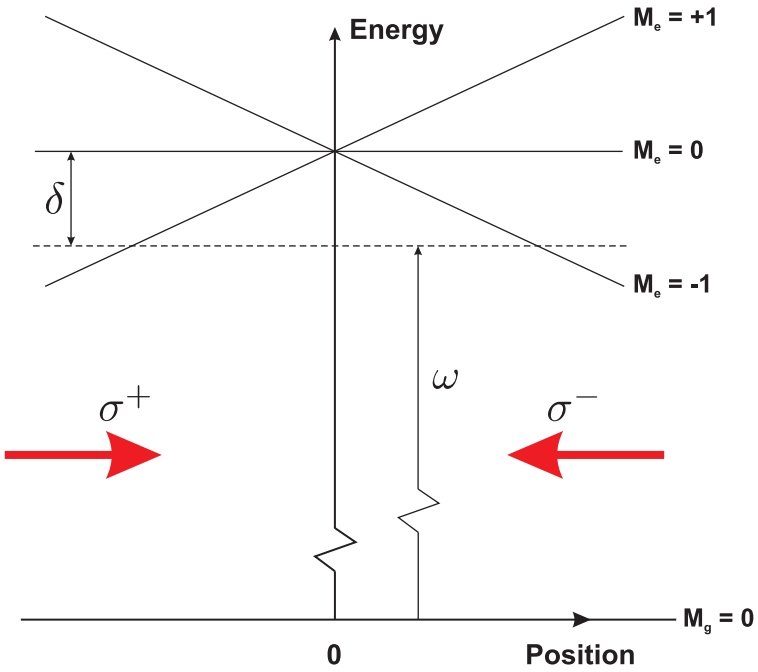

Figure 2.3: Schematic showing the operation of the magneto-optical trap. For simplicity a $J = 0$ to $J = 1$ transition is shown, with M_e and M_g referring to the excited and ground states respectively. The inhomogeneous quadrupole magnetic field splits the excited state energy levels away from the origin resulting in the preferential absorption by an atom of light from the beam travelling toward to trap centre. This creates a restoring force on the atoms.

pressure, acts in addition to the Doppler cooling force given in equation 2.6. The net force on the trapped atoms is then given by:

$$\mathbf{F_{MOT}} = -\alpha\mathbf{v} - \frac{\alpha\beta}{k}\left(\frac{x}{2}\hat{\mathbf{e}}_x + \frac{y}{2}\hat{\mathbf{e}}_y + z\hat{\mathbf{e}}_z\right) \tag{2.11}$$

where β is the Zeeman shift of the atom: $\beta = \frac{g_e \mu_B B'_q}{\hbar}$, in which g_e is the Landé factor for the excited state and B'_q is the axial gradient of the magnetic field.

The energy level scheme used in the laser cooling of ^{87}Rb in the experiment is shown in figure 2.4. The $|\mathrm{F} = 2\rangle \rightarrow |\mathrm{F}' = 3\rangle$ transition is used as the cooling transition. This transition is suited to laser cooling since it is a closed, cycling transition. During laser cooling of the atoms in the $|\mathrm{F} = 2\rangle \rightarrow |\mathrm{F}' = 3\rangle$ cycle there is a small probability of off-resonant excitation to the $|\mathrm{F}' = 2\rangle$ state from where the

atoms can decay to the $|\mathrm{F}=1\rangle$ ground state. This process will eventually place all of the atoms into the $|\mathrm{F}=1\rangle$ dark state. To prevent this, the atoms are illuminated with a small amount of 'repumping' light, resonant with the $|\mathrm{F}=1\rangle \rightarrow |\mathrm{F}'=2\rangle$ transition, which pumps the atoms into the $|\mathrm{F}'=2\rangle$ state from where they can decay into the $|\mathrm{F}=2\rangle$ ground state and return to the cooling cycle.

2.2.2 MOT Atom Number and Phase Space Density

The aim in the MOT is to capture as many atoms as possible and then to maximise the phase space density to give the optimum conditions for the subsequent magnetic trapping of the atom cloud. An expression for the steady-state atom number in the MOT can be found by considering the balance between the loading of atoms into the MOT and atom losses from the trap caused by collisions with atoms in the background vapour. Modelling the MOT loading as linear in time gives a rate equation of the following form [37]:

$$\frac{dN(t)}{dt} = a - b\,N(t) \tag{2.12}$$

where N is the trapped atom number, a is the constant loading rate, and b is the loss rate. Note, here the intra-trap, 'cold collisions' have been neglected, which assumes a low atom density. The solution to this rate equation is:

$$N(t) = \frac{a}{b}(1 - \exp[-bt]) \tag{2.13}$$

for which the steady-state value of N, $N_s = a/b$.

The constant loading rate, a, can be estimated by considering the rate at which atoms enter the the trapping volume of the MOT produced by the region of overlap of the six MOT beams. The rate, R, at which atoms with a velocity between v

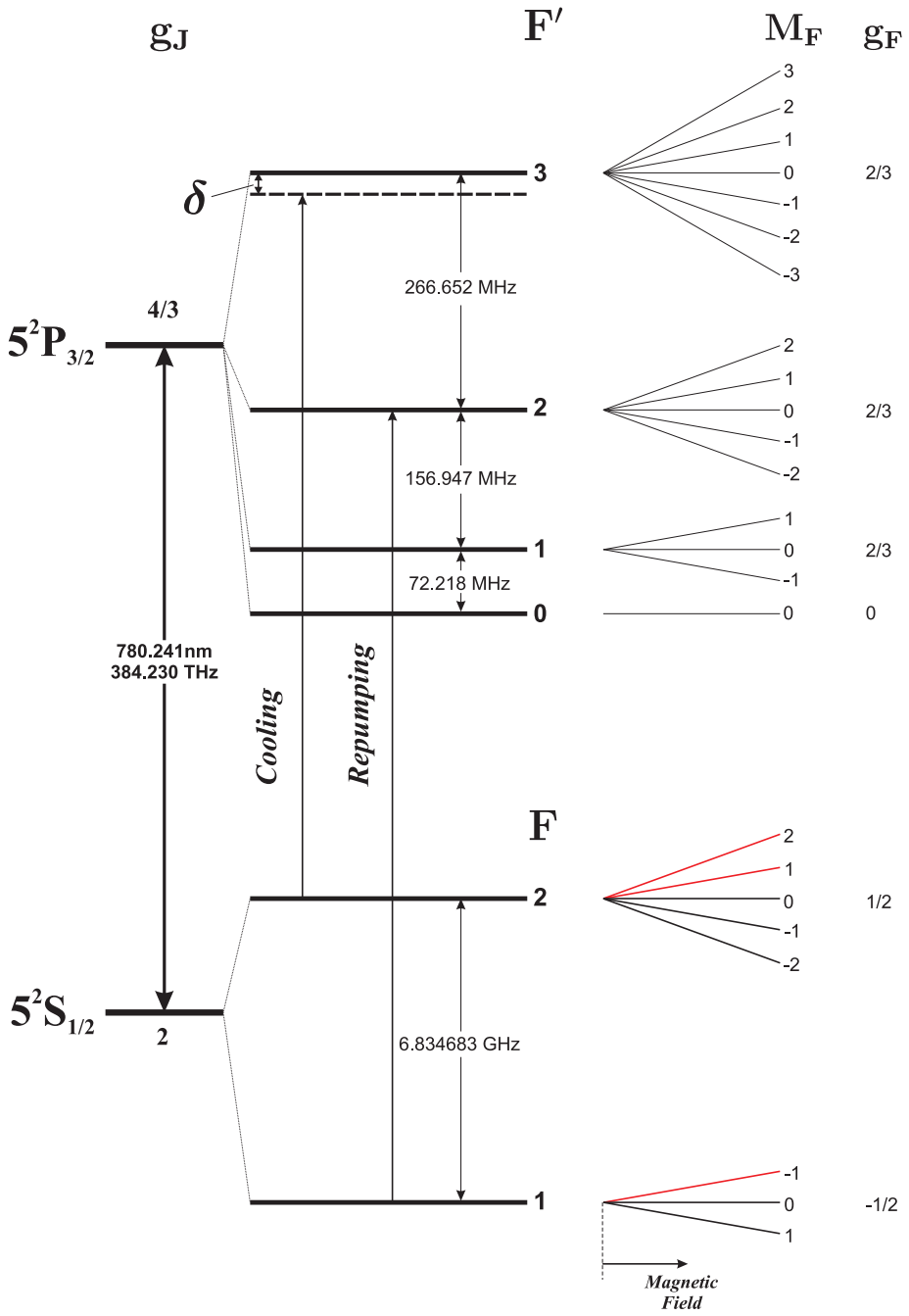

Figure 2.4: The hyperfine structure of the $5^2S_{1/2}$ to $5^2P_{3/2}$ (D2) transition in ^{87}Rb. The Zeeman splitting of the magnetic substates in the weak-field limit is shown with the low-field-seeking substates marked in red.

and $v + dv$ strike the surface area, S, of this volume is a standard result in kinetic theory given by [38]:

$$R = \frac{1}{4} n v S f(v) \tag{2.14}$$

where n is the mean atom density, and $f(v)$ is the Boltzmann distribution. For a 3D gas $f(v)$ is given by [35]:

$$f(v) = \frac{4}{\sqrt{\pi}} \frac{v^2}{v_p^3} \exp\left[-\frac{v^2}{v_p^2}\right] \tag{2.15}$$

where $v_p = \sqrt{\frac{2k_B T}{m}}$ is the most probable velocity of the atoms in the background vapour.

We assume that only atoms with a velocity below a certain capture velocity, v_c, will be captured in the MOT. The constant loading rate can then be calculated by integrating over R from 0 to v_c:

$$a = \frac{1}{4} n S \int_0^{v_c} v f(v) dv = \frac{nS}{\sqrt{\pi} v_p^3} \int_0^{v_c} v^3 \exp\left[\frac{-v^2}{v_p^2}\right] dv. \tag{2.16}$$

We assume that $v_c \ll v_p$ and so the exponential in the integrand can be neglected to give:

$$a \simeq \frac{nS}{4\sqrt{\pi}} \frac{v_c^4}{v_p^3}. \tag{2.17}$$

The value of the loss rate due to collisions with untrapped atoms, b, is given by [27]:

$$b = n \sigma \bar{v} \tag{2.18}$$

where σ is the cross-section for a collision of a trapped atom with an atom in the background vapour, and $\bar{v} = \sqrt{\frac{8k_B T}{\pi m}}$ is the mean atom velocity.

Hence the steady-state atom number is given by:

$$N_s = \frac{a}{b} = \frac{2S}{\pi^2 \sigma} \left(\frac{v_c}{\bar{v}}\right)^4. \tag{2.19}$$

An expression for the capture velocity can be found by considering that for an atom to be captured it must be decelerated to zero velocity over the width, d, of the trapping region. The maximum velocity for which this is possible, the capture velocity, is then given by the simple mechanics relation:

$$v_c^2 = 2Ad \tag{2.20}$$

where A is the acceleration of the atom.

The maximum acceleration experienced by an atom in the MOT can be estimated by noting that for very large beam intensities the scattering rate given by equation 2.3 tends towards $\Gamma/2$. The maximum acceleration is then: $A_{max} = \frac{\hbar k \Gamma}{2m}$, which gives the following expression for the capture velocity:

$$v_c = \sqrt{\frac{\hbar k \Gamma d}{m}}. \tag{2.21}$$

With 3 cm laser beams, as used in the pyramid MOT in the experiment in this thesis, this expression gives a capture velocity $\sim 82\,\mathrm{m\,s^{-1}}$ for rubidium atoms. Applying this expression for v_c to equation 2.19, and considering that $S = d^2$ we get the following dependency:

$$N_s \propto d^4. \tag{2.22}$$

In spite of the simplifying assumptions made in deriving this expression, experiments have confirmed the above dependency holds for trapped atom numbers up to $N \sim 10^{10}$, and therefore to achieve a large atom number in the MOT the size

of the beams should be made as large as possible [39].

As mentioned above, as well as optimising the total atom number it is necessary to maximise the phase space density of the atom cloud. The phase space density of a gas of atoms is given by:

$$\rho = n\lambda_{dB}^3 = n\left(\frac{2\pi\hbar^2}{mk_BT}\right)^{\frac{3}{2}} \tag{2.23}$$

where λ_{dB} is the thermal de Broglie wavelength of the atoms. Therefore to increase the phase space density, the atomic density must be made larger and the average atom temperature made smaller. The optimisation of these parameters was the subject of much early work on the MOT [34,39–43]. It was found that the dynamics of the MOT is strongly dependent on the number of trapped atoms which leads to distinct regimes of MOT behaviour. The typical limits on atom density and temperature depend on which of these regimes the MOT resides in. These regimes were characterised in [43] for MOT sizes up to $N \sim 10^8$ and a summary is given below.

2.2.3 MOT Regimes

When a MOT contains very small atom numbers ($N < 10^4$), the trapped atoms behave as an ideal gas, and their density is set by the balance of the restoring energy and the thermal energy. In this *temperature-limited* density regime the atoms form a gaussian distribution which is contained in a fixed trap volume, set by the value of the spring constant of the trap, so that $n \propto N$.

As more atoms are added to the trap the optical density of the cloud becomes high enough that there is a significant probability for a photon scattered by an atom inside the cloud to be rescattered by a second atom before it leaves the cloud.

This results in a net repulsion between the two atoms. When these interactions are averaged over the whole cloud the result is an outward radiation pressure which limits the density of the MOT cloud. In this regime, termed the *multiple scattering regime*, the increase in volume brought about by the rescattering is proportional to the number of atoms added to the trap and therefore the density remains constant as the atom number increases [44]. This behaviour has been confirmed experimentally for atom numbers up to $N \sim 10^9$ [45]. In addition to its effect on density, the rescattering produces a higher average temperature, with $T \propto N^{1/3}$. This increase in temperature is due to added momentum diffusion and the suppression of sub-Doppler cooling mechanisms both caused by the rescattering [46].

A recent study suggests that a further limitation to density may exist in very large MOTs with $N > 10^9$. At these atom numbers the MOT can become optically thick to the repumping light used to keep the atoms in the cooling cycle. The result is an added outward radiation pressure which gives a drop in density as the atom number is increased above 10^9 [45].

As discussed in subsection 2.1.3, the active cooling mechanisms and average temperature in the optical molasses configuration are highly dependent on the size of the external magnetic field in the vicinity of the atoms. In general, cooling is suppressed as the field strength is increased. Sub-Doppler mechanisms are only active where the Zeeman shift of the atoms' ground state sublevels is less than their light shift. In a MOT, the magnetic field increases in all directions from the centre of the trap and so this condition is met within a radius at which these two shifts are equal [43]:

$$r_{sd} \simeq \frac{\hbar\Gamma^2}{2\mu_B B'_q \delta}\frac{I}{I_{sat}}. \tag{2.24}$$

A cloud which extends beyond this region where sub-Doppler forces are active takes

on a two-component form: at $r < r_{sd}$, sub-Doppler cooling mechanisms produce a relatively dense, low temperature cloud, and at $r > r_{sd}$ a lower density, higher temperature component forms whose dynamics are set largely by the Doppler force [43]. For very low atom number clouds in the temperature-limited density regime, a cloud temperature approximately equal to the optical molasses temperature is observed, indicating that sub-Doppler mechanisms are active in the whole cloud [47]. With larger atom numbers the multiple scattering regime is reached and the increasing cloud size with atom number means that above a certain atom number a portion of the cloud resides at a radius $r > r_{sd}$ where only Doppler cooling is active. As the atom number increases the outer, Doppler portion of the cloud grows and the cloud temperature increases towards the Doppler limit. However, even for atom numbers up to $N \sim 10^8$ the observed cloud temperature remains below the Doppler limit [47] provided that the light shift is sufficiently large. As the cloud of trapped atoms becomes very large ($N \geq 10^8$) the outer component becomes larger than the inner core and the dynamics of the cloud becomes dominated by Doppler forces, and a lower limit on the average cloud temperature equal to the Doppler limit is observed [43].

2.2.4 MOT Compression

In large MOTs ($N > 10^8$) the typical temperature and density limits are $T \simeq T_D$ and $n = 10^{10} - 10^{11}\,\mathrm{cm}^{-3}$, giving a limit to the phase space density of $\rho \sim 10^{-6}$ [45]. A number of approaches have been developed to overcome these limits. Typically, the MOT is first compressed to maximise the atom density. A period of optical molasses cooling is then used to reduce the cloud temperature. For this, the magnetic field is turned off to allow sub-Doppler cooling of the cloud. At the same time, the detuning is increased and the intensities of the trapping and repumping

beams lowered to reduce heating due to rescattering. After this, the cloud has a typical temperature of tens of microkelvin.

The atom density has been improved in schemes that make use of the fact that the optimum parameters for achieving high densities are not the same as those which give optimum MOT loading. The first of these to be used was the dark spontaneous-force optical trap (dark SPOT) (or dark MOT) [48]. In this scheme the MOT is separated into two regions: an outer capture region optimised for MOT loading and a central high density collection region. This scheme makes use of the small probability during laser cooling of off-resonant excitation into a dark substate. As discussed above, in a standard MOT a repumping beam is used to optically pump these dark state atoms back into the cooling transition. In the dark MOT, the central portion of the repumping beam is removed which places a large portion of atoms at the centre of the cloud into a dark state. Since these atoms no longer scatter cooling photons there is a reduction in rescattering and a drop in the outward radiation pressure which increases the spring constant in equation 2.11 and gives a higher density in the centre of the cloud. The resulting form of the MOT is a dense inner cloud of atoms in the dark state surrounded by a less dense outer region in which the light forces on the atoms are the same as in a normal bright MOT to give efficient capture of atoms from the background vapour. This approach gives densities on the order of $n = 10^{12}\,\mathrm{cm}^{-3}$ – an order of magnitude larger than in normal large MOTs [48, 49].

In a second approach to MOT compression the parameters of the MOT are varied in time rather than in space as above, and this scheme is referred to as the temporal dark SPOT [42, 49, 50]. The rapid change in the trapping parameters results in a transient change in the characterisitics of the atom cloud. The typical approach in the compression stage is to increase the magnitude of the detuning and

reduce the intensity of the trapping and repumping light to reduce the re-radiation pressure in the cloud. At the same time, the magnetic field gradient is increased. The combined effect of these changes is to produce a transient increase in the spring constant of the trap which causes the atoms to rush towards the centre of the atom cloud. This gives typical final densities of $n = 10^{12}\,\mathrm{cm}^{-3}$. Since the change in density is transient, the atoms must be rapidly captured in a magnetic trap to maintain the improved phase space density.

A final approach to MOT compression uses the same changes in the light parameters as in the temporal dark MOT to reduce the re-radiation pressure, however in this case the magnetic field gradient is *decreased* [51]. The effect of this is to increase r_{sd} and the volume over which sub-Doppler cooling mechanisms are active. The stronger confinement given by sub-Doppler forces results in a lower average cloud temperature and a higher density.

All of the above MOT compression techniques raise the MOT density to a maximum of approximately $10^{12}\,\mathrm{cm}^{-3}$. This limit to the MOT density is set by the inherent rescattering and intra-trap collisions at these densities [48, 49]. With the typical average cloud temperatures the resulting upper limit on the phase space density in the MOT is on the order of 10^{-5} [49]. This limit to the phase space density can only be overcome by transferring the atoms to a trap which is free from rescattering. In the experiment in this thesis, following capture and compression in the MOT the atoms are transferred to a magnetic potential and evaporative cooling is used to further lower the temperature. The details of this magnetic trapping are outlined in the following section.

2.2.5 New MOT Design

In the design of the new apparatus the general approach was to use a scaled-up version of the pyramid MOTs which had previously been used in our group [52–54]. These MOTs captured approximately 10^8 atoms, and the aim in the new MOT was to increase this value to approximately 5×10^9. In order to increase the atom number, the size of the pyramid mirrors was increased to produce larger beams and take advantage of the rapid scaling of number with beam size expressed in equation 2.22. A difference from the previous pyramid MOTs used in our group was that this MOT would act as the *main* MOT rather than as a 'funnel' MOT feeding a second, main MOT. In order to allow the atoms to be moved out of the pyramid following capture and cooling, our design also incorporated a slit in one corner of the pyramid. This feature was based on a similar design used in JILA [55]. Further details of the MOT construction and design are given in section 5.3.

With $N \simeq 5 \times 10^9$ the new MOT is in the very large atom number, multiple scattering regime discussed above, in which the temperature and dynamics of the atom cloud are set by Doppler forces. In order to maximise the phase space density prior to magnetic transport of the atoms out of the MOT, a compression stage was included. This was based on the third of the approaches discussed in subsection 2.2.4, in which the frequency detuning of the trapping beams is increased to reduce rescattering, and the magnetic field is lowered to increase the extent of the cloud that is subject to sub-Doppler forces. The full details of the experimental MOT sequence are given in chapter 6.

2.3 Magnetic Trapping

The basis of magnetic trapping of neutral atoms is the interaction between the magnetic dipole moment of the atom and an external magnetic field. The potential which arises from the interaction of an atom's magnetic moment, $\boldsymbol{\mu}$, with an inhomogeneous external magnetic field, $\mathbf{B}$, is given by:

$$U = -\boldsymbol{\mu}.\mathbf{B}. \tag{2.25}$$

In the weak-field limit this becomes:

$$U = g_F m_F \mu_B |\mathbf{B}| \tag{2.26}$$

where g_F is the Landé factor, m_F is the Zeeman substate of the hyperfine level F, and μ_B is the Bohr magneton.

Maxwell's equations forbid a local maximum of the magnetic field in free space [56], therefore a field minimum must be used to trap the atoms. Only atoms in states with $g_F m_F > 0$ are trapped at a potential minimum, and these are referred to as *low-field-seeking* states. States with $g_F m_F < 0$ are *high-field-seeking* states and are repelled away from the potential minimum and lost from the trap. For ^{87}Rb there are three low-field-seeking substates: $|F = 1, m_F = -1\rangle$, $|F = 2, m_F = 2\rangle$ and $|F = 2, m_F = 1\rangle$. In the experiment in this thesis the atoms were trapped in the $|F = 1, m_F = -1\rangle$ substate since this substate has better collisional properties than the $|F = 2, m_F = 2\rangle$ substate, which gives increased efficiency in the evaporative cooling stage.

2.3.1 The Quadrupole Potential

The simplest arrangement of magnetic coils that produces a field minimum is the anti-Helmholtz configuration which consists of two coaxial coils which carry current travelling in opposite directions. The spherical quadrupole field produced at the centre of a pair of anti-Helmholtz coils is given, to first order, by [57]:

$$\mathbf{B_q} = B'_q \left(\frac{x}{2}\hat{\mathbf{e}}_x + \frac{y}{2}\hat{\mathbf{e}}_y - z\hat{\mathbf{e}}_z \right) \tag{2.27}$$

where B'_q is the magnetic gradient in the axial (z-) direction. The resulting potential, $U = -\boldsymbol{\mu}.\mathbf{B_q}$, has a minimum at the mid-point of the two coils on the z-axis. At this point the fields from the two coils exactly cancel to give zero magnetic field.

A major shortcoming of the quadrupole potential arises from this point of zero field at its centre. Around this point the magnetic moment of the atom can no longer adiabatically follow the rapidly changing direction of the magnetic field and the atoms can undergo transitions to untrapped magnetic substates [42]. These transitions are referred to as Majorana flops. As the temperature of the cloud of trapped atoms is decreased the atoms spend longer in the vicinity of the field zero in the centre and thus the atom loss rate increases. At sufficiently low temperatures (typically below $\sim 100\,\mu$K) Majorana flops become the dominant loss mechanism and severely limit the lifetime of the cloud. For this reason the quadrupole potential is not suitable for confining the atoms during the final cooling stage to the BEC transition.

A number of solutions have been developed which remove the magnetic field zero at the centre of the quadrupole potential to eliminate Majorana losses. An early scheme used a blue-detuned laser beam to plug the hole at the bottom of the

potential [14]. Alternatively, a static magnetic bias field may be applied to produce a Ioffe-Pritchard style trap [58, 59]. In the experiment in this thesis a time-varying bias field is applied to produce the time-orbiting potential (TOP) trap outlined in the next subsection.

2.3.2 The Time-Orbiting Potential Trap

The TOP trap was first demonstrated at JILA [42] and was used there in the first experiment which achieved BEC [13]. To create the TOP trap a bias field rotating in the xy-plane is added to the quadrupole potential given in equation 2.27, as illustrated in figure 2.5. This time-averages the quadrupole potential to produce a harmonic potential free from points of zero magnetic field. The rotating bias field has the form:

$$\mathbf{B_T}(t) = B_T(\cos\omega_T t\hat{\mathbf{e}}_x + \sin\omega_T t\hat{\mathbf{e}}_y) \tag{2.28}$$

where B_T is the amplitude of the bias field and ω_T is the angular frequency of rotation of the bias field.

The bias field rotation frequency is chosen to be larger than the typical trapping frequencies such that the atoms cannot follow the instantaneous movement of the magnetic field, and smaller than the Larmor precession frequency such that the atomic magnetic dipoles can follow the changing magnetic field direction, thereby avoiding non-adiabatic transitions to untrapped magnetic substates. To fulfil these criteria a bias field frequency, $\omega_T/2\pi$, of 7 kHz was used in the experiment.

The rotating bias field is added to the static quadrupole field, to give a total magnetic field:

$$\mathbf{B_{TOP}}(t) = B'_q\left(\frac{x}{2}\hat{\mathbf{e}}_x + \frac{y}{2}\hat{\mathbf{e}}_y - z\hat{\mathbf{e}}_z\right) + B_T(\cos\omega_T t\hat{\mathbf{e}}_x + \sin\omega_T t\hat{\mathbf{e}}_y). \tag{2.29}$$

The potential energy of atoms in the TOP trap is given by the interaction energy of the atomic magnetic dipole with this magnetic field: $U = -\boldsymbol{\mu}.\mathbf{B_{TOP}}$. To obtain an expression for the time-averaged potential this instantaneous TOP potential must be integrated over one whole cycle:

$$\begin{aligned} U_{TOP} &= \frac{\omega_T}{2\pi}\int_0^{\frac{2\pi}{\omega_T}} g_F m_F \mu_B \left|\mathbf{B_{TOP}}(t)\right| dt && (2.30)\\ &\simeq g_F m_F \mu_B \left[B_T + \frac{B_q'^2}{16 B_T}\left(x^2+y^2+8z^2\right)\right] && (2.31)\\ &= U_0 + \frac{1}{2}m\omega_r^2 r^2 + \frac{1}{2}m\omega_z^2 z^2 && (2.32)\end{aligned}$$

where

$$\begin{aligned} \omega_r &= \sqrt{\frac{g_F m_F \mu_B B_q'^2}{8 m B_T}} && (2.33)\\ \omega_z &= \sqrt{\frac{g_F m_F \mu_B B_q'^2}{m B_T}} = \sqrt{8}\omega_r. && (2.34)\end{aligned}$$

U_{TOP} has the form of a radially symmetric harmonic potential with a minimum of $U_0 = g_F m_F \mu_B B_T$. The difference in trapping frequencies in the radial and axial directions results in trapped atom clouds with an aspect ratio of $\sqrt{8} : 1$.

The instantaneous picture of the TOP trap is shown in figure 2.5. The magnetic field zero of the quadrupole potential moves in a circle, known colloquially as the *circle of death*, of radius:

$$r_0 = \frac{2B_T}{B_q'}. \qquad (2.35)$$

Atoms are lost from the trap at this locus of field zero through Majorana flops, and thus the effective depth of the TOP trap is equal to: $U(r_0, z=0) - U_0 = \frac{g_F m_F \mu_B B_T}{4}$. For our maximum B_T of 43 G this trap depth corresponds to a temperature of 361 μK.

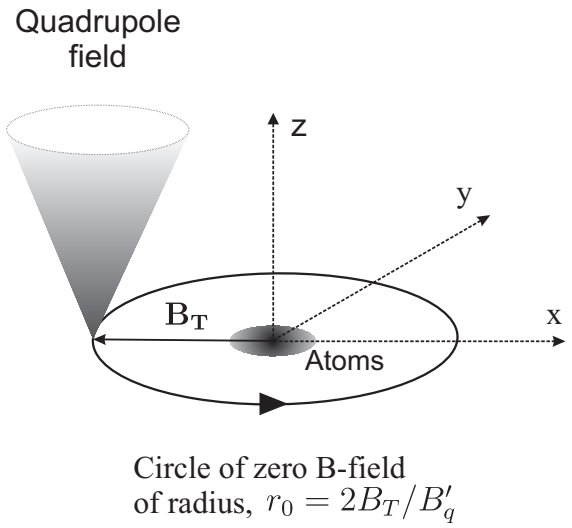

Figure 2.5: Schematic of the time-orbiting potential (TOP) trap.

The value of r_0, and hence the trap depth, can be changed by changing the magnitude of the TOP bias field, B_T. This is exploited in the first stage of evaporative cooling in the TOP trap during which the trap depth is reduced to remove the hottest, outermost atoms (see subsection 7.1.3).

2.4 Bose-Einstein Condensation

In quantum mechanics particles are divided into two kinds which have different quantum statistics. Those with integral spin are *bosons* and have wavefunctions that are symmetric under the exchange of any pair of particles in a system of particles. Those with half-integral spin are *fermions* and have wavefunctions that are antisymmetric under the exchange of any pair of particles. The difference in the form of the wavefunctions of bosons and fermions means that they distribute themselves differently among a series of energy levels. Fermions obey the Pauli exclusion principle which states that no two particles may exist in the same quantum state, and so tend to fill up the energy levels successively, with one particle in each

level. Bosons are not restricted in this way and in fact have a natural tendancy to group together in the same energy level. These two different behaviours arise purely from the allowed combinatorics of placing particles into a series of energy levels.

Quantum statistical mechanics must be invoked when the population of individual energy levels becomes of order unity, which occurs when the phase space density of the system is high. At lower phase space densities the system is well approximated as a continuum of energy levels. In this classical limit the quantum Fermi-Dirac and Bose-Einstein distributions which describe fermions and bosons respectively tend towards the classical Maxwell-Boltzmann distribution.

In the case of bosons, the tendancy of the particles to group together in the same state means that below a certain temperature the particles can form a macroscopic population in the ground energy state. This phase transition, termed Bose-Einstein condensation, arises purely from the quantum statistics of the particles. An intuitive picture of this phase transition may be gained by noting that condensation occurs in a system of particles with a phase space density for which the inter-particle separation is approximately equal to the de Broglie wavelength of the particles:

$$\rho = n\lambda_{dB}^3 \approx 1. \tag{2.36}$$

At this point the wavefunctions of the particles will overlap. The particles are then no longer described by individual wavefunctions but by a common, macroscopic, many-body wavefunction.

2.4.1 Uniform Ideal Bose Gas

In a uniform ideal gas of identical bosons confined in a volume, V, the occupation of the energy level, E_i, is given by [60]:

$$n_i(E_i) = \frac{g(E_i)}{\exp\left(\frac{E_i-\mu}{k_B T}\right) - 1} \tag{2.37}$$

where $g(E_i)$ is the degeneracy of each level, and μ is the chemical potential.

In the grand canonical ensemble the chemical potential and the temperature are calculated from the following constraints on the total atom number, N, and total energy, E:

$$N = \sum_i n_i(E_i) \tag{2.38}$$

$$E = \sum_i E_i n_i(E_i). \tag{2.39}$$

We assume that $V \to \infty$, so that the energy levels form a continuum and the sum in equation 2.38 can be changed into an integral. The total atom number is then given by:

$$N = N_0 + \int_0^\infty n(E) D(E) \mathrm{d}E = N_0 + N_e \tag{2.40}$$

where N_0 and N_e are the number of atoms in the ground and excited stated respectively and $D(E)$ is the density of states, which for a uniform non-interacting gas, is given by:

$$D(E) = \frac{V}{4\pi^2}\left(\frac{2m}{\hbar^2}\right)^{\frac{3}{2}} \sqrt{E}. \tag{2.41}$$

It is necessary to keep N_0 outside the integral in equation 2.40 since $D(0) = 0$.

At high temperatures the chemical potential of the atoms is large and negative. As the temperature is reduced the chemical potential increases in order to keep

the total particle number constant in accordance with equation 2.38. At a critical temperature, T_c, the chemical potential becomes zero. At this point $N_0 = 0$ and N_e reaches its maximum value. Any further increase in the chemical potential is forbidden since that would result in unphysical predictions from equation 2.37. Further decreasing the temperature therefore results in atoms cascading into the ground state and for $T < T_c$ there is a macroscopic ground state population.

The transition temperature, T_c, may be calculated by first evaluating the integral in equation 2.40 to give:

$$N - N_0 = V \frac{g_{3/2}(z)}{\lambda_{dB}^3} \tag{2.42}$$

where the function $g_\alpha(x) = \sum_{j=1}^{\infty} x^j / j^\alpha$ and $z = \exp\left(\frac{\mu}{k_B T}\right)$ is the fugacity of the gas. At the transition temperature, $\mu = 0$ so that $z = 1$, and $N_0 = 0$. Entering these values into equation 2.42 and rearranging gives the phase space density at the transition:

$$\rho = n\lambda_{dB}^3 \approx 2.612. \tag{2.43}$$

The transition temperature is defined as that which occurs in λ_{dB} in the above equation and is thus given by:

$$T_c = \frac{2\pi\hbar^2}{m k_B} \left(\frac{n}{g_{3/2}(1)} \right)^{\frac{2}{3}}. \tag{2.44}$$

The fraction of atoms in the ground state can be found by inserting equation 2.44 into equation 2.42 and rearranging to give:

$$\frac{N_0}{N} = 1 - \left(\frac{T}{T_c} \right)^{\frac{3}{2}}. \tag{2.45}$$

2.4.2 Trapped Ideal Bose Gas

In the experiment in this thesis the atoms are trapped in a harmonic potential. This inhomogeneous trapping potential modifies the density of states compared to that in the uniform case, and this modification in turn changes the scaling of the system properties around the transition to BEC. The form of a 3D harmonic potential is given by:

$$V_{ext} = \frac{m}{2}\left(\omega_x^2 x^2 + \omega_y^2 y^2 + \omega_z^2 z^2\right) \tag{2.46}$$

where $\omega_x, \omega_y, \omega_z$ are the trapping frequencies in the x-,y- and z-directions respectively. For an ideal gas the eigenvalues of the resulting Hamiltonian are given by:

$$E = \left(n_x + \frac{1}{2}\right)\hbar\omega_x + \left(n_y + \frac{1}{2}\right)\hbar\omega_y + \left(n_z + \frac{1}{2}\right)\hbar\omega_z \tag{2.47}$$

where n_x, n_y, n_z are non-negative integers. The density of states for identical bosons in such a potential is given by:

$$D_{tr}(E) = \frac{E^2}{2(\hbar\omega_{ho})^3} \tag{2.48}$$

where $\omega_{ho} = (\omega_x\omega_y\omega_z)^{1/3}$ is the geometric mean of the trapping frequencies. Using this value for the density of states in equation 2.40 gives:

$$N - N_0 = g_3(1)\left(\frac{k_B T}{\hbar\omega_{ho}}\right)^3 \tag{2.49}$$

where $g_3(1) \simeq 1.202$.

As before, at the transition to BEC $N_0 = 0$, so that the critical temperature,

$$T_c = \frac{\hbar\omega_{ho}}{k_B}\left(\frac{N}{g_3(1)}\right)^{\frac{1}{3}}. \tag{2.50}$$

The fraction of atoms in the ground state is then given by:

$$\frac{N_0}{N} = 1 - \left(\frac{T}{T_c}\right)^3. \tag{2.51}$$

A calculation of the BEC transition temperature and condensate fraction in a generic power-law potential may be found in [61].

2.4.3 Interacting Bose Gas

In the above derivations it was assumed that the gas of atoms was non-interacting. However, the density of typical condensates produced in experiments is relatively high ($n \sim 1\times10^{14}\,\mathrm{cm}^{-3}$), and the interactions between the atoms are strong enough to modify the condensate's dynamics significantly. Fortunately, the interactions are still sufficiently weak that a mean-field approach can be used to model the condensate's dynamics.

An interacting gas of atoms can be described by the following many-body Hamiltonian which takes into account the interactions between pairs of atoms confined in an external potential, V_{ext} [62]:

$$\hat{H} = \int_0^\infty \mathrm{d}^3\mathbf{r}\hat{\Psi}^\dagger(\mathbf{r}) \left[-\frac{\hbar^2\nabla^2}{2m} + V_{ext}(\mathbf{r}) + \frac{1}{2}\hat{\Psi}^\dagger(\mathbf{r}')V(\mathbf{r}-\mathbf{r}')\hat{\Psi}(\mathbf{r}')\right]\hat{\Psi}(\mathbf{r}) \tag{2.52}$$

where $\hat{\Psi}^\dagger$ and $\hat{\Psi}$ are the boson field operators that create and annihilate particles at position $\mathbf{r}$, and $V(\mathbf{r}-\mathbf{r}')$ is the two-body interaction potential. By including only two-body interactions in the Hamiltonian we assume that the density and temperature are low. This assumption also allows the interactions to be considered weak so that the interaction potential can be approximated as a mean field:

$$V(\mathbf{r}-\mathbf{r}') = g\delta(\mathbf{r}-\mathbf{r}') \tag{2.53}$$

where the coupling term, $g = \frac{4\pi\hbar^2 a_s}{m}$, in which a_s is the s-wave scattering length. Here it is assumed that only s-wave interactions are present which, again, is only valid in the limit of low density and temperature. These conditions may be expressed as: $n|a_s|^3 \ll 1$, and $T \ll T_c$.

The time evolution of the field operator is given by using the Hamiltonian in equation 2.52 in the Heisenberg equation:

$$i\hbar\frac{\partial\hat{\Psi}(\mathbf{r},t)}{\partial t} = \left[\hat{\Psi}(\mathbf{r},t), \hat{H}\right]. \tag{2.54}$$

When the occupation of the ground state becomes macroscopic the Bogoliubov approximation can be made in which the field operator is decomposed into two components [63]:

$$\hat{\Psi}(\mathbf{r},t) = \Phi(\mathbf{r},t) + \hat{\delta}(\mathbf{r},t) \tag{2.55}$$

where $\Phi(\mathbf{r},t)$ is a complex function which describes the condensate and is defined as the expectation value of the field operator, $\langle\hat{\Psi}(\mathbf{r},t)\rangle$, and $\hat{\delta}(\mathbf{r},t)$ is a perturbation which describes the excited modes of the boson field. The density of the condensate, $n_0(\mathbf{r},t) = |\Phi(\mathbf{r},t)|^2$. We again assume a low temperature so that the excitation term in equation 2.55 may be neglected. Then, the operator, $\hat{\Psi}(\mathbf{r},t)$, in equation 2.54 may be replaced by $\Phi(\mathbf{r},t)$ to give the Gross-Pitaevskii equation [64, 65]:

$$i\hbar\frac{\partial\Phi(\mathbf{r},t)}{\partial t} = \left[-\frac{\hbar^2\nabla^2}{2m} + V_{ext}(\mathbf{r}) + g\left|\Phi(\mathbf{r},t)\right|^2\right]\Phi(\mathbf{r},t). \tag{2.56}$$

The Gross-Pitaevskii equation gives an accurate description of the condensate dynamics on a length scale that is large compared to the interatomic distance. This equation is only valid in the limit of low density and temperature.

2.4.4 The Thomas-Fermi Approximation

A time-independent form of the Gross-Pitaevskii equation may be obtained by writing the ground state wavefunction as:

$$\Phi_g(\mathbf{r},t) = \Phi_0(\mathbf{r}) \exp\left(-\frac{i\mu t}{\hbar}\right). \tag{2.57}$$

Substituting this solution into equation 2.56 gives:

$$\left(-\frac{\hbar^2\nabla^2}{2m} + V_{ext}(\mathbf{r}) + g|\Phi_0(\mathbf{r})|^2\right)\Phi_0(\mathbf{r}) = \mu\Phi_0(\mathbf{r}). \tag{2.58}$$

In a harmonic trapping potential the ratio of the interaction and kinetic energies is given by [62]:

$$\frac{E_{int}}{E_{KE}} \propto \frac{N\,|a_s|}{a_{ho}} \tag{2.59}$$

where $a_{ho} = \sqrt{\hbar/m\omega_{ho}}$ is the mean harmonic oscillator length of the trapping potential. For condensates with large N this ratio is large and the kinetic energy term, $-\frac{\hbar^2\nabla^2}{2m}$, in equation 2.58 may be neglected. This approximation is called the Thomas-Fermi approximation. Equation 2.58 then becomes:

$$V_{ext}(\mathbf{r}) + g|\Phi_0(\mathbf{r})|^2 = \mu. \tag{2.60}$$

Solving this equation gives the density distribution of the condensate as the following parabolic form:

$$|\Phi_0(\mathbf{r})|^2 = \frac{\mu}{g}\left(1 - \frac{x^2}{R_x^2} - \frac{y^2}{R_y^2} - \frac{z^2}{R_z^2}\right) \tag{2.61}$$

where $R_i = \sqrt{\frac{2\mu}{m\omega_i^2}}$ is the width of the condensate in the i-direction and the chemical potential is given by:

$$\mu = \frac{\hbar\omega_{ho}}{2}\left(\frac{15N_0a_s}{a_{ho}}\right)^{\frac{2}{5}}. \tag{2.62}$$

Chapter 3

Radio-Frequency Dressed Potentials

3.1 Motivation: Low-Dimensional Systems

The TOP magnetic trapping scheme, outlined in the previous chapter, and the Ioffe-Pritchard counterparts provide harmonic trapping potentials with frequencies on the order of 100 Hz using relatively simple arrangements of magnetic coils. As a result, these configurations have become one of the standard means to trap atoms in the final stages of BEC experiments. However, a large number of experiments demand a more complex trapping geometry than the simple harmonic, relatively low trapping frequency, form afforded by these schemes. An important range of experiments involves studying the physics of ultracold gases confined to potentials with effectively less than three dimensions. Such systems will be investigated in the new apparatus where they will be created using the RF-dressed magnetic potentials described in this chapter.

The physics of 1D and 2D Bose gases is fundamentally different from that of the 3D case. In 3D, Bose-Einstein condensation can occur as a result of the long-range order in the gas, and BEC is predicted to occur even in a homogeneous, ideal gas, as described in subsection 2.4.1. In lower dimensions the existence of finite temperature superfluid and BEC transitions is strongly dependent on the interactions in the gas and its confinement. A comprehensive overview of the predicted behaviour of 1D and 2D quantum gases may be found in [66], and references therein, and a brief summary is given in the following paragraphs.

In the homogeneous 2D case, a transition to BEC at finite temperature is not possible since thermal fluctuations destroy any long-range order in the gas. This is true even for an interacting gas. However, a superfluid transition is predicted in this homogeneous, interacting case. This phase transition is based on the emergence of a topological order: the Berezinskii, Kosterlitz, Thouless (BKT) transition [67,68]. The topological order arises from the pairing of vortex-anti-vortex pairs, giving quasi-long-range order in the gas. This gives rise to a state termed the 'quasi-condensate', with local coherence rather than the global coherence of a BEC, and this coherence leads to a superfluid transition. There is some debate about the nature of the superfluid transition in the harmonically trapped 2D gas since the harmonic confinement modifies the density of states of the gas in such a way to make conventional BEC possible [69, 70]. A summary of the predicted BKT and BEC transitions in a 2D gas for different interaction strengths and forms of trapping potential is given in [71].

The BKT transition has been observed in a number of condensed matter systems including helium films [72], superconducting Josephson-junction arrays [73] and spin-polarised hydrogen [74]. Recently, this transition has been observed in ultracold gases: in gases in 2D potentials [75–77], and in a 2D lattice of Josephson-

coupled BECs [78]. In the experiment of Hadzibabic *et al* a proliferation of thermally-activated vortices in a 2D gas just above the predicted BKT transition point was observed, as well as an abrupt increase in the superfluid fraction around this point [75]. Krüger *et al* measured the critical atom number at the superfluid transition in an array of harmonically trapped BECs [76]. This number was considerably higher than predicted by BEC theory but agreed closely with the predictions of the BKT model which the authors used. In the experiment of Cladé *et al*, a 2D gas was observed to go through two distinct regimes as the temperature was lowered below the BKT transition temperature (T_{BKT}) [77]. With $T > T_{BKT}$, a crossover from the thermal state to a non-superfluid quasi-condensate state was observed. As the temperature was reduced below T_{BKT} a sharp transition to a superfluid quasi-condensate state was observed. These experiments have confirmed the general features of the BKT transition, however several points remain outstanding. In particular, as yet, there have been no experiments which have directly probed the superfluid properties of the 2D gas. This should form the focus of future experimental studies on 2D systems.

In a homogeneous non-interacting 1D gas, no finite temperature BEC transition occurs, however the presence of interactions modifies the behaviour of the homogeneous gas allowing a crossover to a quasi-condensate state. The behaviour of the gas is further modified by its confinement, and in the harmonically-trapped case depends upon the strength of its interactions which is set by the density of the gas. At high densities the interactions are weak and a finite temperature transition to BEC is possible [79]. At low densities, the interactions are strong and a transition to the Tonks-Girardeau regime occurs in which the gas possesses strongly correlated, fermionic properties [80]. The rich physics of 1D Bose gases is the subject of ongoing experimental investigations.

In order to reduce the dimensionality of a 3D system and enter the quasi-2D regime, one of the trapping frequencies, ω_{trap}, of the confining potential must fulfil the following condition: $\omega_{trap} > \mu$, where μ is the 3D chemical potential given in equation 2.62. This is equivalent to requiring that the energy level spacing in the tightly confined direction should be greater than the interaction energy between atoms. Similarly, to enter the quasi-1D regime two trapping frequencies must fulfil this condition. Typically trapping frequencies on the order of 1 KHz are required to meet this criterion, and such high frequencies cannot be obtained using typical magnetic potentials such as the TOP or Ioffe-Pritchard traps. Instead, to date, the typical approach has been to use optical dipole potentials [81, 82].

An alternative approach to creating quasi-2D potentials, employing a purely magnetic potential, was proposed by Zobay and Garraway in 2001 [83]. This approach involves the dressing of static magnetic potentials with radio-frequency (RF) radiation to produce adiabatic dressed-state potentials. In this way, a large range of trapping geometries can be created through the dressing of the standard static magnetic potentials. Since the parameters of the RF and the magnetic trap may be controlled dynamically, the form of the dressed-state potentials may be morphed adiabatically between different geometries. In addition, since the trapping potentials are formed far from the magnetic coils, the potentials are very smooth and free from corrugations. This is an advantage over optical dipole traps where the trapping potential often exhibits such small scale features.

RF-dressing also allows the creation of traps with different topologies from the simple harmonic case. To date, experimentally demonstrated potentials include double-well potentials [84] and toroidal potentials [19, 85]. Proposals have also been made for lattice potentials [86] and more complex toroidal and ring-shaped potentials [87]. The toroidal potential is important since its multiply-connected

topology allows the creation of persistent currents in superfluid samples. The persistent current is a key hallmark of superfluidity [88], and thus could be used to test for the presence of superfluidity in the quasi-2D and quasi-1D regimes.

In this chapter the theory of RF dressed potentials is presented. First, the interaction of an atom with a rapidly oscillating field is outlined, culminating in the dressed-state picture of the atom in this field. An overview of the RF-dressed trapping potentials that we intend to produce in the new experiment is then given. These include a purely magnetic ellipsoidal potential which allows quasi-2D trapping, and a toroidal potential formed by dressing a combined magnetic and optical dipole potential which, for the parameters of the new experiment, will allow entry into the quasi-2D and quasi-1D regimes. This is a continuation of work begun in the old apparatus, presented in the theses of William Heathcote [20] and Eileen Nugent [21]. Finally, a new scheme is presented which combines RF dressing with time-averaging to allow the creation of purely magnetic toroidal and double-well potentials.

3.2 Interaction of a Two-Level Atom with Radiation

The interaction of an atom with an oscillating electromagnetic field can be modelled using a semiclassical approach in which the atom has quantised energy levels and the field is treated as a classical field. The Hamiltonian of this system can be represented as:

$$H = H_0 + H_{int} \tag{3.1}$$

where H_0 is the Hamiltonian of the unperturbed atom, and H_{int} is a perturbation arising from the interaction of the atom with the field. A general expression for

H_{int} of the following form is assumed:

$$H_{int} = V\cos(\omega t) \tag{3.2}$$

where V is the amplitude of the interaction and ω is the angular frequency of the oscillating radiation field.

We assume that the atom has a two-level wavefunction of the form:

$$\Psi(\mathbf{r},t) = c_1 \mathrm{e}^{-i\omega_1 t}|1\rangle + c_2 \mathrm{e}^{-i\omega_2 t}|2\rangle \tag{3.3}$$

where $E_i = \hbar\omega_i$ are the energies of the atomic levels. The time evolution of the system is given by the time-dependent Schrödinger equation:

$$i\hbar\frac{\mathrm{d}\Psi}{\mathrm{d}t} = H\Psi. \tag{3.4}$$

Substituting equations 3.1 and 3.3 into this equation gives the coupled equations:

$$i\dot{c}_1 = \Omega\cos(\omega t)\mathrm{e}^{-i\omega_0 t}c_2 \tag{3.5}$$

$$i\dot{c}_2 = \Omega^*\cos(\omega t)\mathrm{e}^{i\omega_0 t}c_1 \tag{3.6}$$

where $\omega_0 = \omega_2 - \omega_1$, and $\Omega = \langle 1|V|2\rangle/\hbar$ is the Rabi frequency.

The cosine in the above equations may be rewritten, $\cos(\omega t) = \frac{\mathrm{e}^{i\omega t}+\mathrm{e}^{-i\omega t}}{2}$ to give:

$$i\dot{c}_1 = \frac{\Omega}{2}\left(\mathrm{e}^{i(\omega-\omega_0)t} + \mathrm{e}^{-i(\omega+\omega_0)t}\right)c_2 \tag{3.7}$$

$$i\dot{c}_2 = \frac{\Omega}{2}^*\left(\mathrm{e}^{i(\omega+\omega_0)t} + \mathrm{e}^{-i(\omega-\omega_0)t}\right)c_1. \tag{3.8}$$

The radiation is assumed to be close to resonance with the atomic transition so

that $\omega \simeq \omega_0$. Then the term rotating at $\omega + \omega_0 \simeq 2\omega_0$ rotates much faster than the $\omega - \omega_0$ term and may be neglected in the rotating wave approximation. The resulting coupled equations can be written in matrix form:

$$i\frac{\mathrm{d}}{\mathrm{d}t}\begin{pmatrix} c_1 \\ c_2 \end{pmatrix} = \frac{1}{2}\begin{pmatrix} 0 & \Omega\,\mathrm{e}^{i\delta t} \\ \Omega^*\,\mathrm{e}^{-i\delta t} & 0 \end{pmatrix}\begin{pmatrix} c_1 \\ c_2 \end{pmatrix} \tag{3.9}$$

where $\delta = \omega - \omega_0$ is the detuning of the radiation from the atomic transition. Applying the transformation

$$\begin{pmatrix} \tilde{c}_1 \\ \tilde{c}_2 \end{pmatrix} = \begin{pmatrix} \mathrm{e}^{-i\delta t/2} & 0 \\ 0 & \mathrm{e}^{i\delta t/2} \end{pmatrix}\begin{pmatrix} c_1 \\ c_2 \end{pmatrix} \tag{3.10}$$

gives

$$i\frac{\mathrm{d}}{\mathrm{d}t}\begin{pmatrix} \tilde{c}_1 \\ \tilde{c}_2 \end{pmatrix} = \begin{pmatrix} \delta/2 & \Omega/2 \\ \Omega^*/2 & -\delta/2 \end{pmatrix}\begin{pmatrix} \tilde{c}_1 \\ \tilde{c}_2 \end{pmatrix}. \tag{3.11}$$

The solutions to these equations are:

$$\begin{pmatrix} \tilde{c}_1 \\ \tilde{c}_2 \end{pmatrix} = \begin{pmatrix} a \\ b \end{pmatrix}\mathrm{e}^{-i\lambda_{2L}t} \tag{3.12}$$

where a and b are constants and λ_{2L} are the eigenvalues of the total Hamiltonian given by:

$$U = \hbar\lambda_{2L} = \pm\frac{\hbar}{2}\sqrt{\delta^2 + |\Omega|^2}. \tag{3.13}$$

The potentials in equation 3.13 describe the combined atom + field system with Hamiltonian, H. The form of these potentials is of two energy levels separated by an energy $\hbar\delta$ plus an amount $\hbar|\Omega|$ arising from the perturbation of the oscillating field. Since the value of these terms is time-independent, the potentials in equation

3.13 are also time-independent. This system may be described using the *dressed-atom* picture developed by Cohen-Tannoudji [25]. In this picture, the radiation field is considered quantised rather than classical and time-independent energy levels representing the whole system (atom + field) – the so-called dressed states – are introduced. The atom can be considered to move in these time-independent potentials. The dressed states are described according to the energy level of the atom – $|1\rangle$ or $|2\rangle$ – and the energy level of the radiation field, $|n\rangle$. This gives rise to a ladder of dressed states: $|i, n\rangle$. In the uncoupled basis ($\Omega = 0$) adjacent states are simply separated by an energy $\hbar\delta$, but for finite coupling these states repel each other by an amount $\hbar\sqrt{\delta^2 + \Omega^2}$.

3.3 Extension to a Three-Level Atom

The RF-dressing scheme which was used in the old experimental setup and which will be used in the new apparatus works by dressing the bare magnetic substates of ^{87}Rb. In our experimental scheme the atoms are magnetically trapped in the $F = 1$ state, which has three magnetic substates: $m_F = 0, \pm 1$. Expressions for the dressed-state energy levels in this case may be found by extending the above treatment to the case of a three-level atom. This is simplified by the fact that the magnetic substates of the $F = 1$ state are equally spaced about zero energy. As in the above two-level atom derivation, the RF field is treated as a perturbation, with a form given by equation 3.2. The rotating wave approximation is then used to allow the coupled equations of the system to be solved. The result of this treatment, outlined in full in [20], is the following three-level equivalent to the

dressed-state equation 3.11:

$$i\frac{\mathrm{d}}{\mathrm{d}t}\begin{pmatrix}\tilde{c}_1\\ \tilde{c}_2\\ \tilde{c}_3\end{pmatrix} = \begin{pmatrix}\delta & \Omega & 0\\ \Omega^* & 0 & \Omega\\ 0 & \Omega^* & -\delta\end{pmatrix}\begin{pmatrix}\tilde{c}_1\\ \tilde{c}_2\\ \tilde{c}_3\end{pmatrix}. \tag{3.14}$$

The solutions to this equation have the form:

$$\begin{pmatrix}\tilde{c}_1\\ \tilde{c}_2\\ \tilde{c}_3\end{pmatrix} = \begin{pmatrix}a\\ b\\ c\end{pmatrix}\mathrm{e}^{-i\lambda_{3L}t} \tag{3.15}$$

where a, b and c are constants, and the dressed-state energies are given by:

$$U = \hbar\lambda_{3L} = 0, \pm\hbar\sqrt{\delta^2 + \frac{|\Omega|^2}{2}}. \tag{3.16}$$

The dressed-state potentials have the same form as in the two-level case but with the addition of the $\tilde{m}_F = 0$ substate level (where the tilde is used to distinguish the dressed state from the bare state) for which $U = 0$, and an extra factor of $1/2$ in the coupling term.

3.4 Landau-Zener Transitions

An important feature of dressed potentials is the possibility of non-adiabatic, so-called Landau-Zener, transitions between the different dressed states. These transitions occur at an avoided crossing, illustrated in figure 3.1, and lead to atom loss by shifting the population between trapped and untrapped dressed states. In the uncoupled basis the two energy levels are degenerate where $\delta = 0$. However,

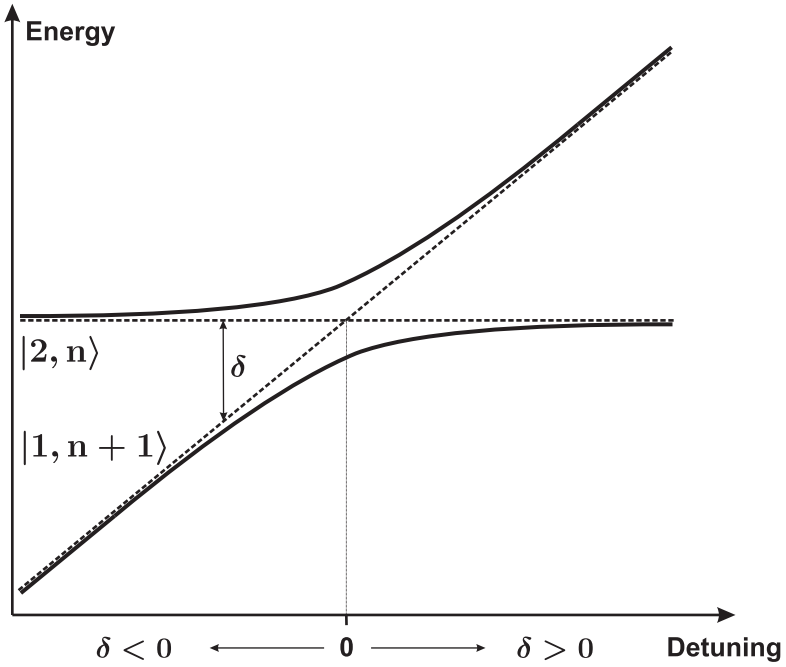

Figure 3.1: An avoided crossing between two dressed states. The uncoupled states (dashed lines) cross over at zero detuning, while, for nonzero coupling the dressed states (solid lines) are separated even at zero detuning.

when $\Omega > 0$, the two levels are never degenerate but have separation $\hbar\sqrt{\delta^2 + \Omega^2}$, giving rise to a so-called avoided crossing. Now, for sufficiently strong coupling, when the detuning is swept through the crossing the population can be transferred between the two dressed states. The probability of such Landau-Zener transitions occurring is given by [89, 90]:

$$P_{LZ} = \exp\left(\frac{-2\pi\Omega^2}{\dot{\delta}}\right). \tag{3.17}$$

This probability is highest where the coupling is at a minimum since at these points the separation between the dressed states is at a minimum. In the case of the RF-dressed potentials discussed below, Landau-Zener losses set important constraints on where atoms may be trapped in the potentials. In addition, the dependence of P_{LZ} on the rate of change of detuning sets a limit on how quickly

δ may be changed experimentally without incurring atom loss. The requirement that $P_{LZ} \simeq 0$ sets the constraint: $\dot{\delta} \ll 2\pi\Omega^2$.

A further important property of RF-dressed potentials is that the spontaneous emission is negligible relative to the coupling between the levels. This is true even on resonance and means that spontaneous emission may be neglected.

3.5 Magnetic Dressed States

The above treatment of an atom interacting with an oscillating field used a general expression for the oscillating field. In this section the specific case of the interaction of an atom with a oscillating magnetic field is elaborated. The interaction of an atom with hyperfine structure with an oscillating magnetic field arises from the Zeeman effect. The interaction energy is given by the following expression which is treated as a perturbation to the main Hamiltonian:

$$H_{int} = -\boldsymbol{\mu}.\mathbf{B} \tag{3.18}$$

where $\boldsymbol{\mu}= -g_F\mu_B\mathbf{F}$. The oscillating magnetic field may be described by the following general expression:

$$\mathbf{B} = C\cos(\omega t)\hat{\mathbf{e}}_\mathbf{x} + D\cos(\omega t - \varphi)\hat{\mathbf{e}}_\mathbf{y} + E\cos(\omega t - \phi)\hat{\mathbf{e}}_\mathbf{z} \tag{3.19}$$

where C, D and E are the amplitudes of each component and φ and ϕ are arbitrary phases.

In order to include transitions between magnetic substates, H_{int} is rewritten

using the following relations:

$$\mathbf{F}.\hat{\mathbf{e}}_\mathbf{x} = F_x \qquad \mathbf{F}.\hat{\mathbf{e}}_\mathbf{y} = F_y \qquad \mathbf{F}.\hat{\mathbf{e}}_\mathbf{z} = F_z \tag{3.20}$$

and the ladder operators:

$$F_+ = F_x + iF_y \qquad F_- = F_x - iF_y \tag{3.21}$$

to give:

$$H_{int} = \frac{1}{4} g_F \mu_B \Big(C(F_+ + F_-)(\mathrm{e}^{i\omega t} + \mathrm{e}^{-i\omega t}) - iD(F_+ - F_-)(\mathrm{e}^{i(\omega t - \varphi)} + \mathrm{e}^{-i(\omega t - \varphi)}) + EF_z \cos(\omega t - \phi) \Big). \tag{3.22}$$

The expectation value of transitions between adjacent hyperfine states, $\psi_1 = \mathrm{e}^{-i\omega_1 t}|F, m_F\rangle$ and $\psi_2 = \mathrm{e}^{-i\omega_2 t}|F, m_F + 1\rangle$, is given by the off-diagonal matrix element:

$$M_{21} = \langle F, m_F + 1|\mathrm{e}^{i\omega_2 t} H_{int}\, \mathrm{e}^{-i\omega_1 t}|F, m_F\rangle \tag{3.23}$$

$$= \frac{1}{4} g_F \mu_B \hbar c_+ \mathrm{e}^{i\omega_0 t} \left(C(\mathrm{e}^{i\omega t} + \mathrm{e}^{-i\omega t}) - iD(\mathrm{e}^{i\omega t}\mathrm{e}^{-i\varphi} + \mathrm{e}^{-i\omega t}\mathrm{e}^{i\varphi}) \right) \tag{3.24}$$

where $c_+ = (1/\hbar)\langle F, m_F{+}1|F_+|F, m_F\rangle = \sqrt{F(F+1) - m_F(m_F+1)}$ is the Clebsch-Gordon coefficient for the transition and $\omega_0 = \omega_2 - \omega_1$. The presence of an external d.c. magnetic field directed along the z-axis has been assumed in this treatment.

As in section 3.2, we may assume that the field is close to resonance so that the rotating wave approximation can be applied. Here, $\omega + \omega_0 \gg \omega - \omega_0$, and the

higher frequency term can be neglected to give:

$$|M_{21}|^2 = \left(\frac{\hbar g_F \mu_B c_+}{4}\right)^2 (C^2 + D^2 - 2CD\sin\varphi). \tag{3.25}$$

The Rabi frequency of the transition is given by $\hbar\Omega = 2M_{21}$ so that:

$$|\Omega|^2 = \left(\frac{g_F \mu_B c_+}{2\hbar}\right)^2 (C^2 + D^2 - 2CD\sin\varphi). \tag{3.26}$$

Thus, following the application of the rotating wave approximation, the matrix element and Rabi coupling between magnetic substates are time *independent*, and the system can be described as a dressed-state system.

It can be seen from equation 3.26 that only the RF components, with amplitude C and D, which are perpendicular to the assumed d.c. magnetic field along the z-direction, contribute to the coupling between substates. In this work the static magnetic field is a quadrupole field, and finding the perpendicular component of the RF is non-trivial since the quadrupole field changes direction over space. However, this can be achieved using the following steps. First, a set of basis vectors in the frame of the static magnetic field is constructed. The vector describing the RF field is then rotated into the static field basis to find the respective components in this basis. The RF field may be described by the vector:

$$\mathbf{B_{RF}} = B_0^{RF} \begin{pmatrix} \cos(\omega t) \\ \lambda\cos(\omega t - \alpha) \\ \kappa\cos(\omega t - \beta) \end{pmatrix} \tag{3.27}$$

where α and β are arbitrary phases and λ and κ are arbitrary amplitudes, with κ included to take into account a component of the RF field out of the xy-plane.

The result of this derivation, which may be found in full in [20], is:

$$\left(\frac{B_{\perp}^{RF}}{B_0^{RF}}\right)^2 = h(x, y, z, \lambda, \kappa, \alpha, \beta) \tag{3.28}$$

where $h(x, y, z, \lambda, \kappa, \alpha, \beta)$, given in equation 3.33, encapsulates the dependence of the coupling on the polarisation and amplitude of the RF. The full expression for the coupling is then given by:

$$|\Omega|^2 = \left(\frac{g_F \mu_B B_0^{RF}}{\sqrt{2}\hbar}\right)^2 h(x, y, z, \lambda, \kappa, \alpha, \beta). \tag{3.29}$$

In order to find the full expression for the dressed-state potentials given in 3.16, an expression for the detuning term must also be found. The detuning is given by $\delta = \omega - \omega_0$, where $\omega_0 = g_F \mu_B |B_{dc}|/\hbar$ and $\omega = \omega_{RF}$. The quadrupole field is described by equation 2.27, and the magnitude of this field is given by:

$$|B_{dc}| = B_q' \left(\frac{x^2 + y^2}{4} + z^2\right)^{\frac{1}{2}} \tag{3.30}$$

and hence the detuning is:

$$\delta = \omega_{RF} - \frac{g_F \mu_B}{\hbar} B_q' \left(\frac{x^2 + y^2}{4} + z^2\right)^{\frac{1}{2}}. \tag{3.31}$$

A full expression for the dressed magnetic potentials can then be found by combining equations 3.16, 3.29 and 3.31 to give:

$$U = 0, \pm\hbar \sqrt{\left(\omega_{RF} - \frac{g_F \mu_B}{\hbar} B_q' \left(\frac{x^2 + y^2}{4} + z^2\right)^{\frac{1}{2}}\right)^2 + \left(\frac{g_F \mu_B B_0^{RF}}{2\hbar}\right)^2 h(x, y, z, \lambda, \kappa, \alpha, \beta)} \tag{3.32}$$

where the full expression for $h(x, y, z, \lambda, \kappa, \alpha, \beta)$ is given by [20]:

$$\begin{aligned} h(x,y,z,\lambda,\kappa,\alpha,\beta) =& \frac{4z^2}{x^2+y^2+4z^2}\left(\frac{x^2+\lambda^2y^2}{x^2+y^2}\right) + \frac{y^2+\lambda^2x^2}{x^2+y^2} - \frac{2\lambda xy\cos\alpha}{x^2+y^2+4z^2} \\ &+ \frac{4\lambda z\sin\alpha}{\sqrt{x^2+y^2+4z^2}} + \kappa^2\frac{x^2+y^2}{x^2+y^2+4z^2} + 2\kappa\Bigg(\frac{2xz\cos\beta}{x^2+y^2+4z^2} \\ &+ \frac{2\lambda yz\cos(\alpha-\beta)}{x^2+y^2+4z^2} + \frac{\lambda x\sin(\alpha-\beta)}{\sqrt{x^2+y^2+4z^2}} + \frac{y\sin\beta}{\sqrt{x^2+y^2+4z^2}}\Bigg). \end{aligned} \tag{3.33}$$

As in the general 3-level dressed-state equation (3.16), this dressed-state potential contains two terms: a detuning term and a coupling term. As a result of the spatial variation in the magnitude of the perpendicular RF component, $B_\perp$, and the spatial variation in the quadrupole field strength, both of these terms vary in space. This gives rise to a complex trapping geometry whose key characteristics are described in the following section.

3.6 Shell Potential

The upper dressed-state potential given in equation 3.32 has a potential minimum with the form of a 3D shell. Atoms with a sufficiently low temperature may be trapped on the surface of this shell. The key feature of this potential is that the trapping frequencies across the shell may be made sufficiently large so that the atoms are in the quasi-2D regime. In this section the main characteristics of the shell potential are described, followed by a summary of the experimental work done to date using this potential. The planned extension of this work in the new experimental setup is then discussed.

3.6.1 Characteristics of the Potential

The characteristics of the shell potential can be better understood by rewriting equation 3.32 for the specific case of RF applied in the radial plane of the quadrupole potential, and including the potential due to gravitation:

$$U_{shell}(x,y,z) = mgz \pm \hbar\sqrt{(\omega_{RF} - \varrho f(x,y,z))^2 + h(x,y,z,\lambda,\alpha)\Omega_0^2} \tag{3.34}$$

where g is the acceleration due to gravity, $\varrho = \frac{g_F \mu_B B'_q}{\hbar}$ and $\Omega_0 = \frac{g_F \mu_B B_0^{RF}}{2\hbar}$. The functions $f(x,y,z)$ and $h(x,y,z,\lambda,\alpha)$ contain the spatial dependence of the detuning and coupling terms respectively. The former is set by the bare quadrupole potential and is given by:

$$f(x,y,z) = \sqrt{\frac{x^2+y^2}{4} + z^2}. \tag{3.35}$$

The function $h(x,y,z,\lambda,\alpha)$ depends upon the polarisation of the RF, and can be found by inserting the relevant constants into equation 3.33. For example, for circularly polarised light: $\lambda = 1$, $\alpha = -\pi/2$; and for RF linearly polarised along the y-direction: $\lambda = 0$, $\alpha = 0$. Since we assume the RF is applied only in the radial plane, $\kappa = 0$.

The origin of the shell trapping geometry may be understood by noting that the minimum in potential occurs where the RF radiation is resonant with the splitting of the atom's magnetic sublevels produced by the quadrupole field, such that the detuning term in equation 3.34 is a minimum. Since the quadrupole field increases in all directions away from its zero at the origin, this resonance occurs at a specific distance from the origin set by the gradient of the field, giving rise to the shell form of the potential minimum. The quadrupole field gradient along the z-axis is twice that in the xy-plane, and so the radius of the shell along the z-axis is half that in

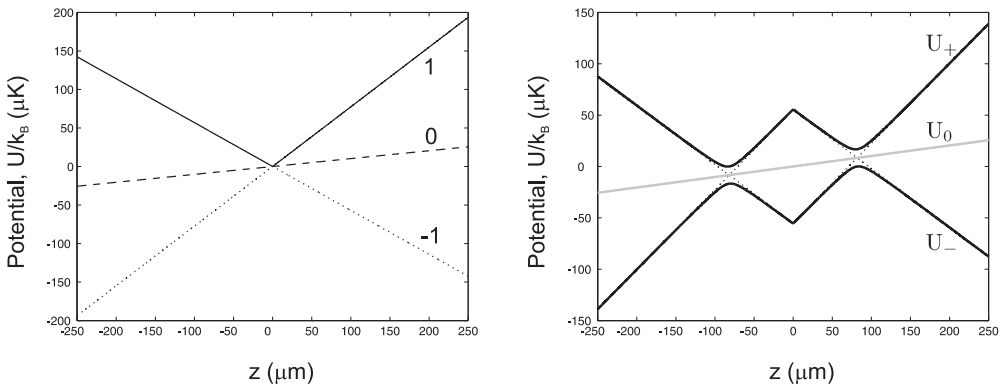

(a) (b)

Figure 3.2: The formation of the shell potential: a) bare quadrupole potentials and b) uncoupled state (dotted lines) and dressed-state (solid lines) potentials in the z-direction for all three magnetic substates of the $F = 1$ level. The other parameters are: $\omega_{RF}/2\pi = 1.15\,\mathrm{MHz}$, $B'_q = 200\,\mathrm{G\,cm^{-1}}$, $B_0^{RF} = 0.5\,\mathrm{G}$, $\lambda = 1$, $\alpha = -\pi/2$.

the xy-plane, making the shell ellipsoidal. The absolute value of the coupling term in equation 3.34 changes in space due to the variation of the orientation of the RF relative to the quadrupole field. This adds a further spatial variation to the potential on top of that given by the detuning term. In the regime considered in this work (large RF frequencies, $\omega_{RF}/2\pi > 1\,\mathrm{MHz}$, and low RF power, $B_0^{RF} < 1\,\mathrm{G}$) the detuning term is much larger than the coupling term, and so the detuning term dominates and sets the trapping geometry as the ellipsoidal shell described above. The effect of the coupling term is to modify the absolute value of the potential on the shell, to produce regions of lower potential where the trapped atoms will preferentially reside. Gravity plays a similar role, tending to pull the atoms to the bottom of the shell potential.

The case of circularly polarised RF ($\lambda = 1$, $\alpha = -\pi/2$) is illustrated in figure 3.3. If gravity is neglected, this handedness of circularly polarised RF produces a minimum of potential at the north pole of the shell where the coupling is a minimum. Figure 3.3 (a) shows the potential in the xz-plane for this polarisation

and a low RF power. Here gravity dominates and pulls the atoms to the bottom of the shell. In 3.3 (b) the RF power is greater and the increased coupling pushes atoms up around the shell towards the north pole. For the opposite handedness of circularly polarised RF ($\lambda = 1$, $\alpha = +\pi/2$), in the absence of gravity, the minimum in coupling and hence the potential minimum is at the south pole of the shell.

As discussed in section 3.4, Landau-Zener losses occur with highest probability in regions of minimum coupling. For circularly polarised RF with $\lambda = 1$, $\alpha = -\pi/2$ this is at the north pole of the ellipsoid while for circularly polarised RF with $\lambda = 1$, $\alpha = +\pi/2$ it is at the south pole of the ellipsoid. The result of this is that trapping atoms over a non-negligible timescale is impossible using RF with $\lambda = 1$, $\alpha = +\pi/2$ since the atoms are rapidly lost through Landau-Zener transitions. In the case of $\lambda = 1$, $\alpha = -\pi/2$ polarised RF, although some atom loss is incurred at the north pole of the ellipsoid, this is generally small since, for small couplings where the effect of gravity is dominant, the majority of the atoms reside near to the south pole. For this reason the $\lambda = 1$, $\alpha = -\pi/2$ polarisation was used in practice to produce quasi-2D potentials, as described in the next subsection.

The oscillation frequencies for atoms in the shell potential can be found by Taylor expanding the expression for the trapping potential about the equilibirium position. Assuming an equilibrium position at the bottom of the shell $(0, 0, z_0)$, and circularly polarised RF ($\lambda = 1, \alpha = -\pi/2$), the frequencies in the radial directions are [21]:

$$\omega_x = \omega_y = \frac{1}{2}\sqrt{\frac{g}{z_0}\left(1 - \frac{\hbar\Omega_0}{mgz_0}\right)} \tag{3.36}$$

and the frequency perpendicular to the shell surface:

$$\omega_z = \varrho\sqrt{\frac{\hbar}{2m\Omega_0}}. \tag{3.37}$$

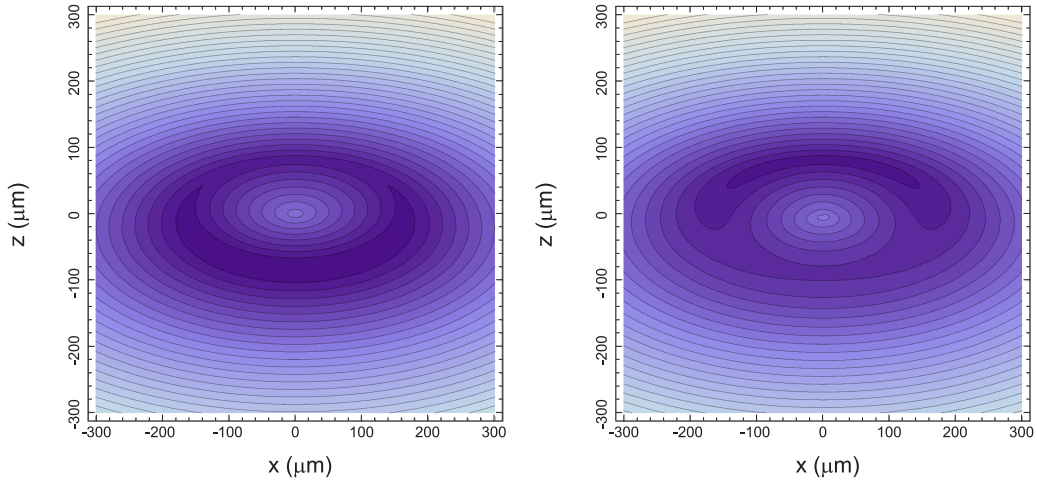

(a) (b)

Figure 3.3: A contour plot of the shell potential in the xz-plane (with dark shading representing lower potential.): a) with $B_0^{RF} = 0.25\,\mathrm{G}$, gravity dominates and pulls the atoms to the bottom of the shell, b) with $B_0^{RF} = 1\,\mathrm{G}$ the increased coupling pushes the atoms to the top of the shell. The other parameters are: $\omega_{RF}/2\pi = 1.15\,\mathrm{MHz}$, $B_q' = 200\,\mathrm{G\,cm^{-1}}$, $\lambda = 1$, $\alpha = -\pi/2$.

The condition for the potential to be quasi-2D is that ω_z should be greater than the value of $\mu/\hbar$, where μ is the 3D chemical potential of the atoms, given by equation 2.62. Then excitations can only occur in the radial direction and are frozen out in the axial direction.

The above trapping frequencies are only valid for small amplitude oscillations about the equilibrium position and when $\frac{\hbar\Omega_0}{mgz_0} < 1$, in which case there exists a trapping region at the bottom of the shell potential. For $\frac{\hbar\Omega_0}{mgz_0} > 1$ there is anti-trapping at the bottom of the shell, tending to push atoms up the sides of the shell. In the intermediate case of $\frac{\hbar\Omega_0}{mgz_0} = 1$ a quartic term is present in the trapping potential. This quartic term may be used to provide higher than harmonic confinement in experiments where the potential is rapidly rotated. This range of rotation experiments is discussed in the final chapter of this thesis.

3.6.2 Experimental Realisation

The first demonstration of an RF shell potential was made by Colombe *et al* [91] following the scheme in the original proposal by Zobay and Garraway [83]. In that experiment the exact form of the potential differed from that in equation 3.32 since the static magnetic field was a Ioffe-type field generated by a quadrupole-Ioffe configuration (QUIC) trap rather than a quadrupole field. The atoms were trapped at the bottom of the shell as a result of the pull of gravity and a trapping frequency of 600 Hz was measured in the axial direction. This frequency was sufficient to enter the quasi-2D regime, however unavoidable heating of the atoms upon loading into the potential prevented the creation of a BEC.

This work was expanded upon using the old experimental apparatus in this group. This work is presented in the thesis of Eileen Nugent [21] where a shell potential of the form given in equation 3.34 was created by dressing a bare quadrupole field. The RF was generated using the same two pairs of Helmholtz coils that were used to generate the bias field for the TOP trap. The objective was also to create a BEC in the quasi-2D potential formed at the bottom of the shell.

With circularly polarised RF with $B_0^{RF} = 0.21\,\mathrm{G}$ and $B'_q = 388\,\mathrm{G\,cm^{-1}}$, the axial and radial frequencies were measured to be $725 \pm 14\,\mathrm{Hz}$ and $19.85 \pm 0.37\,\mathrm{Hz}$ respectively, in close agreement with the predictions of equations 3.36 and 3.37. Approximately 30,000 atoms were trapped in this potential, and for this number and these frequencies, equation 2.62 gives a value for the chemical potential, $\mu/\hbar = 685\,\mathrm{Hz}$. This figure is less than the axial trapping frequency indicating that the system was in the quasi-2D regime.

The formation of a BEC in the shell trap in the old experiment was assisted by the following spontaneous evaporative cooling mechanism. With the circularly polarised RF ($\lambda = 1$, $\alpha = -\pi/2$) used in this experiment Landau-Zener losses

occur with probability one at the north pole of the shell potential. The probability of losses progressively decreases towards the south pole where it is equal to zero. As a result, hotter atoms, which can sample the region around the north pole preferentially undergo Landau-Zener losses. By contrast, colder atoms are held close to the bottom of the shell by gravity and are not lost from the trap. This results in spontaneous evaporation of hotter atoms from the shell trap and reduces the average temperature sufficiently to produce a BEC at the bottom of the shell. The presence of a condensate was confirmed through the highly anisotropic expansion of the atom cloud following release from the trap [21].

The results from the old experiment also matched well the predictions for the distribution of atoms over the shell for different polarisations of RF. The interplay between the effects of gravity and coupling on the distribution of atoms on the shell was as expected. With circularly polarised RF ($\lambda = 1$, $\alpha = -\pi/2$) of low power, the atoms were pulled to the bottom of the shell by gravity. With increasing RF power the coupling was sufficient to overcome the pull of gravity and push the atoms all the way around the shell, as in figure 3.3.

3.7 Ring Potential

3.7.1 Characteristics of the Potential

The above shell potential is generated by dressing a spherical quadrupole static magnetic field. An alternative, ring-shaped trapping geometry may be created by instead dressing a *biased* quadrupole field. This was first demonstrated in the old apparatus in this group [19], in which a ring-shaped potential was formed by combining an RF-dressed shell potential with an optical dipole potential. This particular trapping scheme was proposed by Morizot *et al* [92].

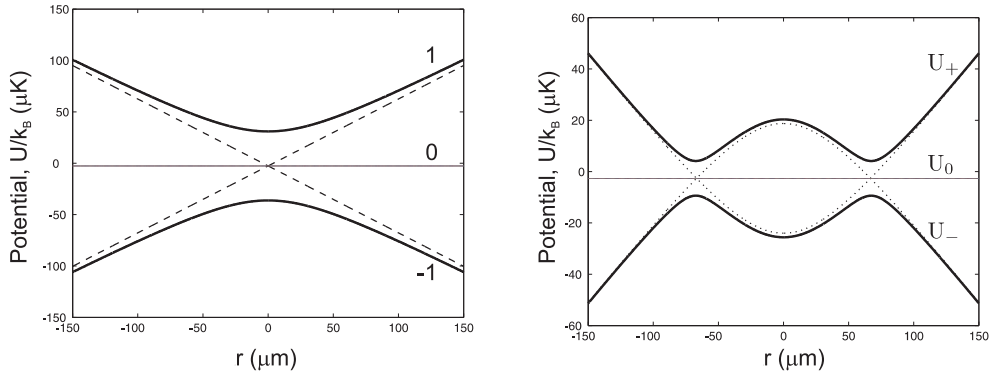

(a) (b)

Figure 3.4: The formation of the ring potential: a) quadrupole potential (dashed lines) and biased quadrupole potential (solid lines), b) uncoupled state (dotted lines) and dressed-state (solid lines) potentials in the radial direction for all three magnetic substates of the $F = 1$ level. The other parameters are: $\omega_{RF}/2\pi = 1.15\,\mathrm{MHz}$, $B'_q = 388\,\mathrm{G\,cm^{-1}}$, $B_0^{RF} = 0.25\,G$, $B_{dc} = 1\,\mathrm{G}$, $\lambda = 1$, $\alpha = -\pi/2$.

The biased quadrupole potential was formed in the following way. First, an ultracold cloud of atoms was formed in the TOP trap. The atoms were then trapped in the xy-plane by ramping up an optical dipole potential in which the atoms were trapped between two sheets of blue-detuned light (further details of this dipole potential may be found in [20] and [21]). The centre of the TOP trap was then biased upwards away from the atoms using a static magnetic bias field, and the TOP bias field was ramped off to leave the atoms in a biased quadrupole potential. The dressing RF field was then ramped on to create a shell potential located above the plane of the atoms. Finally, the static bias field was ramped down so that the plane in which the atoms were held intersected with the shell potential. The atoms were then trapped in a horizontal slice through the shell, which has the form of a ring-shaped potential.

The atoms in the dipole potential reside at a distance z_0 from the centre of the quadrupole potential. For a static bias field, B_{dc}, this distance is given by $z_0 = B_{dc}/B'_q$. The magnitude of the biased quadrupole field at the location of the

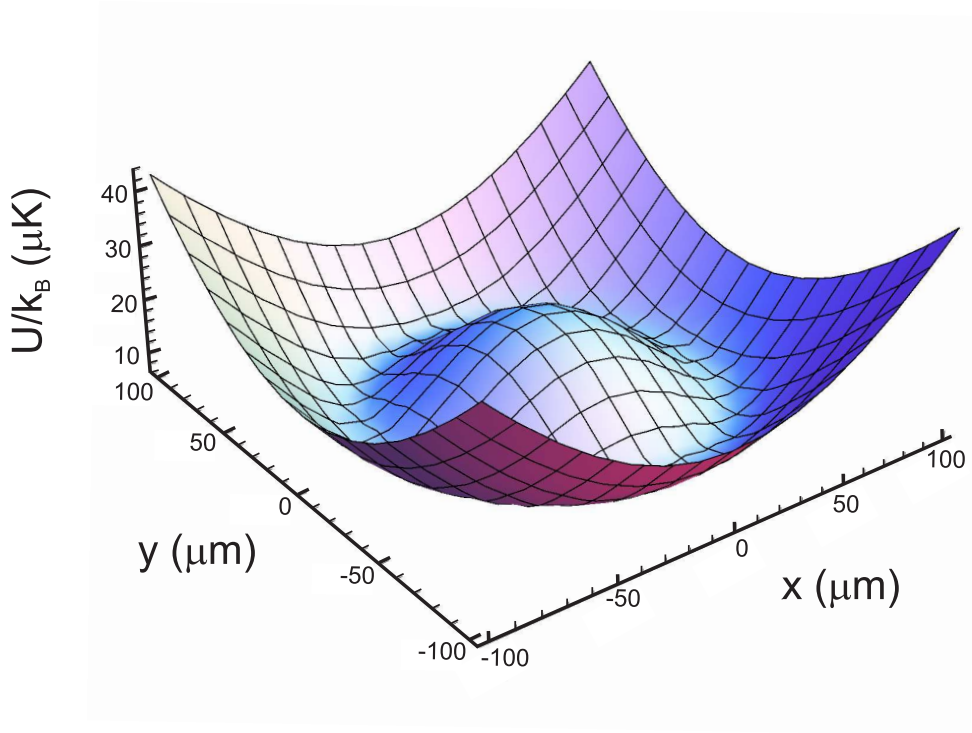

Figure 3.5: The upper dressed-state potential in the xy-plane for typical parameters used in the old experiment: $\omega_{RF}/2\pi = 1.15\,\mathrm{MHz}$, $B_q' = 388\,\mathrm{G\,cm^{-1}}$, $B_0^{RF} = 0.25\,G$, $B_{dc} = 1\,\mathrm{G}$, $\lambda = 1$, $\alpha = -\pi/2$.

atoms is then:

$$|\mathbf{B_{bq}}| = B_{dc}\left(1 + \frac{x^2 + y^2}{4{z_0}^2}\right)^{\frac{1}{2}}. \tag{3.38}$$

This expression can be used to find the value of the detuning term in the dressed-state potential:

$$\delta = \omega_{RF} - \frac{g_F \mu_B}{\hbar} B_{dc}\left(1 + \frac{x^2 + y^2}{4{z_0}^2}\right)^{\frac{1}{2}}, \tag{3.39}$$

leading to the following expression for the dressed-state potentials:

$$U = 0, \pm\hbar\sqrt{\left(\omega_{RF} - \frac{g_F \mu_B}{\hbar} B_{dc}\left(1 + \frac{x^2 + y^2}{4{z_0}^2}\right)^{\frac{1}{2}}\right)^2 + \left(\frac{g_F \mu_B B_0^{RF}}{2\hbar}\right)^2 h(x, y, z, \lambda, \kappa, \alpha, \beta)}. \tag{3.40}$$

If the coupling term in equation 3.40 is neglected then the radius of the ring is

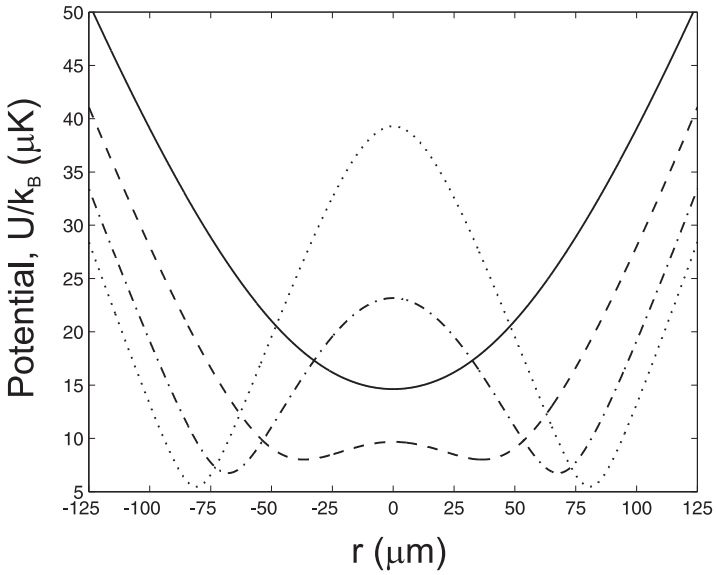

Figure 3.6: The effect of changing B_{dc} on the radius of the ring trap. The values of B_{dc} are: 0.5 G (dotted line), 1 G (dash-dot line), 1.5 G (dashed line), and 2 G (solid line). The other parameters are: $\omega_{RF}/2\pi = 1.15$ MHz, $B_q = 388\,\mathrm{G\,cm^{-1}}$, $B_0^{RF} = 0.25\,G$, $B_{dc} = 1$ G, $\lambda = 1$, $\alpha = -\pi/2$.

given by:

$$r^2 = \left(\frac{2\hbar\omega_{RF}}{g_F\mu_B B_q'}\right)^2 - 4\left(\frac{B_{dc}}{B_q'}\right)^2. \tag{3.41}$$

Therefore the ring radius is set by three parameters: ω_{RF}, B_q' and B_{dc}. The value of ω_{RF} and B_q' fixes the radius of the shell potential whilst B_{dc} fixes the z position at which the plane of the atoms intersects the shell. The tunability of the ring radius was demonstrated in the old experiment by varying B_{dc} whilst keeping ω_{RF} and B_q' fixed, and the results matched the predictions with a slight offset which could be accounted for by a miscalibration of either the imaging system or quadrupole field gradient [21]. The cross-section of the upper dressed-state potential is shown in figure 3.6 for various values of B_{dc}, with circularly polarised RF ($\lambda = 1$, $\alpha = -\pi/2$). The formation of a BEC in the ring trap was confirmed through the anisotropic expansion of the cloud upon release from the trap [21].

3.7.2 Rotation in the Ring Potential

A Bose-Einstein condensate in the multiply-connected topology of a ring-shaped potential has qualitatively different superfluid properties than in the simply-connected topology of a standard harmonic potential. In particular, when angular momentum is transferred to a condensate in a ring potential it will undergo frictionless flow around the ring [88]. This flow, commonly referred to as a persistent current in analogy with the persistent flow of electrical current around a loop of superconductor, will continue indefinitely provided the trapping potential is conservative. In contrast, for a BEC in a simply-connected potential, the addition of angular momentum results in irrotational flow through the formation of vortices. Persistent currents are one of the key hallmarks of superfluidity and could serve as a means of better understanding the fundamental relationship between Bose-Einstein condensation and superfluidity.

Ryu *et al* first demonstrated persistent flow of a BEC in a ring-shaped potential in 2007 [93]. In that experiment, orbital angular momentum was transferred to the atoms using a Laguerre-Gaussian laser beam. In the old experiment in this group two schemes for rotating the atoms in the ring trap were demonstrated, both relying on the time variation of the RF dressing fields [21]. The first of these, the *barrier rotation* scheme, uses two superimposed circularly polarised RF fields of opposite handedness which differ in frequency by $\tilde{\delta}$. The resultant field is linearly polarised and introduces two barriers across the ring. The plane of polarisation, and hence the axis of the barriers, rotates at a frequency $\tilde{\delta}/2$, stirring the atoms into a flow around the ring. The second scheme, the *gold-pan rotation* scheme, involves adding in a z-component of RF to tilt the ring potential out of the xy plane. Atom flow is induced by detuning the oscillation frequency of the z-component relative to that of the x- and y-components such that the tilt axis of the ring rotates at a

chosen frequency.

Both rotation schemes were demonstrated in the ring potential using a thermal cloud of atoms at a temperature of approximately 700 nK [21]. However, as yet in our group, rotation of a condensate in the ring potential to produce a persistent current has not been achieved. One aim in the new experiment is to produce a persistent current, and use this to study superfluidity in the quasi-1D and quasi-2D regimes.

3.8 Time-Averaged Adiabatic Potential

In 2007 a novel type of trapping potential, the time-averaged adiabatic potential (TAAP) trap, was proposed [94]. The TAAP trap combines the time-averaging approach used to create the TOP trap with the RF dressing approach described in the previous sections. This combination allows a large variety of trapping geometries to be generated using a relatively simple set of magnetic coils. The range of potentials is increased over those obtainable using RF dressing alone, and the typical trapping frequencies are larger. As with RF-dressed potentials, the geometry of the potentials may be morphed adiabatically by changing the trapping parameters. The TAAP trapping scheme has now been demonstrated successfully in the new apparatus [95].

The TAAP scheme in our experiment involves RF dressing a TOP potential. The instantaneous field in the TOP trap is a quadrupole potential and thus RF-dressing results in the shell potential described above. The rotating TOP bias field then time-averages the shell potential in the manner illustrated in figure 3.7. As in the formation of the TOP trap, the condition for time-averaging is that the variation of the bias field should occur on a timescale that is greater than the trapping frequencies but much smaller than the Larmor frequency of the atom:

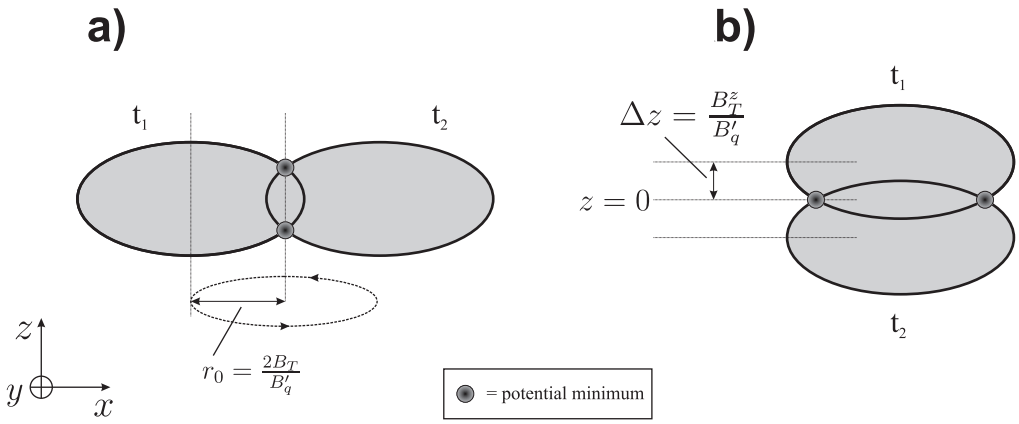

Figure 3.7: Schematic of the time-averaged adiabatic potential (TAAP) trap. a) Double-well potential formed by rotation of the RF-dressed shell potential in the xy-plane. b) Ring potential formed by vertical modulation of the shell potential position, where B_T^z is the amplitude of the TOP field in the axial direction. In each case the shell is shown at the two extrema (t_1, t_2) of the time-averaging cycle.

$|g_F \mu_B B_{bias}/\hbar| \gg \omega_{bias} > \omega_{trap}$. The dressed magnetic field then moves slowly enough for the atoms' magnetic moment to stay aligned with the local field, but quickly enough that the atoms cannot follow the field kinematically, and thus see a time-averaged field.

In the original TAAP proposal two trapping geometries were considered: a ring potential and a double-well potential. Both result from time-averaging a shell potential which can be formed by RF dressing either a Ioffe-Pritchard potential or a quadrupole potential, as outlined in section 3.6. The shell potential is time-averaged by modulating its position in either the radial or axial directions of the static field using a time-varying bias field. Radial modulation gives rise to a double-well potential, while axial modulation produces a ring-shaped potential.

For our purposes, modulation in the radial direction can be achieved using the TOP bias field given in equation 2.28. The separation of the two wells in the resulting time-averaged potential is set by the points at which the shell potential intersects the rotation axis, and increases as the TOP field amplitude, B_T, is decreased. For a large enough B_T the double wells merge into a single well.

A modulation in the axial direction can be applied using an additional pair of TOP Helmholtz coils placed along the axial direction. The radius of the resulting ring potential can be adjusted by changing the amplitude of the modulation. With typical trapping parameters, trapping frequencies across the ring of up $\sim 1\,\mathrm{kHz}$ can be achieved. Both the double-well and the ring TAAP traps have been demonstrated experimentally in the new apparatus [95].

A further case of interest is the potential formed by applying a small radial modulation to the standard shell potential. This produces a shell potential with a similar axial frequency as the potential in section 3.6 but with a larger radial trapping frequency. Such a potential is ideally suited to a further line of research intended to be carried out in the new apparatus: the rapid rotation of condensates, for which enhanced radial confinement is advantageous. Further details of this experiment are given in the final chapter of this thesis.

3.9 RF Requirements for the New Apparatus

The aim in the new apparatus was to increase the range of RF trapping parameters over those in the old apparatus to broaden the scope of possible experiments using RF-dressed potentials. In particular, an increased maximum axial trapping frequency was desirable to permit the trapping of a greater number of atoms in the quasi-2D regime. In order to achieve this increase in trapping frequency the maximum value of the quadrupole gradient, B'_q, had to be increased over its value in the old experiment. The axial trapping frequency may also be increased by using a larger value for the RF frequency, ω_{RF}, than the 1.15 MHz used in the old experimental setup, and for this reason it was desirable to include the capability of generating a number of different RF frequencies in the new experiment. In addition, a larger maximum RF amplitude, B_0^{RF}, was planned to increase the strength

of the RF coupling.

In order to allow these improvements, it was necessary to rebuild the final magnetic coil array to include purpose-built RF coils. This would extend the capabilities of the old experimental setup where the RF was applied using the TOP bias coils which were not optimised for this purpose. In addition, separate RF and TOP coils would allow more complex trapping potentials such as the TAAP trap, outlined in section 3.8, to be created. The technical details of the new magnetic coil assembly are given in subsection 5.7.1. In addition to these changes to the magnetic coil assembly the new apparatus was designed around the inclusion of a high resolution imaging system. This system was designed to provide sub-micron resolution primarily for experiments with small atom numbers such as the planned fast rotation experiment. Further details are provided in subsection 5.8.3.

Chapter 4

New Apparatus Design

4.1 Requirements for the New Apparatus

The first experiments using ultracold atoms in RF-dressed potentials in this group [19–21] were carried out using an experimental apparatus which was built in 1998 and produced Oxford's first BEC [52]. As a consequence, several elements of the apparatus were designed with older experiments in mind, which meant it was not ideally suited to continuing the studies of atoms in RF-dressed potentials or the more demanding proposed experiments involving the imaging of small numbers of atoms in rapidly rotating potentials, outlined in the final chapter. This chapter describes the design and construction of a new apparatus intended to increase the scope of possible experiments. The following were the key requirements for the new apparatus:

Imaging: The principal modification to the apparatus was the incorporation of an improved vertical imaging system. The required specifications of this system

were set by the experiments to be carried out in the new apparatus. First, the in-trap imaging of condensates in the toroidal and ellipsoidal RF-modified potentials. Second, the fluorescence imaging of small atom numbers in the proposed fast rotation experiment. The typical length scales in these experiments demanded an imaging system with a spatial resolution of one micron or better.

Optical access: In addition to the space required for the vertical imaging system, good optical access to the experimental cell was necessary to allow entry of the laser beams which will be used to create dipole potentials for atom confinement. First, the blue-detuned dipole potential used to give quasi-2D confinement in the RF-trapping experiments [21] and second, the red-detuned lattice beams that will ultimately be used to trap atoms during imaging at the end of the proposed fast rotation experiments.

Trapping frequencies: In order to generate the proposed trapping geometries discussed in chapter 3, larger trapping frequencies than those obtainable in the old experiment were required. These trapping frequencies are set by the magnitude of the magnetic field gradient generated by the final magnetic trapping coils: the quadrupole potential outlined in subsection 2.3.1. To give the required increase in trapping frequencies an axial gradient of $1000\,\mathrm{G\,cm^{-1}}$ was chosen for this quadrupole field in the new experiment, compared to the maximum value of $388\,\mathrm{G\,cm^{-1}}$ in the old experiment [21]. This increase in gradient was brought about by making two changes to the anti-Helmholtz coil pair compared to that used in the old apparatus. First, the coils were designed to carry a much higher current than previously: $\sim 300\,\mathrm{A}$ compared to $\sim 10\,\mathrm{A}$. Second, the radii and separation of the coils were reduced.

RF dressing field: In the old experiment, because of spatial constraints, the dressing RF was applied using the same coils used to generate the rotating bias field of the TOP trap. In the new system separate TOP and RF coils were required to allow these coils to be each optimised for their specific function. In particular, a higher RF power and the possibility of generating different frequencies of RF were desirable to increase the scope of the RF-dressed potential experiments.

The above points were impossible to fulfil in the original apparatus since the site of the six-beam MOT, in which the atoms were initially cooled and collected, was also the site of BEC production. To allow access for the six large MOT beams, considerable free space must be left around the experimental cell and the proposed high resolution vertical imaging optics, and the new smaller anti-Helmholtz coils, could not be installed on the system without impinging on this space.

Therefore, to create access for the imaging optics and dipole trap beams, and to create space for moving the final magnetic trapping coils closer to the cell, the position of the MOT needed to be spatially separated from the site of BEC production. This is a feature which has become common in the latest generation of BEC experiments. In such apparatuses the atoms are moved between the MOT and the site of BEC production inside a moving magnetic potential, in a stage of 'magnetic transport'.

A major part of this thesis concerns the design, construction and optimisation of such a system for magnetically transporting atoms between the MOT and the site of BEC production. In addition, the scheme for initially capturing atoms was simplified with respect to the original scheme; employing a single large MOT rather than a double MOT. The philosophy behind the MOT design was to collect

large numbers of atoms in a short amount of time to allow rapid, reliable BEC production. The design of the MOT and final magnetic trap was also contingent upon the particular transport scheme that would be used, and so which approach to take to atom transport was the first consideration in the design process.

The following section contains an overview of the different methods that have been developed for transporting ultracold atoms. This is followed by a discussion of the relevant physical processes which must be considered when designing and optimising such a system. The technical details of the new apparatus are presented in the next chapter.

4.2 Review of Approaches to Atom Transport

4.2.1 Preliminary Atom Transport

The first attempts to transport ultracold atoms were motivated by the desire to move atoms out of the high vapour pressure of the MOT and into a region of higher vacuum, where precision spectroscopy and Bose-Einstein condensation would be easier to carry out. The experiments involved launching atoms out of a MOT by changing the frequency of the upward and downward laser beams to create an upward moving polarisation gradient [96]. This 'moving molasses' launches a ballistically expanding moving cloud of atoms, which forms an atomic fountain (the atomic fountain is now used in the highest precision atomic clocks). Unfortunately, the expansion of the atom cloud results in a drop in phase space density. This drop in phase space density can be reduced by using a conservative guiding force which takes the form of either an optical or a magnetic force [97, 98]. However, it cannot be eliminated altogether without recourse to a second MOT to re-cool and compress the atoms after transport, in the so-called double MOT scheme [99]. For

our purposes however, whilst the double MOT system provides a low pressure site for BEC production, it still necessitates surrounding this site with the many optics and coils needed to create a MOT and thus does not allow the required optical access to the atoms. For this, full adiabatic transport of the ultracold MOT atoms must be employed. This approach forms the basis of the following three techniques.

4.2.2 Overlapping Anti-Helmholtz Coils

The first demonstration of magnetic atom transport took place in Munich and employed a chain of overlapping anti-Helmholtz coil pairs to move the atoms approximately 30 cm from the MOT to the experimental cell around a 90° bend, and was motivated by the need to add in dipole beams to form an optical lattice, and to allow simultaneous MOT operation and BEC production [22]. By ramping the current simultaneously in three pairs of overlapping coils the axial field gradient in the vicinity of the atoms was kept constant at $130\,\mathrm{G\,cm^{-1}}$ throughout the transport sequence. In addition, the magnetic trapping potential underwent minimal geometric deformation, with any changes occurring on an adiabatic timescale. This meant that, unlike in the initial attempts at transport outlined above, the temperature and phase space density of the cloud remained almost constant throughout transport, and there was no need for a second MOT for atom cooling and recompression.

4.2.3 Moving Anti-Helmholtz Coils

The second approach to magnetic transport was first demonstrated at JILA and used a single pair of anti-Helmholtz coils to provide both the MOT field and the field for transporting the atoms [100]. These coils were translated between the MOT and the experimental cell using a commercial translation stage. As in the

above approach, the temperature and phase space density of the cloud remained almost constant throughout transport. In both of these experiments atom clouds were transported at temperatures of approximately 100 μK and then further cooled following transport to produce BEC.

4.2.4 Moving Optical Dipole Potential

A non-magnetic means of transport was demonstrated at MIT using an optical dipole potential rather than a magnetic potential to transport the atoms [101]. Since the depth of optical dipole potentials is typically much less than that of magnetic potentials, in this scheme the atoms must be much colder before transport than in the above two magnetic schemes. In fact, in the MIT experiment, the atoms were already Bose-condensed upon loading into the dipole potential. Consequently the constraints on atom transport in an optical dipole potental are much more stringent: heating must be reduced to tens of nanokelvin so that the atoms remain confined in the shallow dipole potential. In particular, the dipole potential, formed by tightly focussing an infrared beam, must provide very tight confinement to avoid heating of the atoms when the potential is translated. Also, a high degree of smoothness and precision of translation of the potential is required, which is achieved, as in the moving coils approach, by using a commercial translation stage. The more stringent constraints involved in transporting using an optical dipole potential versus a magnetic potential mean that the magnetic approach to transport is more straightforward to implement and has become more widely adopted. In our case, since, prior to transport, the atoms were to be captured in a MOT at a relatively high temperature corresponding roughly to the Doppler limit, magnetic transport was chosen as the more suitable approach.

4.2.5 Hybrid System

The decision of which magnetic transport scheme to use in our apparatus was based on two considerations: the need to accommodate the high resolution imaging optics next to the science cell, and the time required to build and set up the necessary hardware in each case. In terms of hardware, the overlapping coils approach is the more complex since several pairs of magnetic coils must be made, rather than the single pair used in the moving coils approach. In addition, the current through each coil must be regulated independently for which a relatively complex high current switching circuit must be constructed. By contrast, the translation stage for the moving coil approach is commercially available and relatively simple to control using a computer interface, and the control electronics for the magnetic coils are simpler since they need only control a single current. It was decided, therefore, that the moving coils approach would be faster to implement.

Accommodating the high resolution imaging system added a further constraint to the design since to image in the vertical direction the axis of the imaging path containing the imaging optics must cut through the horizontal planes above and below the cell. This impinges on the space required for bringing in moving coils to the site of BEC production. We decided, therefore, to use a hybrid transport system which first uses the less complex moving magnetic coils scheme to move the atoms the bulk of the distance to within a few centimetres of the position of the final magnetic trap, and then overlapping coils to shift the field zero over the last few centimetres into the final magnetic trap. In this design the moving coils do not impinge on the imaging path which passes uninterrupted through the centre of the final fixed pair of coils.

The planned implementation of the hybrid transport system involved two stages:

1. Use the moving coils alone to move the atoms all the way to the final magnetic

trap position. Optimise this system to give sufficiently efficient atom transfer such that BEC can be produced.

2. Use the hybrid system: first transport in the moving coils and then transport the final few centimetres in the fixed coils. Optimise the full system such that BEC can be produced.

By starting with the first stage the atom transport process could be characterised and shown to produce BEC. Then, the full hybrid system could be brought online, to allow installation of the high resolution imaging system. The results presented in this thesis describe the completion of the first stage and initial testing of the second. The high resolution imaging system has yet to be installed but the proposed system is outlined in subsection 5.8.3.

4.3 Physical Considerations for Atom Transport

In transporting a cloud of ultracold atoms the key criterion is minimising the incurred increase in phase space density and atom loss such that the initial conditions of the cloud of atoms are preserved as closely as possible. To achieve this, changes to the trapping potential must be minimised and if present must occur on an adiabatic timescale to avoid heating of the atoms. The confinement frequency should remain approximately constant to preserve atom density, since even adiabatic compression will result in an increase in atom temperature. In addition, any losses from the trap should be minimised. Below is a discussion of these key parameters and their optimisation.

4.3.1 Support Against Gravity and Acceleration

The atom confinement provided by the magnetic transport potential must be sufficient both to support the atoms against gravity and to keep the atoms in the potential when it is accelerated horizontally (i.e. in the xy-plane). The magnetic field produced by the transport coils is a spherical quadrupole field, whose form is given in equation 2.27. The potential energy of the atoms in this field can be found using equation 2.25, and the force on the atoms is given by the differential of this potential. Taking the magnetic force on the atoms in the vertical direction, $-\frac{dU}{dz}$, and equating it with the force due to gravity, mg, gives the minimum field gradient required to support the atoms against gravity:

$$B_{min}^{Grav} = \frac{mg}{g_F m_F \mu_B} \tag{4.1}$$

where g is the acceleration due to gravity. For atoms trapped in the $|\mathrm{F} = 1, m_F = -1\rangle$ magnetic substate this gives an axial gradient of $B'_q = 30.5\,\mathrm{G\,cm^{-1}}$ and a radial gradient of half this value. Similarly, calculating the magnetic force in the radial plane allows the minimum magnetic field gradient required to keep the atoms confined for a given horizontal acceleration, A_{Horiz}, to be found:

$$B_{min}^{Horiz} = \frac{2mA_{Horiz}}{g_F m_F \mu_B}. \tag{4.2}$$

For an acceleration of $10\,\mathrm{m\,s^{-2}}$, which is the typical maximum acceleration for the type of commercial translation stages used to transport atoms [100], the above equation gives a minimum axial field gradient, $B'_q = 62.1\,\mathrm{G\,cm^{-1}}$.

In the experiments in this thesis a quadrupole field with an axial gradient of $B'_q = 150\,\mathrm{G\,cm^{-1}}$ was used for transporting the atoms, sufficient both to support the atoms against gravity and confine them horizontally at the maximum moving

coil acceleration.

4.3.2 Adiabatic Movement

In order to avoid parametric heating of the atoms during transport three parameters must remain constant or change on an adiabatic timescale with respect to the trapping frequency. These are: the centre of the trapping potential, the trap aspect ratio, and the trap gradient [102].

In the moving coil transport scheme the trap centre is fixed by the coil geometry and the magnetic gradient produced by the coils. The smoothness of operation of commercial translation stages ensures that vibrations of the coils are negligible, and thus any change in the trap centre occurs on only the macroscopic length scale and adiabatic timescale defined by the travel of the stage. The trap aspect ratio is also fixed by the quadrupole form of the field generated by the coils, and will not change provided no other magnetic field impinges on the vicinity of the trapping field. Thus, the only parameter which can introduce heating in the moving coils approach is the horizontal movement of the transport potential along the transport axis. To minimise this heating the deceleration of the atoms at the end of the transport sequence should be sufficiently slow to avoid transferring to the atoms the momentum imparted during the acceleration at the start of transport.

In the overlapping coils atom transport scheme the trapping gradient and aspect ratio can only be kept constant by ramping the current in three pairs of overlapping coils simultaneously [22]. In this way, the trap aspect ratio can be kept constant along the whole chain of overlapping quadrupole coils. However, at the start and end of the chain of coils, where the atoms are loaded from the MOT or into the final magnetic trap, a change in aspect ratio is incurred since only the fields from two coils are used to create the trapping potential. The result is an elliptical

potential with stronger trapping frequencies in one radial direction than the other. A solution to this problem, used in the original Munich experiment, is to use a 'push' coil whose axis lies on the transport axis. The field from this coil exerts a horizontal force on the atom cloud which moves it between the fields generated by the two quadrupole coil pairs (e.g. the MOT coils and the first coil pair in the transport chain). Transferring the atoms in this way results in a much smaller change in cloud aspect ratio compared to that incurred when ramping the fields in the two quadrupole coils alone.

In another experiment which used an overlapping coils transport system, an adiabatic change in aspect ratio from 1 to 1.69 and then to 3.29 was incurred at the start and end of the transport respectively (an aspect ratio greater than one indicates elongation of the atom cloud along the direction of transport) [103]. A push coil was used to move the atoms out of the MOT coils magnetic field into the quadrupole coil chain. Approximately one half to one third of the atoms in the MOT were transported to the final magnetic trap with a temperature increase of approximately $100\,\mu$K relative to the initial value, which demonstrates that even relatively large changes in aspect ratio do not lead to significant heating provided the changes occur on an adiabatic timescale. In the experiment in this thesis, the push coil specified in section 5.5 was used to move the atoms between the field generated by the moving transport coils and that generated by the first pair of fixed quadrupole coils (the Auxiliary coils detailed in section 5.5).

4.3.3 Loss Mechanisms

Majorana spin flips

As detailed in subsection 2.3.1, the zero of magnetic field at the centre of the quadrupole potential leads to atom losses through Majorana flops. The lifetime of

the cloud set by these losses is given by [42]:

$$\tau = \frac{1}{4}\xi\sigma_{FWHM}^2 \tag{4.3}$$

where $\xi = 3.8 \times 10^4\,\mathrm{s\,cm^{-2}}$ is experimentally determined [42], and σ_{FWHM} is the full-width-half-maximum diameter of the cloud.

The radius of the cloud in the quadrupole potential can be estimated by equating the interaction energy of an atom's magnetic dipole at this radius with the thermal energy of the atom at the average cloud temperature, T. This leads to a radial cloud diameter:

$$\sigma_{quad} = \frac{2k_B T}{g_F m_F \mu_B B'_q}. \tag{4.4}$$

As the atom temperature decreases, the atoms spend longer in the central region of the trap, therefore the lifetime of atoms in the quadrupole potential decreases as their temperature decreases. The minimum value for the lifetime given by equation 4.3 may be estimated by assuming that T is the minimum realistic temperature that can be attained after loading the magnetic trap. Since the atom cloud in our MOT is large and therefore dominated by Doppler forces, a reasonable estimate of this minimum temperature is the Doppler limit, $146\,\mu$K. At this temperature, for atoms in the $|\mathrm{F} = 1, m_F = -1\rangle$ substate, and at a typical axial transport magnetic gradient of $150\,\mathrm{G\,cm^{-1}}$, the cloud diameter, σ_{quad}, is 0.06 cm and the lifetime in the quadrupole potential is $\sim 32\,$s. Typical transport times are approximately 2 to 3 s, therefore losses due to Majorana spin flips during atom transport are negligible.

Collisional losses

Collisional atom losses are incurred through three processes: three- and two-body collisions between trapped atoms, and one-body collisions between a trapped atom

and a background gas molecule. In three-body collisions, two atoms combine to form a dimer molecule and the third carries away the released energy and is lost from the trapping potential. The per atom loss rate is given by:

$$R_{3-body} = -L_{3-body} n^2 \tag{4.5}$$

where $L_{3-body} = 4 \times 10^{-30}\,\mathrm{cm}^6\,\mathrm{s}^{-1}$ for ^{87}Rb, and n is the atom density (cm^{-3}) [104].

A maximum value for the atom density in the transport potential can be estimated by again assuming an atom temperature of 146 μK after loading into the transport potential. At this temperature, and assuming a transport gradient, $B'_q = 150\,\mathrm{G\,cm}^{-1}$, the typical atom density is $10^{10}\mathrm{cm}^{-3}$. This corresponds to a negligible three-body loss rate, $R_{3-body} = -4 \times 10^{-10}\,\mathrm{s}^{-1}$.

Two-body collisions cause atoms to undergo spin-flips to untrapped magnetic substates. An upper bound for the two-body rate constant for atoms in the $|\mathrm{F} = 1, m_F = -1\rangle$ substate of ^{87}Rb has been measured to be $1.6 \times 10^{-16}\mathrm{cm}^3\,\mathrm{s}^{-1}$ [105].

One-body collisions of magnetically trapped atoms with residual background gases in the vacuum system result in an exponential decay in atom number. The time constant of this exponential decay is inversely proportional to the background pressure in the system. The relatively high vapour pressure in the MOT chamber, around 10^{-9} Torr, limits the cloud lifetime to a measured value of $1.68 \pm 0.02\,\mathrm{s}$ in this chamber. In the science chamber a pressure of around 10^{-11} Torr gives a measured lifetime of $109 \pm 12\,\mathrm{s}$. Thus, to limit the losses due to background gas collisions the time spent in the MOT chamber should be minimised. The initial approach was to accelerate the atoms as quickly as possible out of the MOT chamber, whilst ensuring that this acceleration was performed sufficiently smoothly to avoid heating of the atoms.

Collisions with the Vacuum System

The final potential loss mechanism is collisions of the atoms with the walls of the vacuum system during the transport sequence. Such losses have been reported in other transport experiments and should be reduced through consideration of the vacuum system design. The most likely site for atom losses is the narrow differential pumping tube which must be present to reduce the conductance between the MOT chamber and the science chamber and maintain a differential in pressure between these two regions (see section 5.1). Since the diameter and length of this tube fix its conductance and hence the pressure differential, an important point to consider is the size of the atom cloud in the transport magnetic potential, as this sets the minimum diameter which may be used for the differential pumping tube.

The widths of the cloud in the quadrupole potential can be estimated using equation 4.4. An average atom temperature of 500 μK was assumed, based on some heating of the atoms during transfer from the MOT into the transport potential. Assuming $B'_q = 150\,\mathrm{G\,cm^{-1}}$ and $m_F = -1$, gives a cloud diameter, $\sigma_{quad} = 2.0\,\mathrm{mm}$ in the xy-plane, and half this value in the axial direction. To accommodate this cloud, with some allowance for misalignment of the vacuum system along the transport path, a minimum diameter of 1 cm was chosen for the differential pumping tube.

In addition to atom loss through collisions with the walls of the vacuum system, stray magnetic fields from sections of the vacuum system can induce atom loss through spin flips into untrapped magnetic substates or through induced heating. Therefore the designs for the sections of the vacuum system through which atoms pass during transport used materials with little or no permanent magnetisation. In addition, system components with permanent magnetic fields such as ion pumps were designed to be as far from the atom transport axis as possible.

A particular concern during the design and manufacture of the vacuum system was the presence of welds used to join sections of the chambers. Although the transport section of the vacuum system was made from non-magnetic 316L stainless steel, the process of melting the steel during welding results in a rearrangement of the magnetic domains in the metal which can cause an increase in its permanent magnetisation. This can result in stray magnetic fields in the vicinity of the welds which perturb the atoms during transport. In another experiment where this problem was encountered, it was necessary to slow the transport coils in the vicinity of the stray field to avoid atom heating and loss [106]. The presence of such stray fields was checked for in our apparatus by measuring the field inside the vacuum components using a gaussmeter before assembly of the system. These measurements showed that the stray fields were negligible compared to the strength of the trapping fields used to transport the atoms.

Chapter 5

Experimental Apparatus

5.1 Vacuum System

The vacuum system is composed of two chambers: the magneto-optical trap (MOT) chamber where rubidium atoms are initially captured from a room temperature vapour and cooled, and the science chamber, onto which is connected the glass, 'science' cell where the atoms are further cooled to quantum degeneracy. The science cell was custom-made by BFi Optiglass from 2 mm thick quartz and has inner dimensions 10×16 mm in the vertical and horizontal directions respectively and length 70 mm.

The cell height is smaller than that of previous cells used in the group to allow the magnetic coils to be placed as close to the atoms as possible. However, the height was kept large enough to ensure good enough clearance for the atom cloud to be transported into the cell and to ensure that the conductance of the cell was high enough to maintain good vacuum.

It is important to maintain a pressure differential between these two chambers

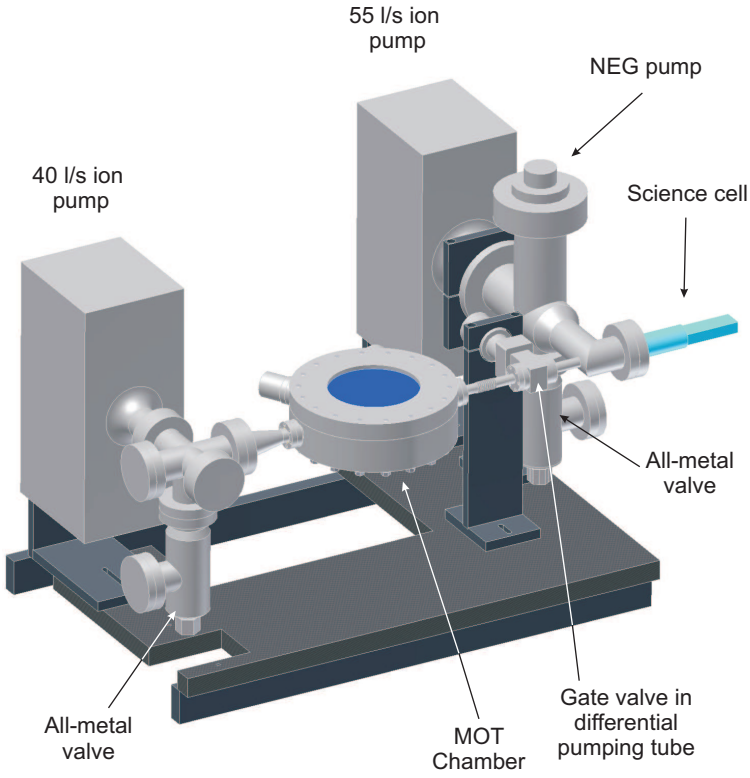

Figure 5.1: A diagram of the vacuum system

in order to separate the relatively high vapour pressure of the MOT from the science chamber where a pressure of approximately 10^{-11} Torr is needed to limit the collisions between trapped atoms and background gas molecules and give a sufficiently long trapped atom lifetime to allow BEC production. To this end, the two chambers are connected by a low conductance section of tubing: a 9 cm length of 1.2 cm inner diameter tube containing a hydro-formed bellows section, followed by a 3 cm length of 1 cm inner diameter tube. A gatevalve (Caburn, 302011) with internal diameter 1.6 cm is located between these two sections of the differential pumping tube to allow the two halves of the vacuum system to be sealed off from each other and baked out independently through one of the two all-metal valves shown in figure 5.1. The conductance of a circular tube, for air at 20°C, and very

low pressure so that the gas is in the molecular flow regime, is [107]:

$$C_{tube} = \frac{12.1 D_{tube}^3}{l_{tube}} \tag{5.1}$$

where D_{tube} is the tube diameter (cm) and l_{tube} is the tube length (cm). For the combination of tubes connecting the MOT and science chambers, $C_{tube} = 1.08\,\mathrm{l\,s^{-1}}$.

To maintain ultra-high vacuum the two chambers are continuously pumped by ion pumps: the MOT chamber by a $40\,\mathrm{l\,s^{-1}}$ pump (Varian, Vacion Plus 40 Starcell) and the science chamber by a $55\,\mathrm{l\,s^{-1}}$ pump (Varian, Vacion Plus 55 Starcell). A non-evaporable getter (NEG) pump (SAES, CapaciTorr-CF35, with C-400-2 DSK-St172 cartridge) is fitted inside the science chamber to provide additional pumping. The NEG pump was activated at the end of the initial vacuum bakeout and acts to adsorb rapidly gaseous species, principally hydrogen. It subsequently acts as an additional pump throughout the apparatus lifetime.

The low conductance between the chambers maintains the necessary pressure differential between the MOT and the science chamber. The lifetime of magnetically trapped atoms was measured to be $1.68 \pm 0.02\,\mathrm{s}$ in the MOT chamber and $109 \pm 12\,\mathrm{s}$ in the science chamber which are sufficient to allow the production of a MOT and BEC respectively.

The addition of a magnetic transport system to the apparatus imposes certain constraints on the design of the vacuum system. The section of the system between the MOT and the experimental cell must be suitably shallow to allow the moving transport coils to fit around the system whilst still giving a sufficiently large field gradient. To fulfil these criteria the maximum depth of this section of the vacuum system was made to be approximately 70 mm – equal to the diameter of the standard DN40CF flange which is used to join the science cell to the science chamber. To conform to this, the depth of the MOT chamber was made 74 mm.

The materials used in the transport section of the vacuum system must have a low magnetic permeability to give minimum field attenuation whilst possessing no permanent magnetisation which might distort the quadrupole field generated by the transport coils and lead to heating or loss of atoms. For this reason this section of the vacuum system was made from 316L stainless steel and the viewport on the MOT chamber was a custom-made non-magnetic viewport (manufactured by UKAEA).

The entire vacuum system is mounted on a breadboard fitted with rollers and can be moved along tracks on the optical bench. This allows the system to be moved out of the magnetic coil array during bakeout.

5.2 Lasers and Optics

5.2.1 Lasers

A key element in the experiment is the light used to laser cool the atoms in the MOT and then image the atoms in the experimental cell. The laser cooling scheme was introduced in subsection 2.2.4 and uses the $|F = 2\rangle \rightarrow |F' = 3\rangle$ transition in the $5^2S_{1/2} \rightarrow 5^2P_{3/2}$, (D2) line of ^{87}Rb, shown in figure 2.4. This transition is suited to laser cooling since it is a closed, cycling transition. As discussed in subsection 2.2.4, during laser cooling of the atoms in the $|F = 2\rangle \rightarrow |F' = 3\rangle$ cycle there is a small probability of off-resonant excitation to the $|F' = 2\rangle$ state from where the atoms can decay to the $|F = 1\rangle$ ground state. This process will eventually place all of the atoms into the $|F = 1\rangle$ dark state. To prevent this, the atoms are illuminated with a small amount of 'repumping' light, resonant with the $|F = 1\rangle \rightarrow |F' = 2\rangle$ transition, which pumps the atoms into the $|F' = 2\rangle$ state from where they can decay into the $|F = 2\rangle$ ground state and return to the cooling cycle. Imaging is

carried out using light resonant with the $|F = 2\rangle \rightarrow |F' = 3\rangle$ transition.

The need to excite transitions between hyperfine states in these processes places stringent constraints on the frequency and linewidth of the light. The frequency must be locked to the transition frequency and have a linewidth less than the natural width of the transition. Such narrow linewidths can only be achieved by using lasers and external cavity diode lasers (ECDL) are used in this experiment. ECDL have become the standard choice of laser in BEC experiments since they can provide suitably narrow linewidths over a wavelength range of several nanometres, whilst being compact, low maintenance, and relatively inexpensive.

The main lasers used in this experiment are Toptica DL100 ECDLs. These are used in the Littrow configuration in which the external cavity is formed between the back face of the laser diode and a diffraction grating. The first diffracted order from this grating is reflected back into the diode and the zeroth order forms the output of the laser. The diode is forced to lase at the narrow range of frequencies contained in the first order. This gives a typical linewidth of less than 1 MHz, which is sufficiently small for laser cooling. The laser frequency can be scanned over a range of $\sim$10 GHz by using a piezo actuator to adjust the grating angle.

The diode temperature and current are regulated using Toptica DTC110, and DCC110 units respectively. The piezo scan is controlled using a Toptica SC110 unit. A Toptica PID 110 unit is used to keep the lasers locked to the desired frequency in the cooling and repumping locking schemes outlined below. Finally, a Toptica PDD 110, Pound Drever Hall detector is used to provide the laser current frequency modulation, and generate the error signal used in the repumping locking scheme.

The lasers are locked to the required frequencies by locking to one of the lines in a reference set of hyperfine lines obtained through sub-Doppler laser spectroscopy

of rubidium. Several types of spectroscopy have been developed which are suitable for this purpose. In these experiments two types of spectroscopy are used: modulation transfer spectroscopy (MTS), and Doppler-free saturated absorption spectroscopy (SAS). The details of these locking schemes, and the optical setup employed, are outlined in the following sections. The hyperfine energy levels of rubidium used in cooling and imaging in the experiment are shown in figure 2.4.

The optical setup for the experiment is divided between two optical tables: the main table, shown in figure 5.2, houses the lasers used to generate the cooling and repumping light, and a slave laser which amplifies the cooling light; and a smaller table houses the tapered amplifier setup which is used to amplify the cooling and repumping light from the main table for use in the MOT.

5.2.2 Frequency Locking

Cooling Light

The light for laser cooling is obtained by locking an EDCL, the "Master" laser (containing an Eagleyard, EYP-RWE-0790-04000-0750-SOT01-0000 diode), to the $|\mathrm{F} = 2\rangle \rightarrow |\mathrm{F}' = 3\rangle$ transition using modulation transfer spectroscopy (MTS). MTS is a pump-probe type spectroscopy which relies on the non-linear interaction of light with rubidium atoms in a vapour cell to resolve the hyperfine structure of rubidium. The pump and probe beams are of roughly equal intensity and propagate through a rubidium vapour cell in opposite directions. The pump beam is modulated using an EOM driven at a frequency, $\nu_m = 10.15\,\mathrm{MHz}$. The transmitted light is phase-shifted such that it contains a carrier frequency, ν_c, with a series of sidebands separated by the modulation frequency, so that its electric field has the form:

$$E = E_0 \sin[\nu_c t + d_m \sin(\nu_m t)] \tag{5.2}$$

where E_0 is the electric field amplitude and d_m is the modulation index. For sufficient pump and probe intensities the non-linear interaction of the beams with the rubidium vapour results in a modulation appearing on the unmodulated probe beam.

The transfer of modulation to the probe beam proceeds through four-wave mixing of the different frequencies of the pump beam and its sidebands and the probe frequency, resulting in a series of sidebands on the probe beam. Further details of this process can be found in [108] and [109]. The modulation transfer to the probe beam only occurs when the laser frequency is very close to resonance with the hyperfine transition. The strongest modulation transfer occurs for closed transitions for which the four-wave mixing process underlying the transfer is most efficient. This is advantageous for us since a large error signal is obtained for the closed cooling transition, making laser locking to this transition straightforward.

The intensity of the probe beam is measured using a photodiode (Thorlabs, PDA36A). The probe sidebands induced through modulation transfer beat with the probe beam to give a signal on the photodiode which alternates at the modulation frequency, ν_m. This signal is zero except when the laser is tuned to the narrow range of frequencies around each hyperfine transition for which the sub-Doppler resonance condition is satisfied. At those frequencies peaks appear in the photodiode output.

An error signal for locking to the cooling transition is generated in the following way. First, the signal from the photodiode is amplified using a Minicircuits ZFL-500HLN amplifier. The relative phase of the resulting signal compared to the signal from the function generator used to drive the EOM (Photonics Technology, EOM01100013) is then found using a phase detector (Minicircuits, ZRPD-1). The output from this detector is passed through a low pass filter, with cut-off frequency

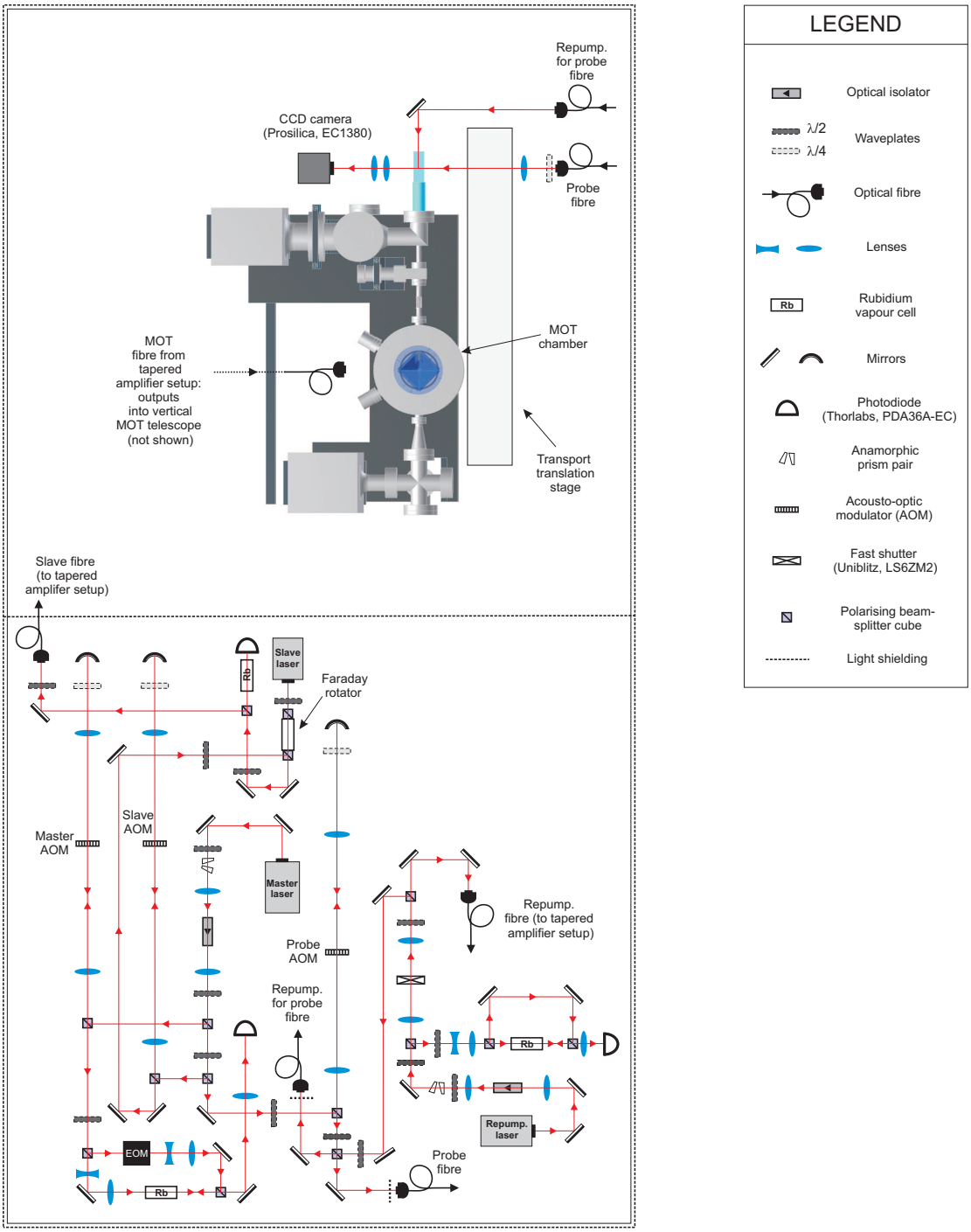

Figure 5.2: A diagram of the main optical table housing the Master, Repumping and Slave laser setups and the vacuum system.

1.9 MHz, to give a DC signal. This error signal is then passed to a PID controller (Toptica, PID 110) and the output applied to the piezo actuator in the laser to adjust the angle of the diffraction grating and keep the laser on resonance with the transition. A phase shifter (Minicircuits, JSPHS-12) is used to adjust the phase of the photodiode signal just before the phase detector to ensure that the error signal has a dispersive form. A higher frequency correction is also applied to the laser current to keep the laser on resonance.

A major advantage in MTS is that, at the transition frequency, the error signal amplitude is exactly zero. This is the case since, unlike in other sub-Doppler spectroscopy schemes in which Doppler broadening gives a non-zero background signal to the error signal, the error signal here resides on a flat, zero background. This characteristic along with the steep gradient of the error signal make it straightforward to lock electronically to the transition frequency. In addition, the zero signal at resonance means that the laser frequency is exactly that of the atomic resonance.

Light from the Master laser is split between three paths: the MTS setup, the imaging setup described below, and for injecting a slave laser. The slave laser is used to increase the total amount of cooling light to provide sufficient power to inject the tapered amplifier system described below. The slave laser was built in-house and contains a Sanyo DL-7140-201 diode which gives a maximum output power of 70 mW. The slave diode current and temperature are regulated using Clarendon-built controller units (EW1291 and EW1251 respectively). The output from the slave is fibre-coupled to the tapered amplifer table in a single-mode fibre (This fibre and all others used in the experiment are single-mode, polarisation-maintaining fibres from OZ optics).

Laser cooling requires light which is red-detuned relative to the $|\mathrm{F} = 2\rangle \rightarrow$

$|F' = 3\rangle$ transition. This detuning is achieved using a combination of the frequency shift provided by an AOM (Crystal Technology, 3110-140), the "Master" AOM, placed before the MTS setup and a second AOM (Crystal Technology, 3080-122), the "Slave" AOM which shifts the frequency of the Master light just before it is injected into the slave laser. For beam widths of 200 μm, the specified frequency shift for a single pass is approximately 110±14 MHz, and 80±15 MHz for the Master and Slave AOMs respectively. Master light is double-passed through the Master AOM with the first positive diffraction order transmitted to the MTS setup. This results in the Master laser being locked 220 ± 28 MHz below the cooling transition. Master light is then double-passed through the Slave AOM with the negative first diffraction order transmitted to the slave laser. The frequency of the light injecting the slave is thus $(160 \pm 30) - (220 \pm 28)$ MHz, following the AOM specifications. In practice, however, it was found that the range of single pass frequency shifts provided by the AOMs which still gave sufficient powers in the output beams was 105 to 145 MHz and 68 to 105 MHz for the Master and Slave AOMs respectively. This gives a detuning range of 0 to 77 MHz below the cooling transition which is sufficient for the MOT loading and compression.

Repumping Light

The repumping light is generated using saturated absorption spectroscopy (SAS) and frequency-modulation (FM) spectroscopy. In SAS a relatively weak probe beam propagates through a rubidium vapour cell and is incident on a photodiode. A relatively strong, counter-propagating pump beam, derived from the same laser as the probe beam, is made to overlap with the probe beam. For a particular laser frequency the two beams are each absorbed by a particular velocity class of atoms; those for which the radiation is Doppler-shifted onto resonance with an atomic

transition. For most laser frequencies the pump and probe beams are absorbed by different sets of atoms due to the fact that the beams are counter-propagating. The two beams are only absorbed by the same velocity class of atoms in two cases: when the laser frequency is on resonance with an atomic transition and when the laser frequency is exactly halfway between two atomic transitions. In these cases, the pump beam prevents a portion of atoms from absorbing probe light by both saturating their atomic transition(s) and hyperfine pumping them into dark states. The result, as the laser frequency is scanned, is a series of peaks in the probe beam intensity at the hyperfine transition frequencies and at frequencies exactly halfway between the hyperfine transitions ('crossover peaks').

The Repumping laser (containing a Sanyo DL-7140-201 diode) is locked to the $|\mathrm{F} = 1\rangle \rightarrow |\mathrm{F}' = 2\rangle$ peak in the SAS spectrum to give the required repumping frequency. Locking is achieved using a frequency-modulation (FM) scheme as follows. A modulation at $20 \pm 2\,\mathrm{MHz}$ is added to the laser current which results in a modulation of the laser frequency. This modulation is generated using a Toptica Pound-Drever-Hall detector (PDD 110). The phase of the resulting amplitude modulation in the intensity on the probe photodiode is compared with the phase of the modulation reference signal by the PDD 110 unit to produce an error signal whose magnitude represents the deviation of the laser frequency from the transition. The PID 110 controller uses this error signal to ascertain which side of the transition the laser frequency is on and to correct the frequency accordingly by adjusting the angle of the diffraction grating in the laser.

5.2.3 Tapered Amplifier

The total power provided by the Master and Repumping lasers is insufficient for operating the pyramid MOT, which requires a few hundred milliwatts of cooling

light and several milliwatts of repumping light. To obtain these powers a master oscillator power amplifier (MOPA) scheme is employed in which the repumping and slave light beams are amplified by the same tapered amplifier diode. A tapered amplifier diode is a semiconductor diode comprised of a tapered section of gain medium which is anti-reflection coated on both the input and output facets. The gain medium tapers outwards in one of the directions perpendicular to the axis of propagation of the injection beam – typically the horizontal direction – so that the area of the output facet is larger than that in a standard laser diode. This larger emission area gives a greater power in the output beam than that from a standard diode while the narrow part provides single-mode operation. In this experiment a 1 W tapered amplifer diode is used (Eagleyard, TPA-0780-01000-3006-CMT03-0000). The diode can amplify light over a maximum wavelength range of 780 ± 10 nm which makes it suitable for amplifying both the repumping and cooling light at the same time. The diode is specified to provide an amplification of 13 dB, and a maximum output power of 1 W.

The tapered amplifier and associated optics, shown in figure 5.3, are mounted on a separate table from the main laser and vacuum system table due to spatial constraints. The tapered amplifier diode is fixed in a Clarendon-built mount which is temperature regulated using two 20.9 W Peltier modules controlled by a Newport 350 temperature controller. The diode current is regulated using a Newport 560 current controller. The slave and repumping fibres carry approximately 30 and 15 mW of cooling and repumping light respectively to the tapered amplifer optical table. The powers of the beams injecting the diode are approximately 15 and 1 mW for the cooling and repumping light respectively. This repumping beam power was optimised to give the ratio of cooling to repumping light in the MOT which maximised the MOT atom number (see section 6.1). The total power in the

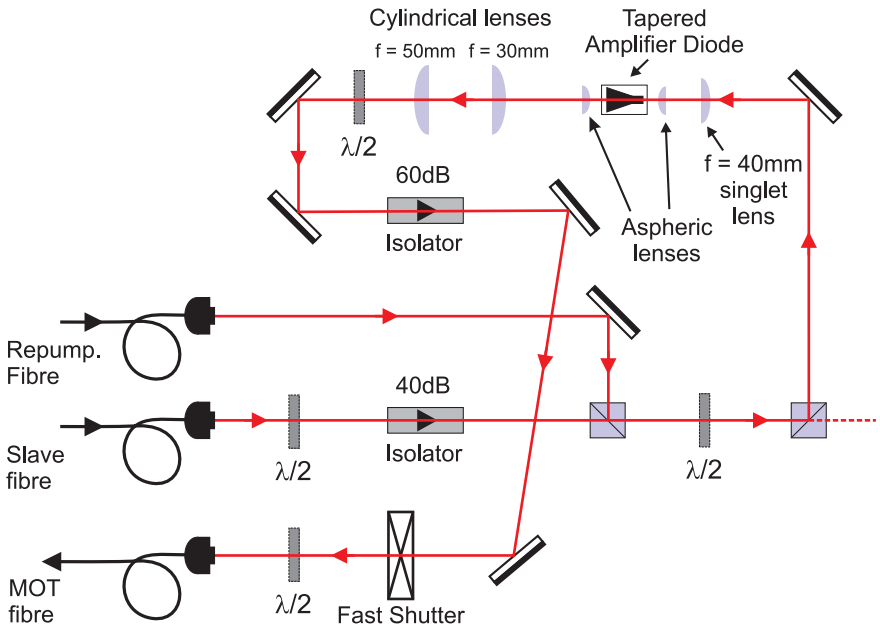

Figure 5.3: A diagram of the optical table containing the tapered amplifier setup. The repumping and slave fibres carry light from the main optical table to inject the tapered amplifier, and the MOT fibre carries the amplified repumping and cooling light to the pyramid MOT.

output beam just before the optical fibre is approximately 700 mW.

The angle of the injection beam into the diode is optimised by aligning the beam with the backwards-propagating spontaneous emission light from the diode. The aspheric lens located before the diode allows the injection beam to be focused onto the input facet of the diode. The position of this lens relative to the diode is adjusted using a fine-thread screw to achieve good coupling of the beam into the diode.

The output beam from the diode is strongly astigmatic and divergent. The divergence is much stronger in the vertical direction than in the horizontal direction as a result of the difference between the height and the width of the diode's output facet. For efficient coupling into a single-mode optical fibre the beam profile must be reshaped to be as symmetrical and as close to gaussian as possible. The output beam is collimated in the fast diverging vertical direction using the second aspheric

lens. A telescope of two cylindrical lenses allows the horizontal beam width to be adjusted independently of the vertical width. The telescope reduces the horizontal width of the output beam such that it is comparable with the vertical width. The collimated output beam is coupled into a single-mode optical fibre which carries the light to the MOT telescope described in section 5.3. A coupling efficiency into the fibre of ∼25% is achieved. The fibre spatially filters the irregular mode from the tapered amplifier light to give a regular gaussian mode at the output.

A fast shutter (Uniblitz, LS6ZM2), with minimum switching time ∼1 ms, is placed before the optical fibre to allow the MOT light to be rapidly blocked at the end of the MOT loading phase. A counterpart fast shutter (Uniblitz, LS6ZM2) in the repumping path on the main laser table blocks the repumping beam before the fibre which carries it to the tapered amplifier table. This allows the cooling and repumping light to be blocked independently. This is exploited at the end of the MOT loading cycle when the repumping light is blocked two milliseconds before the cooling light to 'pump' the atoms in the MOT into the $|\mathrm{F} = 1\rangle$ state (see subsection 6.1.1). A slower, Clarendon-built shutter is placed just before the fibre to the MOT telescope to block out any stray light.

5.2.4 Imaging Light

Two types of imaging are used in the experiment: absorption imaging and fluorescence imaging. The former uses light resonant with the $|\mathrm{F} = 2\rangle \rightarrow |\mathrm{F}' = 3\rangle$ transition, and the latter uses light slightly red-detuned from this transition. Since the atoms are magnetically trapped in the $|\mathrm{F} = 1, m_F = -1\rangle$ substate during the experiment, before imaging it is necessary to use some repumping light to pump the atoms into the $|\mathrm{F} = 2\rangle$ state. For this, approximately 1.5 mW of repumping light is fibre-coupled to the imaging setup described in section 5.8. The fast shut-

ter located in the repumping path allows pulses of repumping light of millisecond duration to be produced.

The $|F = 2\rangle \rightarrow |F' = 3\rangle$ resonant or near-resonant light for both imaging schemes is generated using a portion of the light from the Master laser. This light is double-passed through the Probe AOM (Crystal Technology, 3110-140) which has a specified frequency shift of 110 ± 14 MHz. The actual measured range of frequency shifts given by this AOM is 65 to 105 MHz. The first positive diffraction order is selected. The shift given by this AOM cancels the frequency shift given by the Master AOM to put the Master light onto resonance with the $|F = 2\rangle \rightarrow |F' = 3\rangle$ transition. Detuning from resonance, to create the light used in off-resonant absorption imaging or fluorescence imaging, can be achieved by either tuning the frequency shift given by the Probe AOM or that given by the Master AOM.

For absorption imaging the pulses of imaging light must be at most tens of microseconds in length which cannot be accomplished with the shutters used in the experiment. Instead, the Probe AOM is used as a fast shutter, and gives minimum pulse lengths of $\sim 10\mu$s. The imaging light is fibre-coupled to the imaging setup in a separate fibre to the repumping light.

5.3 Magneto-Optical Trap

The source of cold rubidium atoms in the apparatus is a pyramid magneto-optical trap (MOT), described in section 2.2. The specific design in this thesis, with a pyramid MOT used as the sole MOT, was based on a design from JILA [55]. The construction details were also based on previous pyramid MOT designs in our group [52–54].

An advantage of the pyramid MOT over the six-beam MOT is that the trapping beam geometry is fixed by the geometry of the pyramid and so, once the angle of

the input beam has been fixed, no beam re-alignment, or beam power-balancing is necessary. Since there is only one input beam, far fewer optics are required for beam collimation and control of polarisation, which gives greater clearance for the transport coils to move in around the MOT chamber. In addition, the pyramid is very power efficient since the beams are 'recycled' through the reflections. A disadvantage of the pyramid MOT, however, is that separate control of the trapping beam powers is not possible, and thus exact beam power-balancing is difficult to achieve. This means that true optical molasses, in which the magnetic field of the MOT is completely turned off, is difficult to achieve since the imbalance in beam powers would destroy the cloud during this stage. However, as described below in chapter 6, some degree of beam power-balancing can be achieved in the pyramid MOT which allows the magnetic field to be reduced to almost zero for a few milliseconds, and provides the additional MOT cooling and compression discussed in section 2.2.

The polarisation of the input beam and of the reflected beams in a pyramid MOT is shown in figure 2.3. For ideal MOT operation the circularly polarised input beam should be reflected to give circularly polarised light of the opposite handedness. For this, both the phase shift of the s- and p-polarisations upon reflection and the reflectivities for these polarisations should be approximately equal. Any difference in reflectivity of the mirror for s- and p-polarisations will result in an anomalous phase shift of light into the wrong handedness.

The anomalous phase shift incurred after a single reflection from a mirror is defined as θ, with:

$$\cos\theta = \frac{I_O - I_S}{I_O + I_S} \tag{5.3}$$

where I_S is the reflected light of the same handedness as the incident light and I_O is the reflected light of the opposite handedness to the incident light.

The MOT mirrors were designed to be as close as possible to 100% reflecting for s- and p-polarisation, and to give approximately equal phase shifts for these two polarisations, for reflection at an angle of 45°. The mirror blanks were made from 5 mm thick, $\lambda/20$ flatness BK7 glass (custom made by BFi Optiglass). These were coated by our in-house thin film facility with a dielectric coating comprising a 21 layer stack of alternating layers of SiO_2 and TiO_2. The coating was designed to give the required reflectivities for s- and p-polarisations for light with a wavelength in the range 760 nm to 790 nm, thus allowing the MOT to be used to trap rubidium (trapping wavelength 780 nm - as reported in this thesis) and, with potential future experiments in mind, potassium (trapping wavelength 767 nm). The anomalous phase shift of our mirrors was measured to be $< 5.4°$, which is sufficiently small to allow good MOT operation.

Previous pyramid MOTs in our group have used a similar dielectric mirror coating and have demonstrated consistent operation over years of use, with no degradation in the reflectivity of the mirrors or in the number of atoms trapped in the MOT. This should be contrasted with experiments using gold coatings which show considerable degradation in mirror reflectivity over time due to the build up of rubidium on the gold surface [55].

The pyramid was assembled by gluing the triangular glass substrates onto four separate prism-shaped mounts of 316L stainless steel using UHV epoxy (Epotek 353ND). The dielectric coating described above was applied subsequent to the gluing of the substrates to the mounts. The steel mounts were machined such that when fitted together the mirrors would form a pyramid with 90° angles between opposing faces. The base length of the pyramid mirrors is 65 mm.

Following the design in [55], a section was cut out of two adjacent mirrors to give a slot down the diagonal edge of the pyramid to allow atoms to be transported

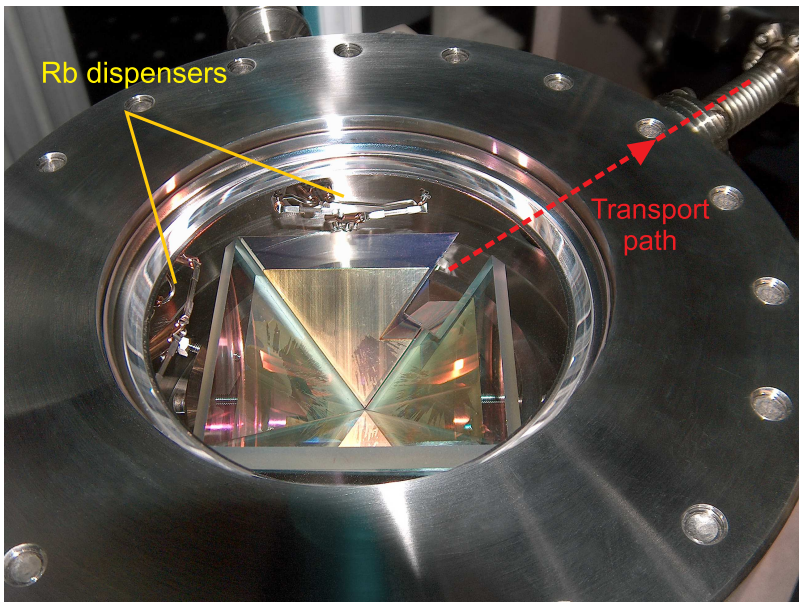

Figure 5.4: Photograph of the pyramid MOT chamber. Indicated on the figure are the two pairs of rubidium dispensers, and the path along which the atoms are moved out of the chamber during atom transport.

out of the MOT chamber during the transport sequence to the science chamber. The width of this slot is 1 cm and it extends 2.5 cm down the diagonal of the pyramid. The material excised to form the slot is at the edge of the two mirrors, and hence has a negligible impact on the MOT operation, merely removing the low power edge of the two reflected beams and reducing slightly the overall capture volume of the MOT, and thus the final atom number in the MOT.

The four separate blocks of the pyramid MOT are bolted together into one unit inside a retaining ring. This assembly is then fixed rigidly in place in the MOT chamber beneath a custom-made DN160CF non-magnetic viewport with window diameter 95 mm (manufactured by UKAEA). The large input beam to the MOT is formed using a telescope assembly positioned above the viewport, illustrated in figure 5.5. Light enters the telescope via a single-mode optical fibre which carries both repumping and cooling frequency light from the tapered amplifer setup. The total power in this beam is approximately 150 mW. The MOT telescope performs

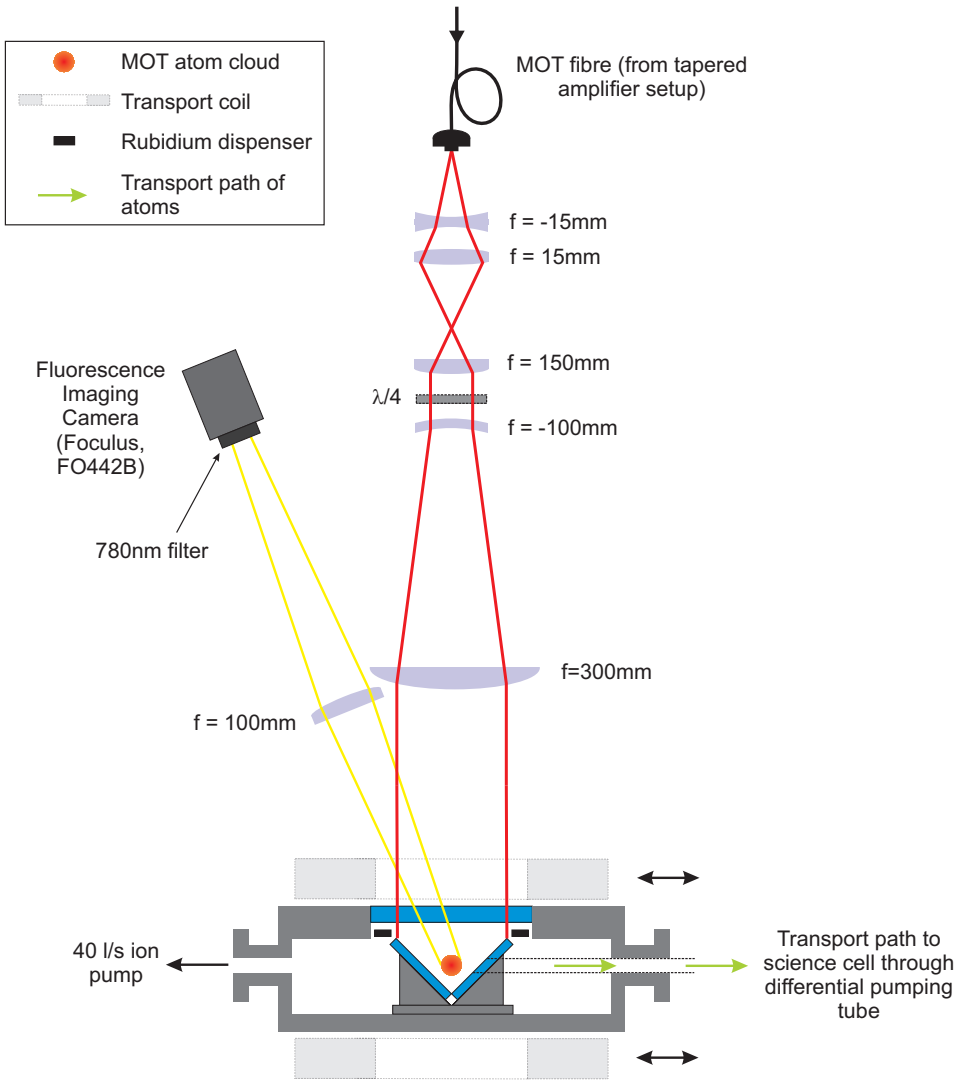

Figure 5.5: Cross-section diagram of the MOT telescope and MOT chamber.

two functions: it fixes the size of the beam entering the MOT and then collimates this beam. The first function is achieved by the first two lenses after the fibre. Adjusting the separation of these lenses and their distance from the fibre alters the diameter of the beam on the third lens. This adjustment was incorporated to allow empirical optimisation of the beam size entering the pyramid MOT since it was unknown what exact beam width would give the optimum MOT number for our particular size of pyramid. The maximum possible input beam size to the MOT is 80 mm (for the complete beam diameter), which is set by the internal diameter

of the Transport coils which are positioned concentrically above and below the MOT chamber during MOT operation. The Transport coils are used to generate the low field gradients required for MOT loading as well as the higher gradients used in magnetic trapping and transport. Details of these coils are given in the following section.

After this variable expansion the beam is further expanded by a fixed amount and then collimated using three lenses: an achromatic doublet lens, a meniscus lens and a large singlet lens. This system was designed to expand and collimate the beam in a way that minimises spherical aberration. A $\lambda/4$ waveplate, positioned between the doublet and meniscus lenses, transforms the linearly polarised light from the fibre into the circularly polarised light required for MOT operation. Also present in the telescope, just before the large collimating lens, is a small power pick-off which diverts a small portion of the light from the beam edge to an amplified photodiode (Thorlabs, PDA36A-EC) to allow the power coupled though the MOT optical fibre to be easily monitored.

The entire MOT telescope assembly is mounted on an xy-translation stage to allow the position of the MOT input beam to be adjusted relative to the pyramid assembly. This adjustment was employed when optimising the MOT loading and magnetic capture (see section 6.1).

The rubidium for the MOT is provided by two pairs of dispensers (SAES, Rb/NF/3.4/12 FT10+10) which are attached to two electrical feedthroughs on side ports of the MOT chamber. To activate the dispensers initially, a current of approximately 8 A was run through them for several seconds. The operating current during experiments is 3 A, and experience with previous setups has shown that the dispensers can run at this current for several years before their rubidium is depleted.

The number of atoms in the MOT is measured by imaging the fluorescence from the MOT cloud onto a CCD camera (Foculus, FO442B). The imaging is achieved using a single 100 mm focal length doublet lens arranged in a $2f-2f$ configuration such that there is no image magnification. A 780 nm filter is fitted to the camera to block out all light except that emitted by the MOT. A Labview VI is then used to sum the total CCD counts given by the MOT cloud for a given exposure time. This figure is converted into the total atom number in the cloud using the following formula [43]:

$$N_{MOT} = \frac{8\,\pi\,[1+4(\delta/\Gamma)^2+(C_1^2 6I_0/I_{sat})]\,N_{counts}}{C_2^2\Gamma(6I_0/I_{sat})\,t_{exp}\,\eta_{count}\,\mathrm{d}\Theta} \tag{5.4}$$

where δ is the frequency detuning of the cooling light from the atomic transition, Γ is the decay rate of the excited state, C_1 and C_2 are the average Clebsch-Gordon coefficients for the transitions between the different Zeeman sublevels in the ground and excited states; here both equal to 7/15, I_0 is the intensity of one of the six MOT beams, I_{sat} is the saturation intensity of the transition (equal to $1.67\,\mathrm{mW\,cm^{-2}}$ for the $|\mathrm{F}=2\rangle \rightarrow |\mathrm{F}'=3\rangle$ transition in ^{87}Rb), t_{exp} is the exposure time of the camera, η_{count} is the efficiency of the camera (number of counts per photon), $\mathrm{d}\Theta$ is the solid angle of the light collected by the camera, and N_{counts} is the integrated number of counts on the camera.

5.4 Moving Coils Transport System

5.4.1 Coils and Translation Stage

The same coils that are used to provide the quadrupole field for the MOT are also used to trap the MOT atom cloud and transport it out of the MOT chamber and

to the science cell. These moving coils, the "Transport" coils, consist of 15 by 8 turns of 1.8 mm by 3.6 mm enamelled copper wire, and have an inner diameter of 80 mm. The inner coil separation of 85 mm allows the coils and their mounts to pass freely over the vacuum system and trapping coil array to the science cell. The coils are fixed in aluminium mounts which act as a heat-sink for the heat dissipated during the approximately two second transport time. This maintains a reasonably low steady-state temperature without the need for water cooling. The coils are driven by a Xantrex, XFR 20-60 power supply which gives a maximum output of 20 V and 60 A.

The coils are mounted on a Parker 404XR translation stage which can be moved a maximum distance of 600 mm. The translation stage is moved by a ballscrew which is driven by a servo motor (Parker, SMB60 30 1,4 892VB64 0). Each revolution of the ballscrew moves the stage 20 mm. The motor is controlled using a drive unit (Parker, ViX 250ie) which can be programmed to give arbitrary movement profiles by varying the acceleration, deceleration, velocity, and start and end positions of the translation stage. Once a movement profile is uploaded to the drive it is triggered using a TTL input. The motor controls the position of the translation stage with a bi-directional reproducibility of $\pm 3\,\mu$m, and an absolute positional accuracy of 40μm. The total load of the Transport coils and their mounts on the translation stage is approximately 10 kg. The rated torque of the motor is 0.25 Nm which for this load gives a maximum acceleration of the stage of $8\,\mathrm{m\,s^{-2}}$. The maximum velocity of the stage is set by the maximum rated angular velocity of the ballscrew, and is equal to $1.1\,\mathrm{m\,s^{-1}}$ [110].

5.4.2 Discharge Circuit for the Transport Coils

The relatively high inductance, $L = 3\,\mathrm{mH}$ (per coil), of the Transport coils, with resistance, $R = 0.16\Omega$ (per coil), means that the current through the coils cannot be ramped up sufficiently quickly to give optimal atom loading using their power supply alone. For optimal loading the quadrupole gradient must be ramped from the $13.9\,\mathrm{G\,cm^{-1}}$ at the end of the MOT to $150\,\mathrm{G\,cm^{-1}}$ in approximately $2\,\mu\mathrm{s}$ or less. This corresponds to a change in coil current from 5.5 A to 60 A, which would take the power supply on the order of 100 ms.

In order to increase the rate of the current ramp the capacitor discharge circuit shown in figure 5.6 was installed in series with the power supply. The capacitor discharge is initiated by triggering the thyristor using a digital output. To give the required current ramp the following procedure is used. First, in the 50 ms prior to the start of the ramp the power supply is switched into constant voltage mode and a voltage of 16 V is maintained. The current passed through the coils is controlled by keeping the MOSFET (STMicrolectronics, STE180NE10) in figure 5.6 partially open. This stage is the compressed MOT stage outlined in subsection 6.1.1, during which the current through the coils is ramped down to almost zero. Keeping the voltage across the power supply high allows it to respond immediately at the start of the current ramp. At the end of the 50 ms stage the current ramp is initiated by simultaneously discharging the capacitor, switching the power supply to constant current mode and programming it to output 60 A, and fully opening the MOSFET. The capacitor discharge increases the voltage across the power supply which produces a ramp up of the current to 50 A in $1.5\,\mu\mathrm{s}$. The power supply then continues this ramp up to its maximum current of 60 A in a further 200 ms (see figure 6.4).

Following the current ramp the magnetic gradient is kept at $150\,\mathrm{G\,cm^{-1}}$ whilst

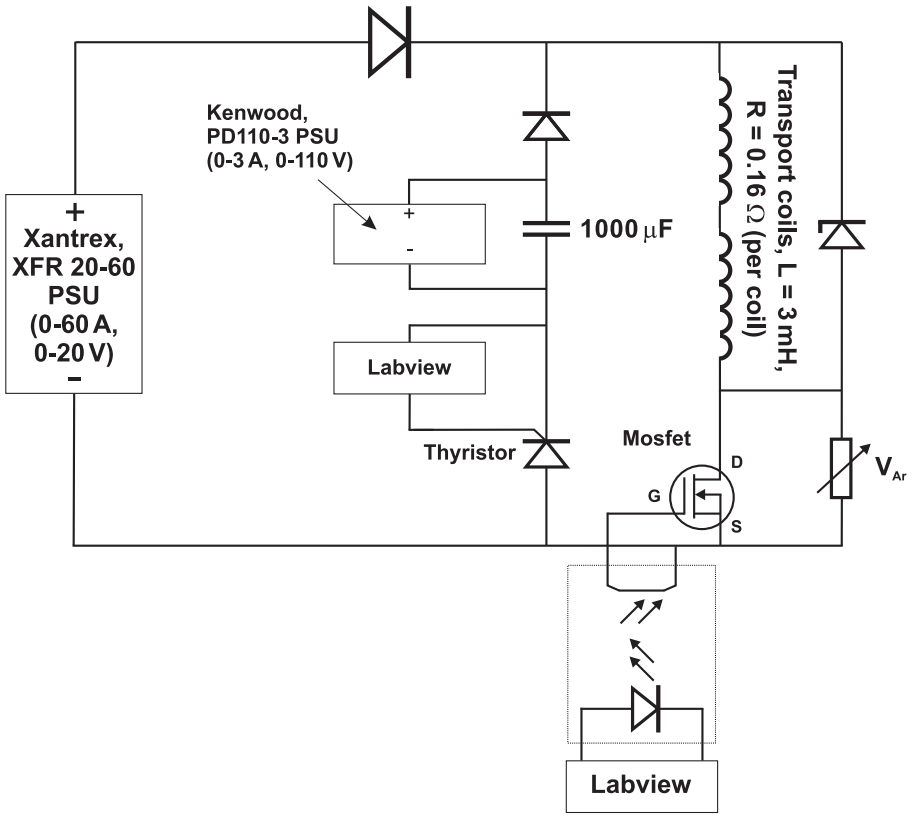

Figure 5.6: Circuit diagram of the capacitor discharge circuit used to produce a rapid current ramp through the Transport coils.

the Transport coils are moved from the MOT chamber to the science cell. This value for the gradient was based on the considerations discussed in section 4.3. The Transport coil power supply is run in constant current mode to ensure that the atoms are subjected to a constant field gradient throughout their transport. This gives a current regulation of: (current value $\pm 250\,\mathrm{mA}$) $\pm 0.1\%$. For the transport current of 60 A this corresponds to $\pm 0.31\,\mathrm{A}$.

5.4.3 Transverse Bias Field

An additional coil was added to the Transport coil mount to provide a bias field for moving the magnetically trapped atoms in the horizontal direction perpendicular to the transport axis during the transport sequence. This bias field was necessary

since without it a substantial fraction of the atoms were lost through collisions with the sides of the exit port of the MOT chamber at the start of the transport sequence (see subsection 6.2.1). The bias coil inner dimensions are 25×100 mm, and it is composed of 72 turns of 2 mm thick enamelled copper wire. It generates a bias field of 0.26 G per ampere at the centre of the Transport coils in the horizontal direction perpendicular to the axis of transport. This field shifts the minimum of the transport potential, and hence the position of the atom cloud, by approximately 0.033 mm per ampere.

5.5 Magnetic Transfer and Trapping Coils

The principal results presented in this thesis involve transport of the atoms in the moving transport coils alone all the way to the science cell. The optimisation of this transport process is presented in chapter 6. This forms the preliminary approach to atom transport outlined in section 4.3. The final, hybrid atom transport system involves combining this approach with the second overlapping coils approach to transport. In the full hybrid system the atoms are first transported in the moving Transport coils to within a few centimetres of the final magnetic trap position. The currents through several fixed magnetic coils, hereafter referred to as the "Transfer coils", are then controlled to create a moving potential which moves the atoms out of the Transport coil field and into the final magnetic trapping potential. So far, this full, hybrid transport system has only been used in preliminary tests (see section 6.2) to move the atoms from the transport potential to the final magnetic trap, and has not been optimised for use in experiments. Ultimately, the hybrid system will be employed when the proposed high resolution imaging system has been brought online. This section describes the Transfer coil assembly and the control electronics used to ramp and control the coil currents.

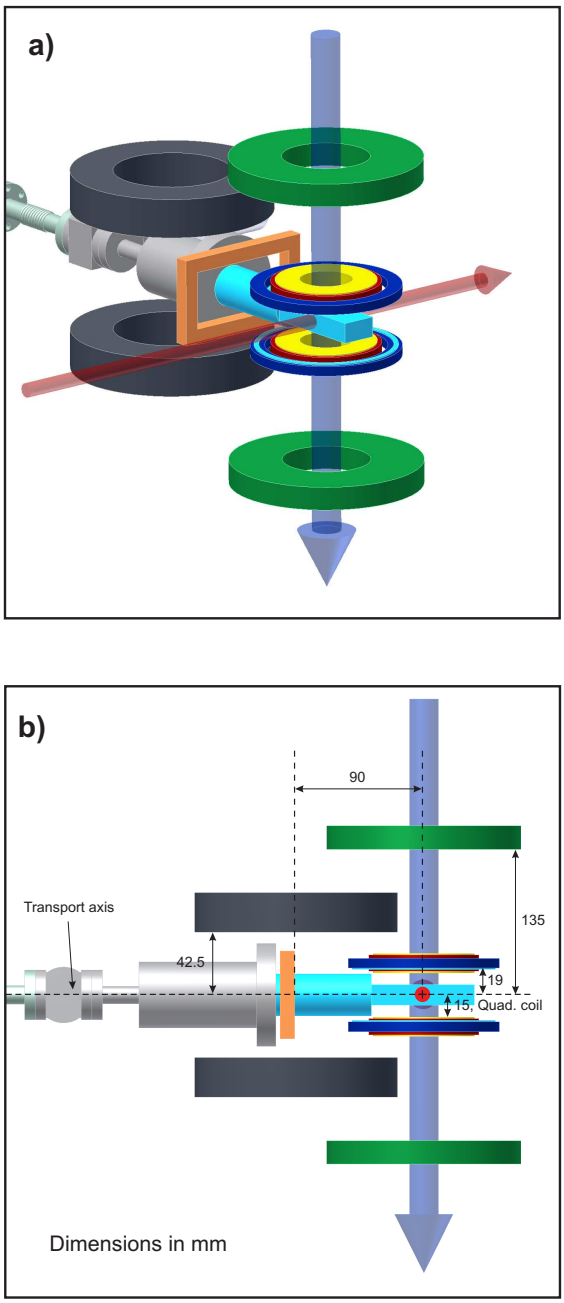

Figure 5.7: Diagram of the main trapping and transfer coils around the science cell: a) isometric and b) side view. The following coils are shown: Transport (black), Push (orange), Auxiliary (green), Helmholtz (dark blue), Quadrupole (yellow), z-RF (red) and z-TOP (light blue). The coil mounts are omitted for the sake of clarity. In (b) the Transport coils are pictured in their final position during the transfer sequence. The red and blue arrows indicate the horizontal and vertical imaging paths respectively.

The exact arrangement of coils, their separation and field gradient, was designed using a Matlab code in which the fields from arbitrarily shaped coils could be simulated. The criteria for minimising atom heating or loss during transfer were that any changes in the magnetic field gradient be adiabatic and that the aspect ratio of the trapping potential remain close to unity, as discussed in subsection 4.3.2. The arrangement of the coils is shown in figure 5.7.

The "Quadrupole" coils provide the field in which the atoms are initially trapped following moving coils transport. These coils also provide the quadrupole field for the TOP trap. In the first stage of the hybrid transport approach, the Transport coils are moved as close to the final Quadrupole coils as possible without impinging on the vertical imaging path. At this position the centre of the Transport coils is 9 cm from the centre of the Quadrupole coils, as shown in figure 5.7 (b). The atoms are transported the remaining distance to the final trapping site by ramping the current in the coils as follows:

1. Ramp up the current in the Push coil.

2. Ramp down the current in the Transport coils whilst simultaneously ramping up the current in the Auxiliary coils.

3. Ramp down the current in the Push coil.

4. Ramp down the Auxiliary coil current and ramp up the Quadrupole coil current.

At the end of this sequence the atoms reside in a quadrupole potential generated solely by the Quadrupole coils. The specifications of the coils used in this transfer sequence are given in table 5.1.

The transfer sequence and final magnetic trap require relatively large magnetic field gradients. To obtain such gradients the magnetic coils must be either very

close to the atoms or they must contain a large number of turns or a high current. The spatial constraints on the apparatus meant that the former two options were not possible and thus to achieve high gradients, large, $\sim 300\,\mathrm{A}$, currents were used. Such large currents result in substantial resistive heating and therefore the coils must be well cooled. To this end, the coils were constructed from copper tubing which is cooled by flowing water along the length of the coil. It is important that the water flow rate through the coils be large enough to remove the resistive heat and keep the coils at a reasonably low steady-state temperature. A maximum steady-state temperature of 50°C was chosen. To find a suitable bore of tube to allow this, typical flow rates were calculated using the Bernouilli equation for pressure drop along a pipe which takes into account the length of the coil and its bore.

The tubing used for the coils (Wolverine Tube Europe) is made from pure copper with a circular bore, and insulated on the outside with Kapton tape by S&W wire. The coils were wound onto formers using a lathe, with each turn being glued in place using Araldite 2011 epoxy. To obtain the required water flow rates the longer Auxiliary coils were made from $4\times4\,\mathrm{mm}$ tube with a 2.5 mm diameter bore, whilst the other coils were all made from $3.3\times3.3\,\mathrm{mm}$ tube with a 1.8 mm diameter bore. The cooling water enters the coils at a pressure of approximately $4 \times 10^5\,\mathrm{Pa}$.

5.5.1 Vertical Bias Coils

Due to the relatively short working distance of the planned high resolution vertical imaging objective (2.8 mm to 3.6 mm), when this imaging system is used the atoms will have to be moved from the centre of the science cell, where evaporative cooling to BEC is carried out, downwards 5 mm to the surface of the cell before imaging.

	Inner diameter (mm)	**Separation (mm)**	**Turns (horiz. × vert.)**	**Gradient per amp. (G/cm/A) (simulated)**	**Error in gradient, % (measured)**	**Power Dissipation per coil (W) (with 330 A)**
Push	40 vertical 80 horizontal	-	3×3	-	-	865
Auxiliary	60	170	9×4	0.332	-15.2	1950
Helmholtz	83	43.2	3×2	-	-10.6	580
Quadrupole	36	30	5×4	2.45	-3.0	995
Transport	80	85	15×8	2.53	0.3	505

Table 5.1: Specifications of the high current, watercooled trapping and bias coils.

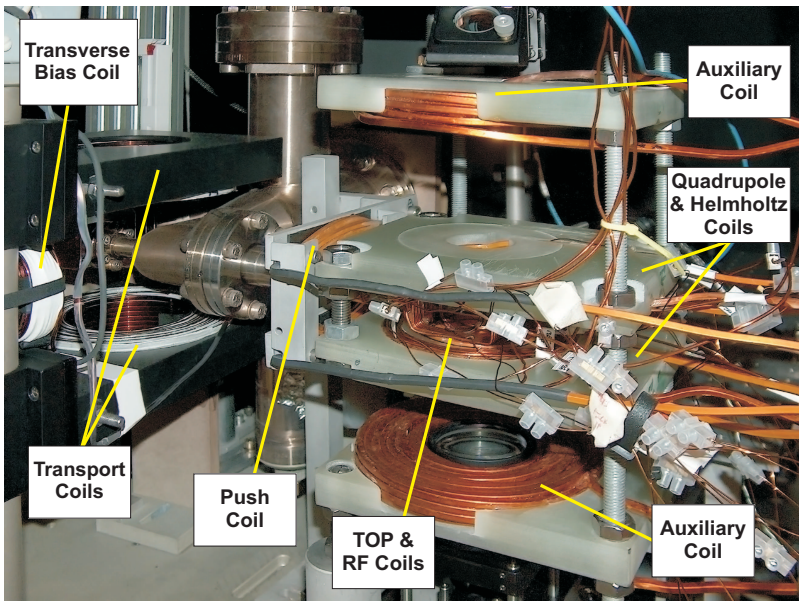

Figure 5.8: Photograph showing the main trapping and transfer coils around the science cell, and the Transport coils.

This will be achieved using a bias field to shift the net magnetic potential minimum. The bias field is principally generated by the "Helmholtz coils", which are arranged in approximately Helmholtz configuration (in a true Helmholtz configuration the coil separation is equal to the coil radius, in this case the separation is 0.87×radius).

The number of turns and separation of the Quadrupole and Helmholtz coils were designed using the aforementioned Matlab program to give the required field gradient and strength when run at a current of 330 A. The Quadrupole coils were designed to give an approximately $1000\,\mathrm{G\,cm^{-1}}$ axial field gradient for a current of 330 A. The Helmholtz coils were designed such that for a 330 A current they would almost exactly cancel out the field from the Quadrupole coils and bias the quadrupole field zero 5 mm from the centre of the cell to the surface of the cell.

The fields given by each coil pair differ from those calculated because of unavoidable errors incurred during the coil winding process. The deviation of the field strength from the ideal simulated values for each coil is given in table 5.1. These errors mean that the bias field given by the Helmholtz coils at 330 A will

not be of the exact magnitude required to move the field zero to the surface of the cell. This was allowed for in the design by making it possible for the Auxiliary coils to be switched from anti-Helmholtz to Helmholtz configuration and then used as secondary Helmholtz coils to fine tune the final biased position of the magnetic field zero.

The Auxiliary, Quadrupole and Helmholtz coil pairs are mounted above and below the science cell in Tufnol 10G/40 mounts. This material provides good rigidity and a low coefficient of thermal expansion to ensure minimal movement of the coils during the experiment, and thus minimal displacement of the resultant fields.

5.5.2 High Current Control Circuit

The water-cooled coils are all powered by a common supply (Magna-Power Electronics, SQA50-330) with a maximum output voltage of 50 V and a maximum current of 330 A, giving a total power output of 16.6 kW. All of the water-cooled coils are connected in series with the power supply. This allows the power supply to be run in constant current mode in which the current output is regulated through internal feedback. In this mode the power supply current is stable to within $\pm 0.04\,\%$ which is suitably small to avoid heating of the atoms through changes in the trapping potential.

During the experiment the fields from the various water-cooled coils must be ramped independently and with fine current control and stability to give adiabatic changes in the resultant fields. To achieve this, the servo circuit shown in figure 5.9 is used to control the current passing through the various coils.

The circuit is composed of blocks connected in series. In each block the coil pair (or single coil in the case of the Push coil) is connected in series with one MOSFET

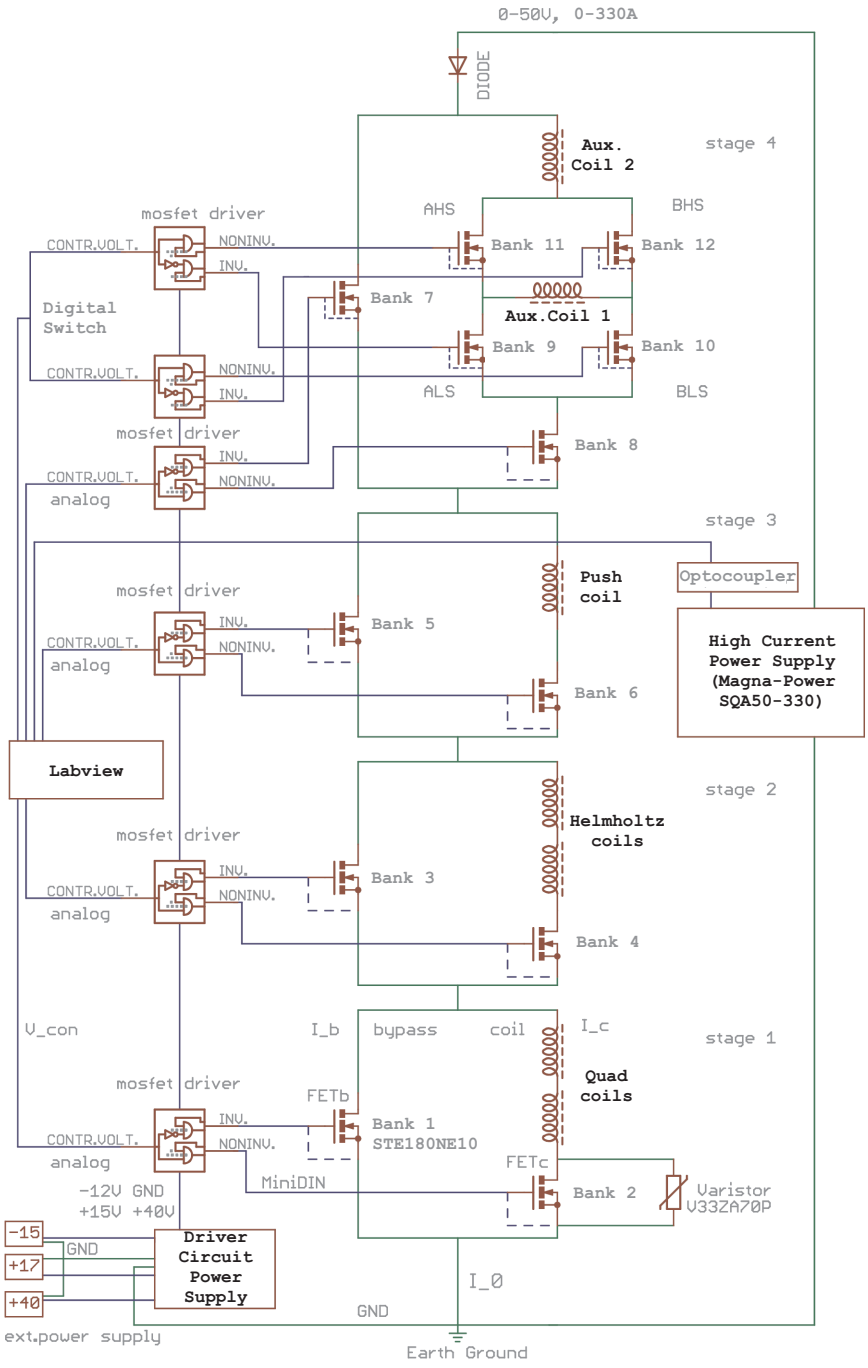

Figure 5.9: Circuit diagram of the high current control circuit used to regulate the current through the water-cooled coils. This circuit was designed and built by Gerhard Zürn [111].

bank and in parallel with another MOSFET bank. An analogue output voltage from the computer control system is used to set the gate voltage of the MOSFET banks. This control voltage is first passed through a MOSFET driver circuit which passes an inverted signal to the MOSFET bank in parallel with the coils and a non-inverted signal to the MOSFET bank in series with the coils. In this way the current through each block of the circuit can be diverted between the coil pair branch and the parallel bypass branch. The current passing through the coil pair can be ramped arbitrarily by ramping the control voltage into the MOSFET driver circuit. The circuit block containing the Auxiliary coils is arranged in an H-bridge formation with four MOSFET banks which allow the coils to be switched from anti-Helmholtz configuration to Helmholtz configuration for the stage when they are used as secondary Helmholtz coils to shift the atoms to the surface of the cell.

The MOSFETs (STMicrolectronics, STE180NE10) have a maximum drain current of 180 A (119 A) at a temperature of 25° C (100° C), and a maximum power dissipation of 360 W at 25° C. Since the MOSFETs are required to switch currents of up to 330 A, five such MOSFETs are used in parallel in each bank shown in 5.9. Such a large 'safety margin' was felt necessary because the MOSFETs do not all have the same characteristics and so do not carry the same load during turn on.

5.6 TOP Trap

The rotating bias field used to create the TOP trap is generated by two orthogonal pairs of 4.6 by 2.4 cm inner diameter rectangular Helmholtz coils. The coils are wound from 7 turns of 1.5 mm thick enamelled copper wire, and are glued together with the RF trapping coils into an array which fits around the science cell (see figure 5.10). The two TOP coil pairs are orthogonal to each other, with one producing the oscillating bias field in the x-direction and the other the field in the y-direction

(according to equation (2.29)). The TOP coils are in contact with the water-cooled Quadrupole coils which act as the necessary heat-sink for the heat generated by the TOP and RF trapping coils.

In addition, a pair of z-TOP Helmholtz coils is fixed onto the inside faces of the Helmholtz coils. These coils are used to provide a TOP field in the axial direction used in the generation of the TAAP trap discussed in section 3.8 and for tilting of the TOP trap. The z-TOP coils are 5 turn, 8.6 cm diameter, flat spiral coils made from 1.5 mm thick enamelled copper with 3.4 cm separation. Contact with the water-cooled Helmholtz coils provides cooling for the coils.

The 7 kHz TOP signal is generated using an Agilent 33220A function generator. This gives the sinusoidal component of the rotating bias field in equation 2.28. The cosinusoidal component is generated by phase shifting this sinusoidal signal. These two signals are then amplified by separate voltage-controlled amplifiers, such that the eccentricity of the trap may be adjusted. The signals are then amplified by a Crown XLS 5000 amplifier. This amplifier will produce a maximum output of 1500 W for a 4 Ω load. At 7 kHz, the TOP coils have an impedance of 0.42 Ω and in order to impedance match the coils to the amplifier a step-up transformer with a turns ratio of $81/26 = 3.1$ is used. The maximum current which may be run through the TOP coils is approximately 100 A peak-to-peak which corresponds to a TOP field magnitude, $B_T = 43$ G.

The signal for the z-TOP coils is the same cosinusoidal signal used for the x- and y-TOP coils. This is then passed through a voltage-controlled oscillator before being amplified by a Soundmaster VF250 amplifier. The coils are in series with a 29.2 μF capacitor and a 0.5 Ω resistor to create a circuit resonant at the required 7 kHz. All of the phase shifter and voltage-controlled electronics for the TOP trap were built in-house.

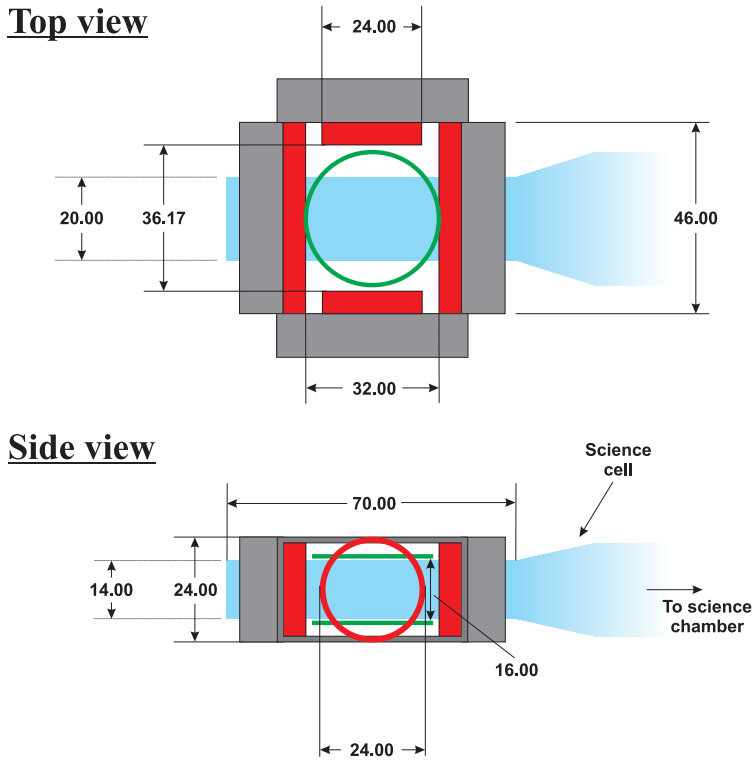

Figure 5.10: Diagram showing the arrangement of the TOP (grey), RF dressing (red), and evaporative RF (green) coils around the science cell.

In the initial optimisation of the atom transport sequence, presented in section 6.2, a different amplifier (Krell, 300cx) was used to amplify the TOP signals. After this amplifier developed a hardware fault it was replaced with the Crown amplifier which was used for all subsequent measurements: those presented in Chapter 7. This hardware change resulted in a small change to the TOP and Quadrupole fields in the experimental sequence, and caused a minor alteration to several parameters in the transport sequence compared to those in the initial optimisation (see section 6.2 for details).

5.7 Radio-Frequency Coils

5.7.1 RF Trapping Coils

The RF trapping fields are generated by two orthogonal pairs of Helmholtz coils wound from 1 mm thick enamelled copper wire. One of the pairs consists of 4.6 by 2.4 cm, 27 turn rectangular coils and the other of 2.4 cm outer diameter, 27 turn circular coils. Both pairs are wound from 0.5 mm diameter enamelled copper wire. The difference in geometry between the coil pairs was incorporated to stop the coil pairs overlapping and thereby reduce the inductive and capacitive coupling between the two channels. As with the TOP coils, the coil pairs are orthogonal to each other, with one producing the oscillating bias field in the x-direction and the other the field in the y-direction.

The signal for the RF coils is generated by a function generator (Stanford Research Systems, DS-345) and amplified by an RF amplifier (Minicircuits, ZHL-32A). The coils were designed to operate with several different frequencies of RF. To make this possible several different sizes of capacitor can be switched into the resonant circuit containing the coils. The standard RF frequency is 1.4 MHz.

In addition to these radial RF trapping coils, a pair of z-RF coils are wound onto the outside of the main Quadrupole coils to provide RF fields in the z-direction and enable tilting of the RF-dressed potentials (see figure 5.7). The coils are 7.0 cm in diameter and are separated by 3.8 cm. They are wound from 10 turns of 0.75 mm diameter copper wire.

5.7.2 Evaporative RF Coils

The RF radiation used in the evaporative cooling stage is generated using a pair of 3.2 cm diameter, 2 turn Helmholtz coils, made from 1 mm thick enamelled copper

wire. The coils are placed above and below the experimental cell at a distance of approximately 0.8 cm from the cell centre. The RF signal is generated using a custom-made direct digital synthesiser (DDS) unit. This unit was made for a previous experiment and full details may be found in [112]. The unit comprises a DDS chip (Analog Devices, AD9852) mounted on an Analog Devices evaluation board. A separate module contains a 60 MHz reference clock. The DDS chip can operate at up to 300 million samples per second and has 12 bits of amplitude resolution and 48 bits of frequency resolution. The output from the DDS module is passed through an RF amplifer (Minicircuits, ZHL-1-2W) before being passed through the coils. The RF evaporation ramps are first calculated in Labview before being passed in real time to the DDS module during the evaporation sequence.

5.8 Imaging System

All of the information about the atoms obtained in the experiment is acquired by imaging the atom cloud. In the experiments in this thesis absorption imaging was used to image the atoms in the science cell. The following sections outline the absorption imaging scheme and the methods used to fit to the images to extract information about the atom cloud. The proposed high resolution fluorescence imaging system is then discussed.

5.8.1 Absorption Imaging

In absorption imaging a pulse of probe laser light generated in the setup described in section 5.2 is passed through the cloud and the shadow cast by the atoms is imaged onto a CCD camera. Typically, the density of the atom cloud is too high to allow in-trap imaging and so prior to imaging the cloud is allowed to undergo a

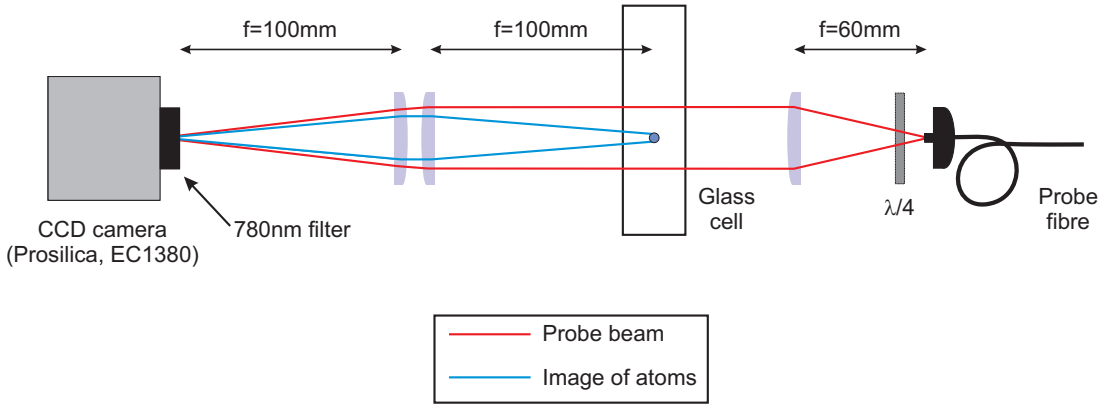

Figure 5.11: Diagram of the horizontal absorption imaging system used to image the atoms in the science cell. The typical probe beam intensity was $\sim 2\,\mathrm{mW\,cm^{-2}}$.

period of ballistic expansion to reduce its optical density. The total atom number in the cloud may be calculated from the attenuation of the light beam, and by fitting widths to the absorption image of the expanded cloud further properties such as the cloud temperature and phase space density may be deduced.

Figure 5.11 shows the optical setup for absorption imaging, in which the beam path is in the horizontal direction (illustrated in figure 5.7). The probe beam is passed to this setup from the laser side of the main table in a polarisation-maintaining fibre. The beam diverges out of the fibre and passes through a $\lambda/4$ waveplate to give circularly polarised light for imaging. The beam is then collimated by a 60 mm focal length doublet lens before passing through the science cell. The $1/e^2$ diameter of the collimated beam was measured to be 6.33 ± 0.02 mm. The typical probe beam intensity was $\sim 2\,\mathrm{mW\,cm^{-2}}$.

The magnification of the system is set by the ratio of the focal lengths of the pair of lenses in front of the camera. For the experiments in this thesis two $f = 100$ mm lenses were used to give approximately $1\times$ magnification. The exact magnification was found by measuring the distance fallen by an atom cloud for different times of flight and fitting these points with a parabolic function. This gave a value for

the magnification, $M = 0.97 \pm 0.01$. The image of the atoms can be focused either by adjusting the position of the final lens before the camera or the position of the camera itself.

To generate the final absorption image a series of three separate images is taken by the CCD camera (Prosilica, EC1380): first an image of the probe beam with the atoms present, second an image of the probe beam alone, and third an image with no probe beam, to measure the dark count of the CCD array. The relationship between the counts, C_{pix}, recorded by each camera pixel and the intensity of light incident on the pixel, I_{pix}, is given by:

$$I_{pix} = \frac{C_{pix}\,\hbar\omega}{\alpha_{pix} A_{pix}} \tag{5.5}$$

where ω is the angular frequency of the probe light, α_{pix} is the quantum efficiency of each pixel, and A_{pix} is the pixel area. For our camera α_{pix} and A_{pix} are $\sim 15\%$ and $6.45 \times 6.45\,\mu\mathrm{m}^2$ respectively.

The number of atoms in the cloud may be found by first noting that the attenuation of light by an optically thin medium is given by Beer's law:

$$I = I' e^{-\int n(y)\sigma_{abs}\mathrm{d}y} \tag{5.6}$$

where I is the transmitted intensity, I' is the initial intensity, $n(y)$ is the density of the medium along the imaging path, and σ_{abs} is the absorption coefficient of the medium. The probe beam excites the atoms to cycle between two energy levels and thus σ_{abs} is given by the two-level scattering equation:

$$\sigma_{abs} = \frac{\hbar\omega}{I'}\frac{\Gamma}{2}\frac{2(I'/I_{sat})}{1 + 2(I'/I_{sat}) + 4\delta^2/\Gamma^2} \tag{5.7}$$

where $\delta = \omega - \omega_0$ is the frequency detuning of the probe beam from the imaging transition.

By rearranging equation 5.6 the total atom number present in the optical path before the ith pixel can be found:

$$N_i = \frac{A_{pix}}{\sigma_{abs} M^2} \ln\left(\frac{I'}{I}\right) \tag{5.8}$$

where M is the magnification of the imaging system. The ratio of intensities in this equation may be expressed in terms of the per pixel intensities for the three images taken by the camera:

$$\frac{I'}{I} = \frac{I_{i2} - I_{i3}}{I_{i1} - I_{i3}} \tag{5.9}$$

where I_{i1}, I_{i2} and I_{i3} is the intensity at the ith pixel for the first, second and third images respectively. The total atom number is then found by summing over all pixels:

$$N = \sum_i N_i. \tag{5.10}$$

5.8.2 Image Fitting

Further properties of the cloud are calculated from the atom number and from the widths of the cloud image. The time-of-flight cloud widths are found by making 2D fits to the final absorption image described above.

The in-trap density distribution of a thermal cloud is gaussian, and is integrated along the imaging direction (y-direction) to give a 2D distribution of the form:

$$n_{2D}^{th}(x,z) = n_{2Dpeak}^{th} \exp\left(-\frac{x^2}{\sigma_x^2} - \frac{z^2}{\sigma_z^2}\right) \tag{5.11}$$

where n_{2Dpeak}^{th} is the peak density in the integrated distribution and σ_x and σ_z

are the cloud widths. For a condensate, taking the Thomas-Fermi approximation outlined in subsection 2.4.4, the in-trap density distribution is parabolic, so that the form after integration along the imaging direction (y-direction) is:

$$n_{2D}^{C}(x,z) = n_{2D\,peak}^{C}\left(1 - \frac{x^2}{R_x^2} - \frac{z^2}{R_z^2}\right)^{\frac{3}{2}} \tag{5.12}$$

where $n_{2D\,peak}^{C}$ is the peak density in the integrated distribution and R_x and R_z are the Thomas-Fermi radii.

In time-of-flight the thermal cloud density distribution remains gaussian, and the width in the i-direction rescales according to:

$${\sigma_i}^2 = \frac{k_B T}{m}\left(\frac{1}{\omega_i^2} + t^2\right). \tag{5.13}$$

Thus the temperature of the thermal cloud can be measured by fitting to the expanded cloud width. This temperature can then be used together with the measured cloud density to calculate other important quantities such as the phase space density and the elastic collision rate.

In the case of a condensate, in time-of-flight, the density distribution remains parabolic but the condensate aspect ratio inverts according to the scaling relations formulated in [113]. This expansion is brought about by the conversion of the interaction energy of the in-trap condensate into kinetic energy upon release from the trap. The characteristic anisotropic nature of the expansion versus the isotropic expansion of a thermal cloud serves as a key signature of Bose-Einstein condensation.

5.8.3 Proposed High Resolution Imaging System

The principal motivation behind building a new BEC apparatus was to make it possible to perform high resolution imaging of ultracold atoms. The key parameter which sets the resolution of any imaging system is the lowest value of numerical aperture (N.A.) in that system. Typically, the optical component with the lowest N.A. is the first lens which captures the light from the object. In the vertical imaging system in the old apparatus the imaging objective had an N.A. of 0.1 which set the resolution limit of the system to 4 μm [21]. The intention in the new apparatus is to increase the imaging resolution so that the resolution limit is one micron or better so that single atoms may be resolved. With this in mind two main solutions were considered: a custom objective lens and a commercial objective lens. We decided on the latter option since commercial microscope objectives are now readily available with values of N.A. up to 0.9, and are relatively inexpensive compared to custom options. The new experiment was designed around the inclusion of a Nikon objective (MRH08430-CFI Super Plan. Fluor. ELWD 40XC). This objective was chosen since it has a working distance of 2.8 to 3.6 mm which is compatible with the 2 mm thickness of the walls of the science cell. It has an N.A. of 0.6, which gives a diffraction-limited lower limit to the resolution of one wavelength, $\lambda = 780\,\text{nm}$.

The microscope objective must be placed immediately next to the cell wall, because of its short working distance, and the magnetic coils and optical paths were designed to allow for this. Specifically, as outlined at the beginning of this chapter, the location of the main MOT in the experiment was spatially separated from the science cell by incorporating the stage of magnetic transport. In addition, the inner diameter of the Quadrupole coils was made large enough to allow the objective to sit inside the bottom coil in this pair such that the collection lens could

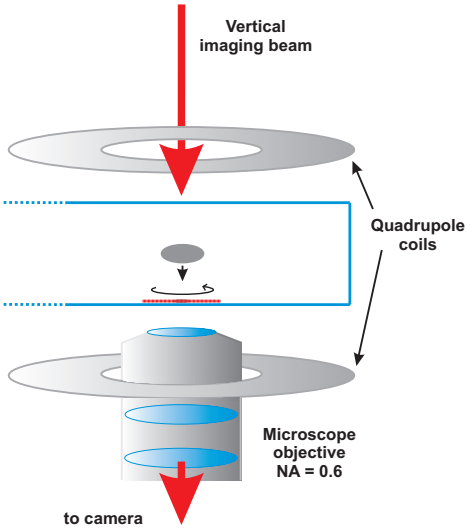

Figure 5.12: Diagram of the proposed high resolution imaging system and its experimental implementation. The atoms are first cooled at the centre of the cell by evaporative cooling. They are then biased toward the cell surface where the rapid rotation experiment is carried out. A deep, red-detuned 2D lattice is then ramped up to trap the atoms during fluorescence imaging.

be placed immediately next to the surface of the cell. The planned procedure for high resolution imaging, illustrated in figure 5.12, is the following:

1. Evaporatively cool atoms in the centre of the cell, as in the usual experimental sequence.

2. Using the fields from the Helmholtz and Auxiliary coils bias the atoms downwards to lie near to the bottom surface of the cell.

3. Turn on the RF shell trap to confine the atoms in a quasi-2D potential and perform the fast rotation experiment.

4. Ramp up a deep, red-detuned infrared 2D lattice to trap the atoms and induce fluorescence.

5. Image the atoms in the lattice by fluorescence imaging.

5.9 Computer Control

The many parameters which must be controlled during the experimental sequence and the microsecond accuracy that is required in the timing of this sequence mean that computer control is essential. In this experiment a field-programmable gate array (FPGA) module (National Instruments, NI PCI-7813R 3M digital R series) is configured with the experimental ramps and handles the necessary digital and analogue input and outputs during the experimental sequence. This module accommodates up to 160 digital channels which can be configured as either inputs or outputs with a maximum rate of 40 MHz. The FPGA module is connected to the control PC through a PCI card (NI PCI-7813R). The experimental control sequence is written in Labview and passed to the FPGA module before each experimental run. Separate National Instruments modules are used to produce the digital and analogue outputs and handle inputs. Analogue outputs are provided by five 4-channel, 16 bit modules (NI 9263), giving a total of twenty possible analogue outputs. Analogue inputs are received by a 32-channel, 250 KS/s module (NI 9205). A 32-channel module (NI 9403) can be configured for either digital inputs or outputs. A final, 4-channel module (NI 9211) receives inputs from thermocouples, used to monitor the temperature of e.g. the magnetic coils in the experiment.

Chapter 6

MOT and Atom Transport Optimisation

6.1 MOT Optimisation

The parameters of the MOT were optimised to give the largest atom number and an atom cloud with the highest phase space density when loaded into the magnetic trap. As outlined in subsection 2.2.2, the atom number in a MOT scales as d^4, where d is the linear size of the capture region which is set by the MOT laser beam width. In a pyramid MOT the width of the MOT beams is fixed by the dimensions of the MOT mirrors. In our case, this limits the (full-width) diameter of the MOT beams to approximately 3 cm.

The size of the input beam to the MOT was adjusted using the MOT telescope to make the full beam width approximately the same width as the base of the pyramid to ensure that all of the light was incident on the pyramid mirrors. This resulted in a $1/e^2$ diameter of 4.2 cm for the MOT input beam.

To give a cloud with the best possible phase space density in the magnetic trap, the uniformity and density of the MOT cloud must be maximised. The shape of the MOT cloud is determined by the net light and magnetic forces on the atoms. A uniform cloud of optimum density will be achieved when the powers of the six trapping beams are balanced and any stray magnetic fields have been cancelled out. Stray magnetic fields in the vicinity of the MOT were cancelled out using three magnetic coils – one for each spatial axis – positioned around the MOT chamber.

The balance in power between counter-propagating MOT beams is set by two factors: first, the respective reflectivity of the two opposing mirrors which produce the beams, and second, by the intensity of the portion of the input beam which forms each of the beams. The reflectivities of the MOT mirrors were measured before installation and are all $94 \pm 1\%$, therefore the first factor should have little impact on the MOT cloud. The second factor, however, was found to be more significant. The position of the MOT input beam relative to the centre of the pyramid fixes the intensity of each of the reflected MOT beams. Some power balancing between these beams can be achieved through fine adjustment of the input beam position. This is achieved by moving the entire MOT telescope assembly which is mounted on an xy-translation stage.

Unfortunately, the final pyramid MOT assembly contained a slight flaw due to errors incurred during the gluing of the mirrors to their support blocks. Small gaps were present along the lines where the four individual mirrors meet at the pyramid vertices. Directly above these gaps there is no retro-reflected light and thus no upward beam. The result is that atoms above a gap are pushed out of the trapping region by the unbalanced downward beam. To overcome this problem the atoms are trapped off-centre in the pyramid by a distance approximately equal to half of

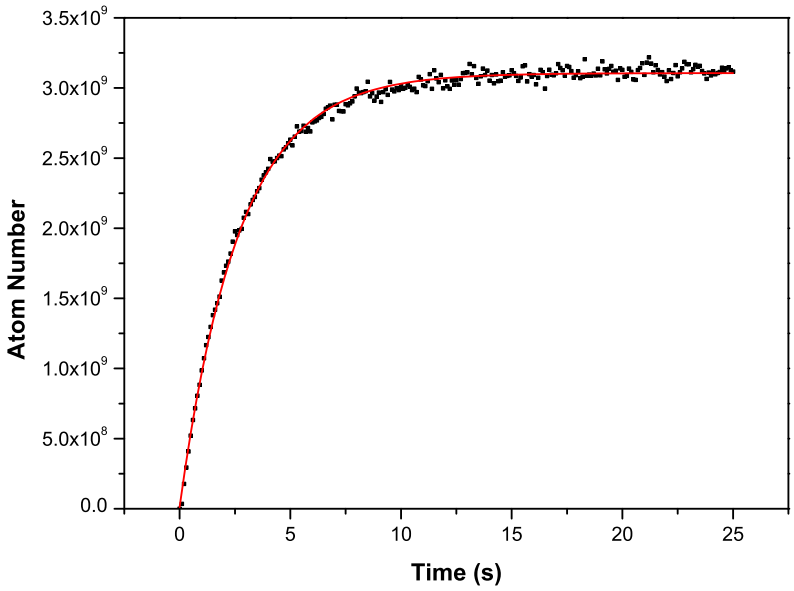

Figure 6.1: The atom number in the MOT versus time during MOT loading. The red line is an exponential fit to the data.

the ∼8 mm cloud diameter such that no portion of the cloud is above a gap between the mirrors. Trapping off-centre in the pyramid meant it was necessary to add a horizontal bias field to move the atoms out of the pyramid during the transport sequence described in subsection 6.2.1. In order to trap the atoms off-centre in the pyramid, whilst still achieving good power balancing between the MOT beams, the central axis of the input beam was set off-centre in the pyramid. The magnetic field was centred as accurately as possible on the resulting point of intersection of the six MOT beams by adjusting the position of the MOT/Transport magnetic coil pair both vertically and in the horizontal plane. Minimising the displacement between the centre points of the magnetic field and the light beams is also important for the stage when atoms are loaded from the MOT into the magnetic trap. Any displacement will result in a shift in the position of the atom cloud during loading into the magnetic trap, resulting in heating of the atom cloud and a reduction in its final phase space density in the magnetic trap.

The degree of power balancing achieved by fine adjustment of the input beam

position, and the degree to which stray magnetic fields were cancelled, was determined by observing the expansion of the MOT cloud when the magnetic field was turned off. Following optimisation of these parameters, the cloud was observed to expand fairly isotropically indicating reasonable beam power balancing. However, the highly isotropic and slow expansion typical of a well-optimised six-beam MOT was not achievable. This ruled out the possibility of performing true optical molasses cooling in which the magnetic field is completely turned off for several milliseconds and for which negligible expansion of the cloud when the magnetic field is turned off is a prerequisite. The beam power balancing was sufficient, however, to allow the magnetic field to be considerably reduced for several milliseconds. This measure was employed in the compressed MOT stage outlined in the next subsection.

Before loading the MOT a sufficient background pressure of rubidium must be introduced into the MOT chamber. For this, a current of 2.9 A is passed through one of the pairs of rubidium dispensers. After about 15 minutes running at this current the rubidium pressure is sufficient to allow the MOT to be fully loaded with atoms. The same dispenser current is then maintained throughout the running of the experiment. This dispenser current was chosen as a compromise: higher currents, whilst giving a larger atom number in the MOT, would more rapidly deplete the dispensers and reduce the lifetime of magnetically trapped atoms in the MOT chamber by increasing the rubidium vapour pressure; lower currents would result in a longer MOT loading time and a smaller atom number. The second pair of dispensers has so far not been used and is being kept in reserve.

The number of atoms in the MOT versus loading time is shown in figure 6.1. The MOT is fully loaded after approximately 20 s which is the loading time used in the standard experimental sequence. The average atom number in the MOT

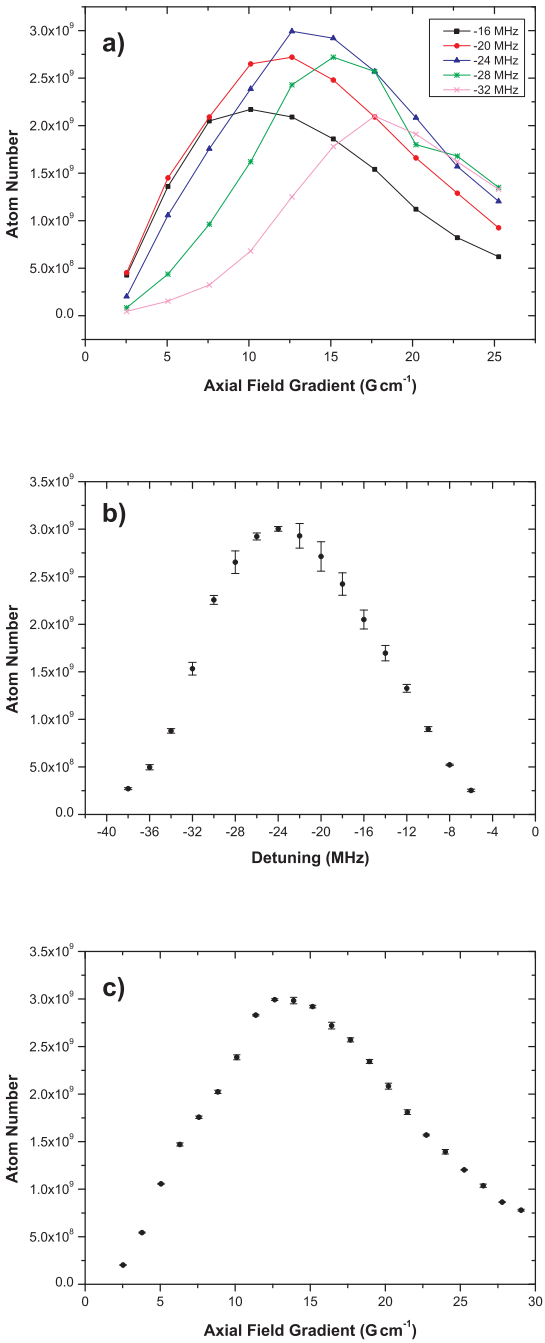

Figure 6.2: MOT atom number optimisation: a) Atom number versus magnetic field gradient for several cooling light frequency detunings, b) Atom number versus frequency detuning of the cooling light with optimum, 13.9 G cm^{-1} magnetic field gradient, c) Atom number versus magnetic field gradient with optimum, -24MHz frequency detuning of the cooling light.

after this loading time is 3×10^9.

The relationship between the final number in the MOT and the magnetic field gradient and frequency detuning of the cooling light is shown in figure 6.2. The maximum atom number is obtained for a frequency detuning and magnetic gradient of $-24\,\mathrm{MHz}$ or approximately -4Γ, and $13.9\,\mathrm{G\,cm^{-1}}$ respectively, which are the values used in the standard experimental sequence. The repumping light power entering the MOT was adjusted to that which gave the largest final atom number in the MOT. This power was controlled by adjusting the final $\lambda/2$ waveplate before the tapered amplifier diode in the setup in figure 5.3.

The number of atoms in the MOT typically varies by a few percent between experimental runs. This change is mainly due to fluctuations in the MOT beam power caused by variations of the coupling efficiency into the MOT optical fibre. The small changes in the position of the MOT/Transport coils incurred following each transport sequence also contribute to the change in MOT number between experimental runs. With the exception of these minor fluctuations, the MOT has operated stably for several months and no major adjustments of the MOT telescope position or configuration have been required.

6.1.1 Compressed MOT

Before loading the atoms into the magnetic trap the size of the cloud in the MOT must be reduced in a compressed MOT (CMOT) stage. This serves two purposes: first, it increases the number of atoms that fit inside the confines of the magnetic trap, and second it reduces the potential energy of the cloud in the magnetic potential. A larger atom cloud will have greater potential energy when loaded into the magnetic trap, and this energy will be converted into heating of the atoms. As discussed in subsection 2.2.3, the size of the cloud in a large MOT is limited by the

outward pressure created by multiple scattering of cooling light photons. To reduce the cloud size the degree of scattering must be reduced. In this experiment the approach taken to MOT compression was the third of those outlined in subsection 2.2.4, in which the magnitude of the frequency detuning of the cooling light is increased and the magnetic field gradient reduced simultaneously. This acts both to reduce the rescattering in the cloud and also increase the size of the region over which sub-Doppler processes are active, to give a higher final phase space density. The CMOT stage in the experiment lasts for 50 ms. The values for the frequency detuning and the magnetic field gradient used during this stage were optimised by measuring the atom number loaded into the magnetic trap using fluorescence imaging (this method of imaging is outlined in the next subsection).

As an initial CMOT optimisation, the values of the frequency detuning and the magnetic field gradient were switched to new values at the start of the 50 ms CMOT period and kept constant at this value throughout the 50 ms. The results of this optimisation are shown in figure 6.3. A sharp increase in atom number was observed for lower values of the field gradient. The atom number also increased as the magnitude of the frequency detuning was increased. This indicates that the cloud has a higher phase space density during the CMOT phase for these values of the parameters, such that more atoms fit inside the confines of the magnetic trap. This behaviour is in agreement with the MOT compression theory in subsection 2.2.4.

During further optimisation, which took place after the atom transport system had been brought online, it was found that the best values for the atom number and phase space density after loading into the TOP trap were obtained when the CMOT parameters were *ramped* rather than held constant. The optimum sequence involved ramping the frequency detuning and the magnetic field gradient

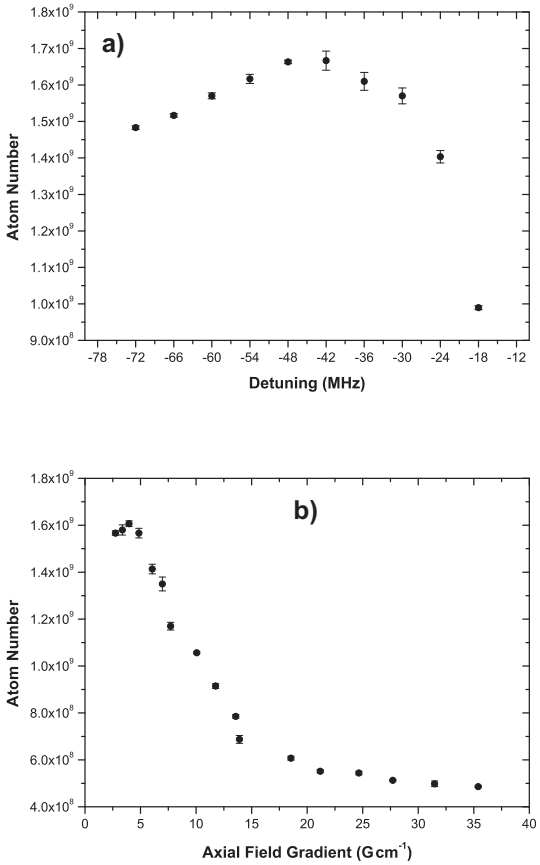

Figure 6.3: Optimisation of the atom number loaded into the magnetic trap: a) atom number versus cooling light frequency detuning with optimum 4.9 G cm^{-1} magnetic field gradient, b) atom number versus magnetic field gradient with optimum -42 MHz frequency detuning.

continuously over the 50 ms CMOT duration. The frequency detuning was ramped down to -38 MHz over the first 40 ms, and then further ramped down to -78 MHz in the final 10 ms. The magnetic field gradient was ramped down continuously during the 50 ms to a final value of 1.5 G cm^{-1}. This CMOT sequence was used in the standard experimental sequence used to produce BEC.

6.1.2 Magnetic Capture

At the end of the 50 ms CMOT stage, the repumping light was turned off 2 ms before the cooling light. This acted to 'pump' the atoms out of the $|F = 2\rangle \rightarrow$

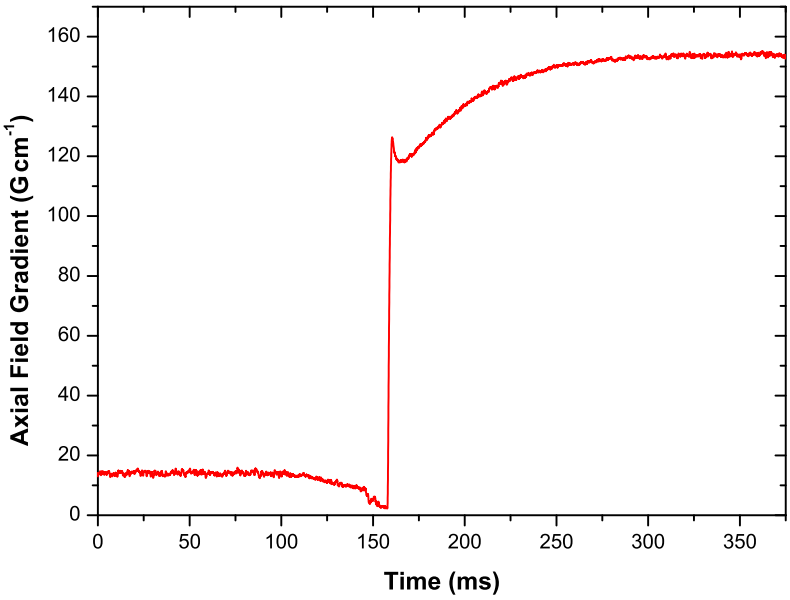

Figure 6.4: Magnetic field gradient at the position of the atoms versus time during the magnetic trapping stage in the MOT chamber.

$|\mathrm{F}' = 3\rangle$ cooling cycle and into the F=1 state in which the atoms are magnetically trapped and transported. At the same time that the cooling light was turned off the magnetic gradient was rapidly jumped to 125 $\mathrm{G\,cm^{-1}}$ in 1.5 ms using the quick-start circuit described in section 5.4 to capture the full cloud from the CMOT stage. The gradient was then ramped up in approximately 200 ms by the power supply acting alone to the full 150 $\mathrm{G\,cm^{-1}}$ gradient used for transport. This sequence for ramping up the magnetic trap is shown in figure 6.4. In this way, approximately one half of the atoms from the CMOT cloud – those in the low-field-seeking, $|\mathrm{F} = 1, m_F = -1\rangle$ substate – were trapped in the magnetic trap.

During the transfer of the atoms from the MOT to the magnetic trap it was observed that the atom cloud underwent a rapid jump in position, despite the care taken to align the centre of the magnetic field with the centre of the MOT beams. It is suspected that this rapid movement was caused by eddy currents induced in the metal components surrounding the atom cloud by the rapidly changing magnetic field. The most likely site of the eddy currents is the steel blocks onto

which the MOT mirrors are glued, which are in close proximity to the atom cloud. Although this problem does not affect the fraction of atoms loaded into the magnetic trap, which matches that achieved in other experiments very well [114], we suspect it causes considerable heating of the atoms. Unfortunately, the presence of the eddy currents makes it impossible to carry out time-of-flight temperature measurements in the MOT chamber to characterize this suspected heating. Such measurements would require releasing the atom cloud from the magnetic trap to allow ballistic expansion of the cloud, however the perturbations to the atom cloud position caused by the eddy currents destroy the cloud during this expansion. A measurement of the temperature of the atom cloud can only be made once the atoms have been transported to the science cell.

The atom number in the magnetic trap was measured using fluorescence imaging as for the MOT cloud. Once the full, $150\,\mathrm{G\,cm^{-1}}$, magnetic field gradient had been reached the repumping light was turned on for 2 ms before the cooling light to pump the atoms back into the $F = 2$ state. Following 4 ms of illumination with both repumping and cooling light an image of the fluorescence from the atoms was taken and equation 5.4 used to give the total atom number.

Once the full gradient of the magnetic trap had been reached the atoms were transported out of the MOT chamber by translating the MOT/Transport coils. This atom transport stage is described in the following section.

6.2 Atom Transport Optimisation

As discussed in section 4.3, the aim in the atom transport sequence was to move the atoms from the MOT to the science cell with minimal loss of atoms and minimal decrease in phase phase density. This section gives details of the experimental sequence used to achieve this. Following the planned approach to implementing

Stage	**Axial magnetic field gradient ($\mathbf{G\,cm^{-1}}$)**	**Cooling light frequency detuning (MHz)**	**Repumping light on/off**	**Cooling light power (mW)**	**Duration (ms)**
MOT loading	13.9	-24	on	~ 150	20 s
CMOT 1	$4.9 \rightarrow 3.2$	$-24 \rightarrow -38$	on	~ 150	40 ms
CMOT 2	$3.2 \rightarrow 1.5$	$-38 \rightarrow -78$	on	~ 150	10 ms
Pumping into F=1 state	1.5	-78	off	~ 150	2 ms
Capture in magnetic trap	$1.5 \rightarrow 125$	–	off	0	1.5 ms
Ramp to full gradient	$125 \rightarrow 150$	–	off	0	200 ms

Table 6.1: Summary of the parameters for the MOT, compressed MOT, and magnetic capture stages.

the atom transport outlined in subsection 4.2.5, the atoms were first transported all of the way to the science cell in the moving Transport coils. The optimisation of this approach makes up the majority of this section. This first approach to transport was used in the experimental sequence outlined in the next chapter in which BEC was produced. The second, hybrid approach to transport involved moving the atoms the majority of the distance between the MOT and the science cell in the Transport coils, and the rest of the way by ramping the current in the Transfer coils. Subsection 6.2.3 outlines the preliminary testing of this transport approach.

In order to optimise the moving coils approach to transport, the atom cloud was transported to the science cell and imaged using the horizontal absorption imaging setup described in section 5.8. The atom cloud was characterised at three points in the magnetic trapping sequence: after initial loading from the Transport coils into the quadrupole potential produced by the Quadrupole coils, following a period

of RF evaporation in this potential to reduce the cloud temperature, and after loading into the TOP trap. The first stage allowed coarse optimisation of the total transported atom number. The second stage allowed more precise measurement and optimisation of this number and in combination with the third stage, in which the temperature and phase space density of the cloud were measured, allowed a complete optimisation of the movement parameters in the transport profile.

6.2.1 Transporting out of the MOT Chamber: Transverse Bias Field Optimisation

In initial attempts to transport the atoms it was found that most atoms were lost before reaching the science cell. In order to establish at which point along the vacuum system the atoms were being lost a sequence was used in which the atoms were transported a set distance along the transport axis and then returned to the MOT chamber. The remaining atom number was then measured through fluorescence imaging. The distance that the atoms were transported was increased incrementally. The results of these measurements are shown in figure 6.5.

A clear drop in atom number is observed after transporting a distance of approximately 2 to 3 cm from the centre of the MOT. This drop is much more abrupt than the decrease that is predicted to occur purely for collisions with background gas molecules in the MOT chamber (the predicted drop from background losses is denoted in figure 6.6 by the solid line). This 2 to 3 cm distance corresponds to the exit slit of the pyramid. We suspect that the need to trap off-centre in the MOT results in the atom cloud clipping the edge of one of the MOT mirrors during transport. Additional smaller drops in atom number are seen at distances of 6 and 25 cm, and these are thought to be due to the edge of the cloud clipping the vacuum system at these points.

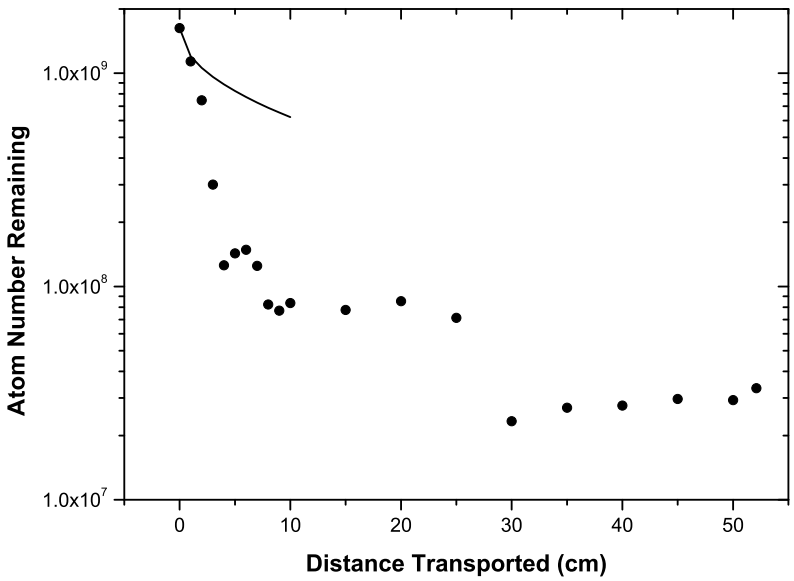

Figure 6.5: Atom number remaining following transport along the transport axis and back to the MOT versus outward distance travelled. The solid line is the predicted decay in atom number from background losses alone, based on the measured MOT chamber lifetime.

In order to overcome these losses the transverse bias coil specified in subsection 5.4.3 was used to generate a field to bias the centre of the quadrupole potential, and thus shift the atom cloud position, during the transport sequence. The timing of the ramping of this bias field relative to the transport movement profile, and the magnitude of the field, were optimised by measuring the atom number after transferring the atoms into the final quadrupole potential.

In order to transfer the atoms between the Transport coil potential and the Quadrupole coil potential in an adiabatic manner the following sequence was used. First the Transport coils were moved from the MOT to the science cell to be coaxial with the Quadrupole coils. Then the magnetic field gradient (N.B. all magnetic field gradients quoted in the following are for the *axial* direction) produced by the Quadrupole coils was ramped up from zero to $99\,\mathrm{G\,cm^{-1}}$ in 100 ms. The magnetic field gradients produced by the Transport coils and the Quadrupole coils were then ramped simultaneously in 800 ms; the former from 150 to $0\,\mathrm{G\,cm^{-1}}$ and the latter

from 0 to 331 G cm^{-1}. The Quadrupole field gradient was then further ramped up to its maximum value, 794 G cm^{-1} in 500 ms to give the maximum density and collision rate for the subsequent evaporation stage in the quadrupole potential.

It should be noted that these parameters for the current ramps were only used in the initial optimisation measurements reported in this chapter and not the final BEC experimental sequence presented in the next chapter. Owing to the necessary change of TOP amplifier (see section 5.6 for details) which took place after the initial optimisation measurements reported in this section had been carried out, and the subsequent recalibration of the Quadrupole and TOP fields, the values of the Quadrupole field gradient, and the times of the above Transport-to-Quadrupole ramps were changed in the final BEC sequence. The final current ramps used in the BEC sequence are summarised in table 6.2. No discernible change in the final atom number and phase space density of the atom cloud in the TOP trap were observed when these changes to the current ramps were made.

The optical density of the atom cloud in the quadrupole potential was too high to allow in-trap absorption imaging, therefore the magnetic potential was first turned off and the cloud allowed to expand ballistically before imaging. The expansion time must be carefully chosen at this stage since for times of less than approximately 4 ms the optical density of the cloud was still high enough to render it opaque to the imaging light, and at times greater than approximately 4.5 ms the cloud no longer fit within the imaging field of view. For the optimisation of the bias coil sequence a value of 4.5 ms was used to ensure that the density was low enough for imaging and that most of the cloud was in the field of view. Since a small portion of the cloud did not fall within the field of view the resulting number measurements are a slight underestimate of the true number in the cloud.

The results of the transverse bias field optimisation are shown in figure 6.6.

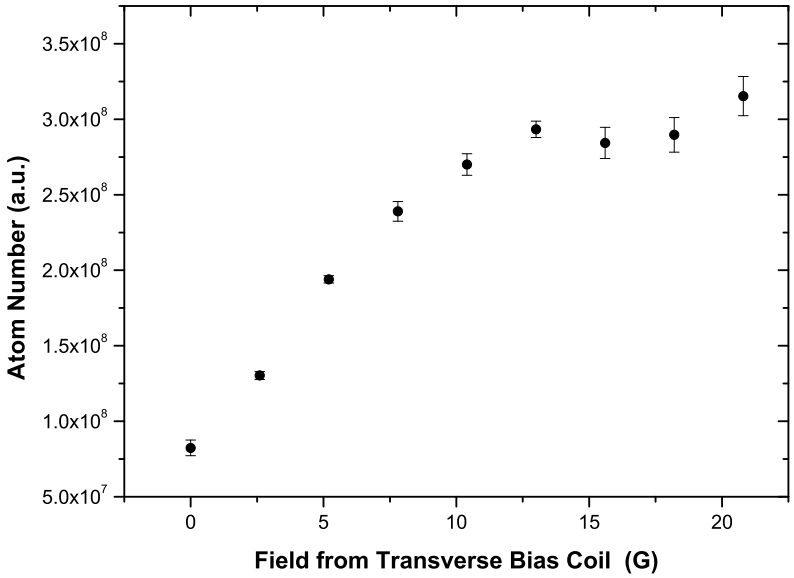

Figure 6.6: Atom number transferred to the final quadrupole potential versus the magnetic field from the transverse bias coil. This field is in the xy-plane, perpendicular to the transport axis and at the location of the atoms. The field was calculated from the current in the coil. The timing of the application of the field relative to the transport sequence is given in table 6.2.

The atom number increases with increasing bias field and levels off to a maximum of approximately 3×10^8 at a bias field of 13 G. This is the typical largest atom number that could be transported into the science cell prior to the optimisation of the transport movement profile outlined in the next subsection. A value of 18 G, corresponding to a current of 70 A through the push coil, gave the greatest transfer of atoms and was used in the standard experimental transport sequence.

The optimum bias field sequence, which was used in the BEC experimental sequence, was the following. The bias field was ramped up in 100 ms after which the transport movement profile was triggered. The field was maintained at a constant value until 700 ms before the end of the transport movement profile at which time it was ramped down to zero in 300 ms. These slow ramping times ensured adiabatic changes in the atoms' position and thus little or no heating of the atoms.

6.2.2 Optimisation of the Transport Movement Profile

The controllable parameters in the movement profile of the transport coil translation stage were the acceleration and deceleration, and the velocity in the central, constant velocity stage of the profile. Only constant acceleration and deceleration are possible with our translation stage and the value of these parameters fixes the duration of the constant velocity stage in the middle of the movement profile. The total transport distance, set by the separation of the centre of the MOT and the centre of the Quadrupole coils was 52 cm. The movement profile was optimised by scanning one of the three movement parameters whilst holding the others constant. Due to the aforementioned difficulties in accurately measuring the atom number initially loaded into the final quadrupole potential, the atom number was measured following a 5 s period of RF evaporation to remove the hottest atoms from the cloud and reduce its size. In the evaporation sequence the magnetic gradient was kept at its maximum, $794\,\mathrm{G\,cm^{-1}}$ (in the final BEC experimental sequence this value was $771\,\mathrm{G\,cm^{-1}}$), and the frequency of the RF radiation was swept in a linear ramp from 120 to 65 MHz in 5 s. Following this evaporation stage the atom cloud was cold enough to be loaded into the TOP trap. For full details of the TOP trap loading optimisation see chapter 7. For each set of movement profile settings the atom number, phase space density and temperature were measured in the TOP trap. The results of the movement profile optimisation are shown in figures 6.7 and 6.8.

An increase in atom number was seen with increasing acceleration which was most likely due to the correspondingly shorter time spent in the poor vacuum of the MOT chamber at these higher accelerations. A maximum atom number was observed for accelerations between 0.8 and $1.2\,\mathrm{m\,s^{-2}}$. Higher accelerations resulted in increased vibrations from the translation stage which perturbed the locking of

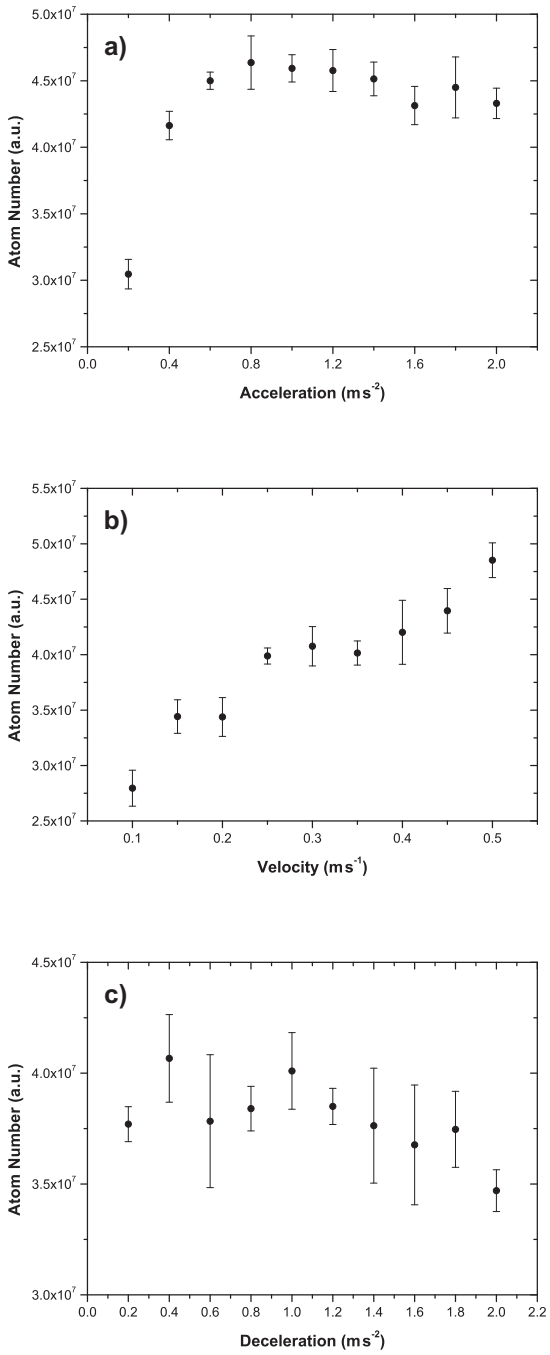

Figure 6.7: Atom number transported to the final quadrupole potential versus a) acceleration, b) velocity, and c) deceleration of the translation stage, and following RF evaporation in the potential.

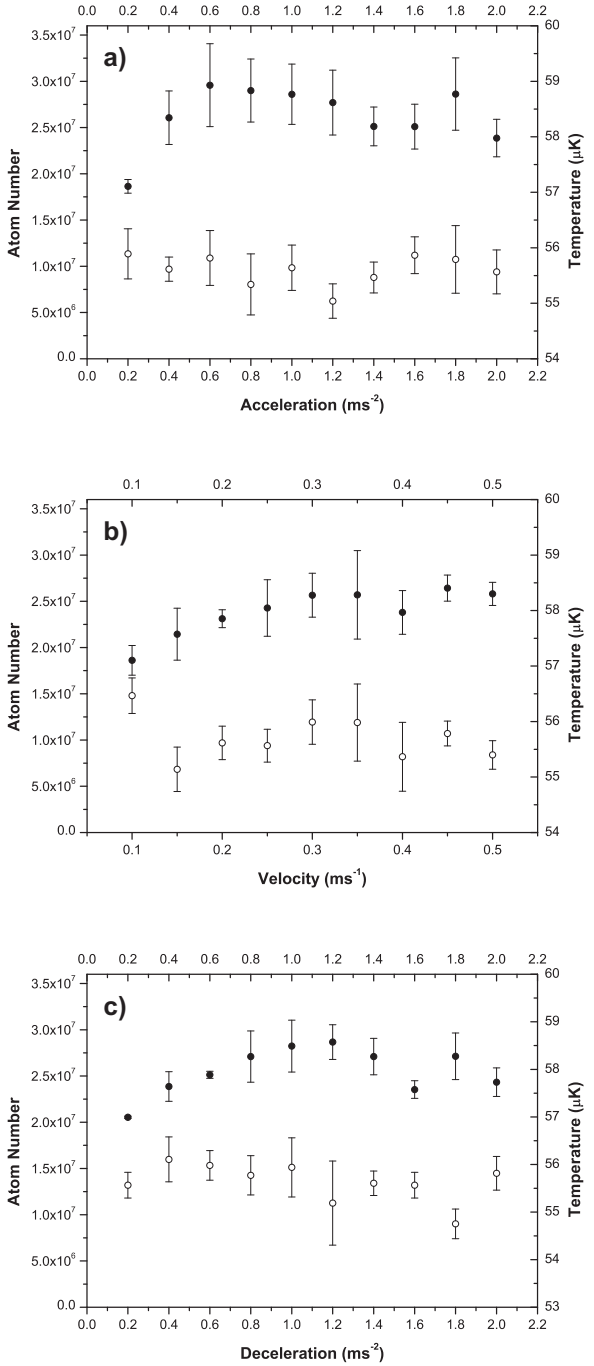

Figure 6.8: Atom number (solid circles) transported in the TOP trap and temperature (empty circles) versus a) acceleration, b) velocity, and c) deceleration of the translation stage, and following RF evaporation in the quadrupole potential.

the Master and Repumping lasers, situated on the same optical table as the transport translation stage. The perturbations to the laser frequency adversely affected the atom number measurement which accounts for the drop in measured number for these accelerations, and ruled out using these higher values of acceleration.

The atom number increased approximately linearly with velocity. Again, we suspect this increase to be due to the reduced time spent in the bad vacuum for higher velocities. As with large values of acceleration, large values of velocity – those above approximately $0.3\,\mathrm{m\,s^{-1}}$ – resulted in perturbations to the laser locking, and adversely affected the imaging. Unlike the acceleration, the deceleration of the stage had no discernable effect on the final atom number. We suspect that since the atoms are in a much better vacuum during the deceleration stage, variations in the time spent decelerating have little effect on the atom number.

The measurements in the TOP trap show that there is no observable variation in temperature over the whole range of transport parameters. This is in agreement with other transport experiments in which minimal heating was observed in the transport stage [22]. The variation in number follows a similar pattern to that observed in the quadrupole potential.

In the final transport sequence used in the experimental sequence used to produce BEC, values of $0.4\,\mathrm{m\,s^{-2}}$, $0.4\,\mathrm{m\,s^{-2}}$, and $0.5\,\mathrm{m\,s^{-1}}$ were used for the acceleration, deceleration and velocity respectively. These values were chosen as a compromise so that the atoms were moved out of the bad vacuum sufficiently quickly to limit losses caused by collisions with background gas molecules but slowly enough such that the translation stage vibrations did not perturb the laser locking. With these movement parameters the total time for the transport sequence was 2.28 s.

This movement profile consistently transferred $\sim 4.5 \times 10^8$ atoms into the Quadrupole potential. As mentioned above, this measurement of the atom number

Stage	**Transverse bias coil field (G)**	**Transport axial field gradient ($\mathbf{G\,cm^{-1}}$)**	**Quadrupole axial field gradient ($\mathbf{G\,cm^{-1}}$)**	**Duration (ms)**
Bias atoms horizontally in MOT chamber	$0 \rightarrow 18$	150	0	100
Transport 1	18	150	0	1700
Transport 2	$18 \rightarrow 0$	150	0	300
Transport 3	0	150	0	280
Hold in Transport field in science cell	0	150	0	120
Ramp up Quad.	0	150	$0 \rightarrow 63$	100
Ramp down Transport and ramp up Quad.	0 0	$150 \rightarrow 0$	$63 \rightarrow 424$	200
Ramp up Quad.	0	0	$424 \rightarrow 771$	500

Table 6.2: Summary of the current ramps in the atom transport stage of the optimised sequence used to produce a Bose-Einstein condensate.

in the large cloud initially loaded into the Quadrupole potential was probably an underestimate because of the relatively low intensity of the probe beam and the relatively high optical density of the cloud.

6.2.3 Demonstration of the Hybrid Transport System

This subsection details the preliminary testing of the hybrid system outlined in section 5.5 which will ultimately be the method of atom transport employed in conjunction with the high resolution imaging system. The optimisation of the moving coils transport approach detailed above demonstrated that this approach is robust, and consistently enables the transfer of $\sim 30\%$ of the atoms magnetically trapped in the MOT chamber to the science cell provided the acceleration of the coils is large enough to limit losses in the poor vacuum of the MOT chamber. The number of atoms transported to the science cell, and the temperature of the atoms, are relatively insensitive to small changes to the movement parameters of

the translation stage.

With this in mind, the starting approach to hybrid transport was to use the same movement parameters as in the standard sequence used to produce BEC. The Transport coils were displaced 43 cm from the MOT, in a time of 2.08 s, such that the axis of the Transport coils was aligned with the Push coil (as illustrated in figure 5.7 (b)). The atoms were then transported the remaining 9 cm to the final trapping site by switching the currents in four coils: the Transport, Push, Auxiliary and Quadrupole coils. The general approach to this sequence followed that of previous fixed coil transport experiments in which the fields from three coil pairs were ramped simultaneously, as discussed in section 5.5. In this way, changes to the aspect ratio of the cloud and net magnetic field gradient in the vicinity of the atoms could be minimised. The coil currents were ramped over ~ 100 ms timescales so that the change in the atom cloud position, and any changes in its aspect ratio were kept adiabatic.

The current ramps which resulted from this optimisation are shown in figure 6.9. These ramps consistently allowed $\sim 2.75 \times 10^8$ atoms to be transferred into the final Quadrupole potential. This is approximately 60% of the typical 4.5×10^8 atoms transported into the Quadrupole potential using the Transport coils alone.

As a further proof-of-principle demonstration, the hybrid transport ramps were used in conjunction with a slightly modified version of the evaporative cooling ramps outlined in the next chapter. This led to the formation of a BEC with an atom number several times smaller than that typically obtained using the moving coils transport approach.

Whilst these results give a preliminary confirmation of the efficacy of the hybrid transport system, further optimisation of the current ramps in this sequence is required to give the maximum possible transfer of atoms into the final magnetic

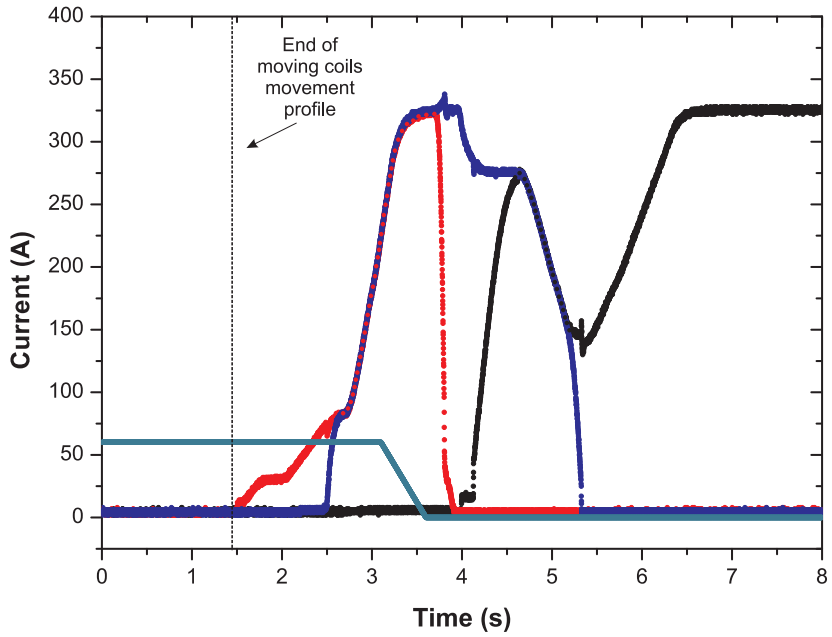

Figure 6.9: Traces of the current ramps used in the transfer stage of atom transport. The traces shown are for the Transport (green), Push (red), Auxiliary (blue) and Quadrupole (black) currents.

trap, and the maximum atom number in the final condensate. This is important for experiments which involve loading of the atoms into complex potentials such as the RF-dressed potentials outlined in chapter 3, where large and unavoidable atom loss occurs during loading of the potential.

Chapter 7

BEC Production

This chapter outlines the final cooling stages used to reduce the temperature of the atoms to below the BEC transition temperature. Following transport into the science cell the atoms have an average temperature of several hundred millikelvin. For the typical highest atom densities in the TOP trap ($n = 10^{13} - 10^{14}\,\mathrm{cm}^{-3}$) the BEC transition temperature is on the order of 100 nK and so the average temperature must be reduced by approximately four orders of magnitude to attain quantum degeneracy. This reduction in temperature is achieved through evaporative cooling of the atom cloud. The atom cloud is first cooled in the quadrupole magnetic potential before being loaded into the TOP trap in which the cloud is cooled to quantum degeneracy.

The structure of this chapter is as follows. First, the principles of evaporative cooling are presented with a discussion of the important parameters that must be considered when optimising the cooling ramps. This is followed by the details of the evaporation ramp in the quadrupole potential and the subsequent loading of the atoms into the TOP trap. Finally, the optimisation of the evaporation ramps

used in the TOP trap to reach BEC is presented.

7.1 Evaporative Cooling Theory

In conventional evaporation the hottest atoms in an ensemble have sufficient kinetic energy to escape and carry away more than the average share of thermal energy. The remaining atoms then rethermalise to a lower average temperature. The evaporative cooling of ultracold gases works on the same principle but rather than being spontaneous the evaporation is *forced* by controlling the form of the potential in which the atoms are trapped. The evaporation rate and the temperature of the atoms removed from the trapping potential are chosen to maximise the increase in phase space density throughout the cooling ramps and maximise the atom number in the resulting BEC.

In this experiment, two methods are used to evaporate atoms: radio-frequency (RF) evaporation and evaporation via non-adiabatic transitions at the locus of $|\mathrm{B}| = 0$ in the TOP trap. RF evaporation is the typical approach used in the majority of BEC experiments since it can be used in conjunction with most types of trapping potential, whilst evaporation at the field zero is peculiar to the TOP trap. The following subsection gives an overview of the theoretical background to the optimisation of the evaporation ramps. The principles of the two evaporation methods are then outlined.

7.1.1 Optimising Evaporation

A comprehensive overview of evaporative cooling in ultracold gases is given in [115]. This subsection summarises the key parameters which must be considered when optimising the evaporative cooling ramps.

The aim in the evaporative cooling stage is to lower the atom temperature to below the critical temperature for BEC with as many atoms remaining as possible. To achieve this the following two criteria must be met. First, the cloud must rethermalise sufficiently quickly during evaporation to maximise the thermal energy carried away by each atom removed from the trap. Second, the losses from inelastic collisions must be kept small enough so as not to compromise the increase in phase space density.

Since rethermalisation relies upon elastic collisions, the first criterion requires the elastic collision rate to be large compared to the evaporation rate. The mean elastic collision rate can be approximated by:

$$\Gamma_{el} = \bar{n}\bar{\sigma}\bar{v} \tag{7.1}$$

where $\bar{n}$ is the mean atom density, $\bar{\sigma} = 8\pi {a_s}^2$ is the mean elastic collision cross-section (where a_s is the scattering length, equal to 5.3×10^{-9} m for the $|\mathrm{F} = 1, m_F = -1\rangle$ substate of ^{87}Rb), and $\bar{v} = \sqrt{\frac{16k_BT}{\pi m}}$ is the mean atom velocity in a harmonic potential.

For a harmonic potential the mean atom density is given by:

$$\bar{n} = \frac{n(0)}{2\sqrt{2}} = N\omega_x\omega_y\omega_z\left(\frac{m}{4\pi k_BT}\right)^{\frac{3}{2}} = \frac{N}{2\sqrt{2}\pi^{\frac{3}{2}}\sigma_x\sigma_y\sigma_z} \tag{7.2}$$

where $n(0)$ is the peak density, and σ_x, σ_y and σ_z are the cloud 1/e radii in the x, y and z directions respectively.

From the above equations it can be seen that increasing the trapping confinement gives a higher atom density and elastic collision rate. For this reason the trapping frequencies are maximised where possible during the evaporation ramps.

The second of the above optimisation criteria requires the ratio of the elastic to

inelastic collision rates, $R_{coll} = \Gamma_{el}/\Gamma_{in}$, to be kept large. As discussed in subsection 4.3.3, there are three forms of inelastic collision which result in atom loss from a magnetic trap: one-, two-, and three-body collisions. In one-body collisions a trapped atom is ejected from the trap by a background gas atom. The rate for this process is set by the background vacuum pressure and is given by $1/\tau$, where τ is the atom lifetime in the TOP trap. This lifetime was measured to be $109 \pm 12\,\mathrm{s}$ in the science cell, giving $1/\tau = 9.1 \times 10^{-3}\,\mathrm{s}^{-1}$.

Two- and three-body collisions were discussed in subsection 4.3.3 and the loss rate constants for these processes have been estimated as $1.6 \times 10^{-16}\mathrm{cm}^3\,\mathrm{s}^{-1}$ [105] and $L = 4 \times 10^{-30}\,\mathrm{cm}^6\,\mathrm{s}^{-1}$ [104] respectively for ^{87}Rb. The typical peak atom densities in evaporation ramps to BEC are between 10^{10} and $10^{14}\,\mathrm{cm}^{-3}$. So even at highest densities the losses caused by two-body losses remain negligible. The three-body loss rate only becomes significant as the highest densities are reached upon formation of the BEC [115]. On the basis of these low two- and three-body rates it was assumed that only one-body losses are significant during the evaporation ramps so that the inelastic loss rate can be well approximated as simply $1/\tau$, giving $R_{coll} = \Gamma_{el}\tau$.

The key to making the evaporation sufficiently efficient to produce BEC is to enter into the regime of *runaway evaporation* in which the elastic collision rate remains constant or increases as the evaporation progresses. To enter into this regime the value of R_{coll} must equal a minimum value which is set by the ratio of the thermal energy of the evaporated atoms and the average thermal energy of an atom in the cloud, referred to as the *truncation parameter*,

$$\eta = \frac{E_{evap}}{k_B T} \tag{7.3}$$

where E_{evap} is the thermal energy of the evaporated atoms. In RF-evaporation

E_{evap} is the energy at which the RF is resonant, E_{RF}, whilst in evaporation with the field zero E_{evap} corresponds to the depth of the TOP potential.

It has been shown that a value of $\eta \sim 6$ gives the smallest minimum value of R_{coll} for entry into the runaway evaporation regime [52,115], with the corresponding value of R_{coll} being approximately ~ 300. These figures were used as a guideline when optimising the evaporation ramps to give runaway evaporation.

7.1.2 Radio-Frequency Evaporation

In RF evaporation the hottest atoms are selectively removed from the trapping potential by applying an RF field which transfers them to untrapped magnetic substates. For an atom to be transferred between trapped and untrapped substates in this way the frequency of the applied RF must be resonant with the splitting of the Zeeman levels in the atom. For a particular frequency of applied radio-frequency radiation, ν_{RF}, this condition is satisfied when the atom is subject to a magnetic field, B_{res}, that fulfils:

$$B_{res} = \frac{h(\nu_{RF} - \nu_0)}{g_F m_F \mu_B} \tag{7.4}$$

where ν_0 is the frequency corresponding to the bottom of the trapping potential, which for a TOP trap is: $\nu_0 = g_F m_F \mu_B B_T / h$.

For our case of atoms trapped in the $|\mathrm{F} = 1, m_F = -1\rangle$ substate, an atom passing through a magnetic field which fulfils the above resonance condition will be transferred to either the untrapped $|\mathrm{F} = 1, m_F = 0\rangle$ substate or to the anti-trapped $|\mathrm{F} = 1, m_F = +1\rangle$ substate.

The selective removal of the hottest atoms is made possible by the fact that both the magnitude of the magnetic field and the potential energy of an atom

increase away from the trap centre. Hotter atoms follow trajectories which take them further from the trap centre where the magnetic field is higher. The RF frequency is then chosen to be resonant with the hotter atoms in the outermost part of the trap where the magnetic field is large, and these atoms are ejected from the trapping potential. Then only atoms with thermal energy, $E_{RF} \geq g_F m_F \mu_B B_{res}$, are ejected from the trapping potential.

In order to reduce the temperature of the cloud, the RF frequency is continuously ramped down so that progressively lower temperature atoms are ejected from the trapping potential. The rate of this ramp is chosen to give the optimum evaporation efficiency.

7.1.3 Evaporation at the Zero of Magnetic Field

In this method of evaporation the locus of zero magnetic field inherent to the TOP trap – the circle of death – described in section 5.6, removes the hottest atoms from the potential. An atom whose trajectory passes onto this circle undergoes a Majorana spin-flip to an untrapped magnetic substate and leaves the trapping potential. This atom loss is energy selective since only those atoms with sufficient energy to move out to the locus of zero field will be lost. The radius of the circle of death, $r_0 = 2B_T/B'_q$, which sets the limit on the TOP trap depth, is chosen so that only the hottest atoms are ejected from the trap. The cloud is cooled by progressively reducing the radius of the circle by ramping down B_T. The rate at which B_T is ramped and the value of r_0 throughout the ramp are chosen to optimise the evaporation efficiency.

An advantage of this method is that reducing B_T also increases the trapping frequencies, giving a higher atom density and elastic collision rate. The resultant increase in the rate of rethermalisation allows the ramp rate to be increased as the

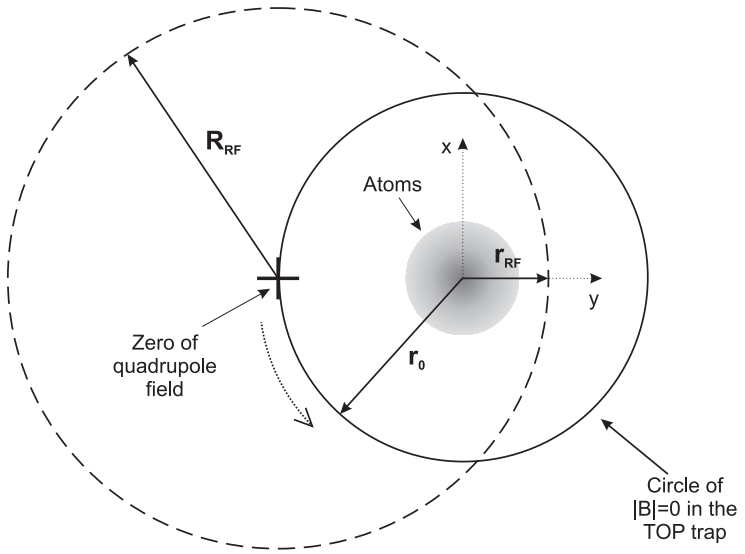

Figure 7.1: Schematic of the instantaneous picture of the TOP trap indicating the two possible methods of evaporative cooling. The figure is a top-down view of the trap. The RF is resonant with the quadrupole field at a radius R_{RF} from the centre of the quadrupole field in the xy-plane. This produces a 'cutting' surface at a distance r_{RF} from the centre of the atom cloud. The circle of zero field in the time-averaged picture, of radius r_0, also provides a locus at which atoms are lost. Which of these two evaporation surfaces gives cooling at a particular time is set by the ratio r_{RF}/r_0.

ramp progresses which facilitates entry into the runaway evaporation regime.

Unfortunately, this method cannot be used to cool the atoms all the way to the BEC transition since the increase in trapping frequencies as B_T is reduced means that eventually the approximation $\omega_z, \omega_r \ll \omega_T$ made in the derivation of the TOP potential, equation 2.32, becomes invalid. When this stage is reached the gain in phase space density given by further decreasing B_T drops off significantly. Therefore in practice B_T is reduced to a point just before this drop in evaporation efficiency is observed. The subsequent cooling to the BEC transition is then carried out using RF evaporation.

7.2 Evaporation in the Quadrupole Potential

As discussed in section 5.6, Majorana losses rule out cooling to the temperatures required to reach BEC in a bare quadrupole potential. Therefore the atoms must first be loaded into the TOP trap which is free from these losses.

The average temperature of the cloud following transport was several hundred microkelvin which is comparable to the maximum TOP trap depth, 361 μK, obtained with the maximum TOP field, $B_T = 43\,\mathrm{G}$. Also, for the typical values of B_T and B'_q required to load the TOP potential, the value of the radius of the locus of zero magnetic field, r_0, is smaller than the radius of the atom cloud in the quadrupole potential. Therefore loading the cloud into the TOP trap immediately after the transport stage would result in the loss of a substantial number of the higher temperature atoms in the cloud. In order to increase the efficiency of this transfer, the cloud temperature must first be reduced and the atom density increased. This was achieved by cooling the atoms in the quadrupole potential in a stage of RF evaporation.

The aim in this evaporative cooling stage was to reduce the cloud size such that it could be loaded into the TOP trap, while keeping the atom number as high as possible. This meant increasing the density of the cloud and decreasing its temperature: that is, increasing its phase space density. Before commencing evaporation the elastic collision rate was maximised to give the best evaporation efficiency. To achieve this, the cloud was compressed by ramping up the quadrupole gradient to its maximum value, $771\,\mathrm{G\,cm^{-1}}$. For this compression to incur a minimum decrease in phase space density it must be carried out on an adiabatic timescale, for which the rate of change of the trapping frequency must be small compared to the trapping frequency:

$$\frac{d\omega(t)}{dt} \ll \omega^2. \tag{7.5}$$

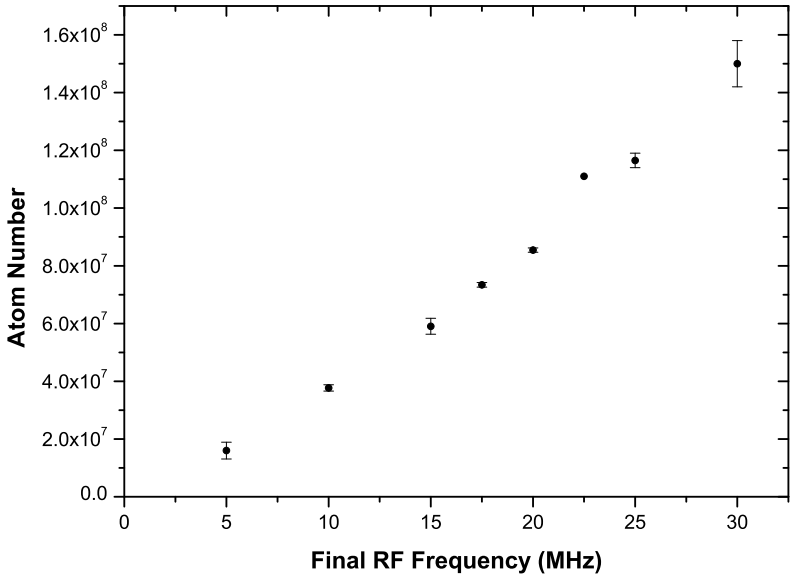

Figure 7.2: The remaining atom number in the quadrupole potential following evaporation versus the final evaporative RF frequency. The starting frequency was 120 MHz for all points and the RF frequency ramp was linear with duration 10 s.

To conform to this the complete compression ramp was carried out over 800 ms, as detailed in table 6.2.

The starting frequency for the RF evaporation was chosen so that the RF cutting surface started outside the cloud to avoid unwanted evaporation. This starting frequency was estimated using equation 7.4, using the expression for a quadrupole field given in equation 2.27. When the starting RF frequency was reduced below 100 MHz a rapid drop off in the final atom number following evaporation was observed indicating that the wings of the cloud were evaporated away at the start of the ramp. For this reason a starting frequency of 120 MHz was used in the final sequence.

The RF frequency was ramped down in a linear ramp lasting 10 s and the final RF frequency was chosen to reduce cloud temperature and size to the point where the entire cloud could be loaded into the TOP trap. In addition, care was taken not to reduce the temperature so low that Majorana losses in the quadrupole potential

became significant.

Figure 7.2 shows the remaining atom number for various final RF frequencies. An RF frequency of 20 MHz was used in the final evaporation sequence. With this final frequency the typical final atom number in the quadrupole potential following evaporation was $\sim 1 \times 10^8$. Based upon the subsequent measurement of the cloud temperature after loading into the TOP trap, and assuming some heating of the cloud during this loading stage, the temperature of the cloud after evaporation in the quadrupole was less than 20 μK.

7.3 Loading the TOP Trap

7.3.1 Optimising the Loading

Following evaporative cooling in the quadrupole potential, the cloud was cold enough to be loaded into the TOP trap. The quadrupole gradient was first ramped down from its maximum value used throughout evaporation to a lower value to facilitate loading of the TOP trap. This quadrupole potential was then transformed into the TOP potential given in equation 2.32 by turning on the TOP bias field. As the TOP bias field is ramped up, the field zero of the quadrupole potential spirals out from the centre of the cloud to larger radii. Majorana losses can occur at this field zero, and the TOP field must be ramped up rapidly to avoid these losses being significant. In this experiment the TOP field was ramped up in approximately 100 μs, which gives no discernible loss of atoms.

The aim in the loading sequence was to avoid a reduction in the phase space density or atom number as the cloud was loaded into the TOP trap. For this, the initial values of the TOP bias field, B_T, and the quadrupole gradient, B'_q, for loading must be chosen to fulfil two criteria. First, the initial TOP trap must be large

enough and deep enough to contain the entire atom cloud, to maximise the atom number. Second, there should be approximate 'mode-matching' between the two traps; the size of the cloud in the quadrupole potential should approximately equal that in the TOP trap. Mode-matching minimises the expansion or compression of the cloud during loading, both of which would result in a decrease in phase space density.

As shown in subsection 2.3.2, the depth of the TOP trap is $g_F m_F \mu_B B_T/4$; a limit set by Majorana losses on the circle of zero magnetic field, of radius $r_0 = 2B_T/B'_q$. These losses also limit the maximum spatial size of the cloud in the radial direction to a radius of r_0. Therefore, to ensure that both the spatial size and the depth of the trap are sufficient to capture the whole cloud, a large value of B_T should be used.

The second, mode-matching criterion cannot be well satisfied in the current experimental setup. This is because the loading sequence involves keeping the quadrupole gradient constant while the TOP field is turned on. The size of the cloud in the TOP trap is then necessarily larger than in the quadrupole potential, and an unavoidable decrease in phase space density of the cloud is incurred. A possible improvement to this sequence, not yet implemented in the experiment, is outlined in the next section. This involves rapidly switching the quadrupole field to a new value when the TOP field is switched on, thus keeping the cloud size approximately constant and conserving its phase space density. Although this approach will give better mode-matching, the inherently different geometries of the quadrupole and TOP potentials mean that perfect mode-matching can never be achieved. However, in the first experiments with TOP traps in our group [52], it was found that mode-matching had a small impact on the phase space density of the cloud loaded into the TOP trap. This is in agreement with theoretical

considerations which show that the phase space density is relatively insensitive to mode mis-match [116].

Following evaporation in the quadrupole potential, and prior to loading the TOP trap, the quadrupole gradient was ramped down to a low value: $62.8\,\mathrm{G\,cm^{-1}}$. This meant that lower TOP fields could be used to produce a trap with a particular value of r_0. An appropriate value for the initial TOP field was found by keeping the quadrupole gradient at $62.8\,\mathrm{G\,cm^{-1}}$ and measuring the number of atoms loaded into the TOP trap for various TOP fields. A decrease in atom number was observed for TOP fields below approximately 6.9 G, corresponding to a radius, r_0 =2 mm. This indicates that at this value of r_0 the field zero of the TOP trap began to cut away atoms at the edge of the cloud. In order to avoid this, and capture all the entire atom cloud, a TOP field greater than 6.9 G must be used for this value of the quadrupole field gradient. The temperature and phase space density of the atom cloud loaded into the TOP trap remained approximately constant over the full range of TOP fields tested (1.7 to 20.8 G). This is to be expected since the degree of mode-matching is approximately the same over this whole range of TOP field values.

The final optimised TOP loading parameters were: B_T=10.3 G, B'_q=$62.8\,\mathrm{G\,cm^{-1}}$, corresponding to a radial trapping frequency of $\omega_r = 2\pi \times 6.2\,\mathrm{Hz}$ and a radius of the circle of death, $r_0 = 3.3\,\mathrm{mm}$. The typical parameters of the cloud after loading into the TOP trap were: $N = 1 \times 10^8$, $T = 20\,\mu\mathrm{K}$. This atom number indicates that essentially the whole cloud had been loaded from the quadrupole potential.

7.3.2 Possible Improvement to the Loading

The above approach of turning on the TOP bias field instantaneously but keeping the quadrupole gradient constant gives relatively poor mode-matching of the cloud

to the TOP potential. A better approach would be to switch the quadrupole field rapidly to a larger value at the same time that the TOP bias field is turned on. In this way, the size of the cloud in the quadrupole potential could be made to match its size in the TOP trap while keeping r_0 sufficiently large to be outside the cloud. The value of B'_q required to achieve this can be found be equating the potential energy of an atom in the TOP and quadrupole potentials. The energy of an atom in the quadrupole potential is:

$$\frac{1}{2} g_F m_F \mu_B B'_q r = \frac{1}{2} k_B T, \tag{7.6}$$

and its energy in the TOP potential is:

$$\frac{1}{2} m {\omega_r}^2 r^2 = \frac{1}{2} k_B T \tag{7.7}$$

where r is the radial distance of the atom from the centre of the potential, and we have equated both the energies to the thermal energy of the atom. For ideal mode-matching we equate these two energies. That is, we assume that the energy of an atom at a particular r in the quadrupole potential is equal to its energy in the TOP potential at the same r. Using the expression for ω_r in a TOP trap gives:

$$r = \frac{8 B_T B'_q}{{B'_T}^2} \tag{7.8}$$

where B'_T is the gradient of the quadrupole field used to generate the TOP trap. Since we also require $r < r_0$ this becomes:

$$\frac{2 B_T}{B'_T} > \frac{8 B_T B'_q}{{B'_T}^2}. \tag{7.9}$$

Thus the mode-matching condition is:

$$B'_T > 4B'_q. \tag{7.10}$$

This expression shows that the quadrupole gradient must increase by at least a factor of four when the TOP field is turned on to give the best mode-matching and for r_0 to remain outside the cloud. Assuming the TOP field and quadrupole gradient currently used during loading of the TOP trap: $B_T = 10.3\,\mathrm{G}$, and $B'_q = 62.8\,\mathrm{G\,cm^{-1}}$, the quadrupole field would need to be jumped to $B'_T = 251.2\,\mathrm{G\,cm^{-1}}$. This ramp up of the quadrupole gradient from B'_q to B'_T would need to be carried out in a time comparable to that taken to ramp up the current in the TOP coils, which is approximately $100\,\mu\mathrm{s}$. The ramping time of the Quadrupole coil power supply acting alone is too slow to allow this. A possible solution would be to divert current from a bypass resistor placed in parallel with the Quadrupole coils, however this has not as yet been installed on the apparatus.

7.4 Evaporation in the TOP Trap

The general approach to evaporation in the TOP trap was similar to that carried out in previous experiments in our group [21, 53, 117]. First, the cloud was adiabatically compressed in order to increase the elastic collision rate and improve the efficiency of the subsequent evaporative cooling. This was followed by a period of evaporation using the locus of field zero. Finally, RF evaporation was used to reduce the temperature below the BEC transition temperature.

7.4.1 Adiabatic Compression

The full evaporation sequence is given in table 7.1. Following loading into the TOP trap a multistage compression was carried out. As with the compression stage in the quadrupole potential, this compression must be carried out adiabatically, to conform to equation 7.5. During this ramp, the quadrupole field gradient and the TOP field are ramped simultaneously in order to keep the locus of field zero of the TOP trap far enough outside the atom cloud to avoid substantial evaporation. This is important since evaporation which occurs before the trapping frequencies have been maximised will be less efficient.

The aim in this compression ramp was to increase the elastic collision rate sufficiently to enter the runaway evaporation regime. The initial elastic collision rate in the TOP trap is $1.5\,\mathrm{s}^{-1}$. As discussed above, in order to enter the runaway evaporation regime for $\eta = 6$ we require a ratio of elastic to inelastic collisions, $R_{coll} = \Gamma_{el}\tau \sim 300$, and thus a value for the elastic collision rate, $\Gamma_{el} > 2.7\,\mathrm{s}^{-1}$. By the end of the compression ramp the collision rate had been increased to $\Gamma_{el} = 42\,\mathrm{s}^{-1}$, meaning that the runaway evaporation regime had been reached. The length of the compression ramp was found to be key to the final atom number in the condensate, with longer ramps giving a higher number.

7.4.2 Evaporation with the Field Zero

Following the adiabatic compression of the cloud, the value of the TOP bias field, B_T, was ramped down to increase the trapping frequencies and give a higher atom density and further increase the elastic collision rate. At the same time, the frequency of the evaporative RF was ramped down so that the RF cutting surface lay just outside the circle of death of the TOP trap. During this ramp, evaporation proceeded by atom loss at the locus of zero magnetic field and the value of the

Ramp	**Description**	**Duration (s)**	$\mathbf{B'_q(G\,cm^{-1})}$	$\mathbf{B_T(G)}$
1	RF evap. in quad.	10	771	-
2	Ramp down quad.	0.5	$771 \rightarrow 63$	-
3	Equilibrate in quad.	5	63	-
4	Load TOP trap	$\sim 100\,\mu$s	63	$0 \rightarrow 10.3$
5	TOP compression 1	5	$63 \rightarrow 309$	$10.3 \rightarrow 20.8$
6	TOP compression 2	5	$309 \rightarrow 424$	20.8
7	TOP compression 3	5	$424 \rightarrow 540$	20.8
8	$\lvert B\rvert = 0$ evap.	5	540	$20.8 \rightarrow 10.3$
9	RF evap. 1	5	540	10.3
10	RF evap. 2	1	$540 \rightarrow 170$	$10.3 \rightarrow 3.2$
11	RF evap. 3	2.5	170	3.2
Ramp	$\omega_\mathbf{r}/(\mathbf{2}\pi)\mathbf{(Hz)}$	$\mathbf{r_0(mm)}$	$\nu_\mathbf{RF}\mathbf{(MHz)}$	$\mathbf{r_{RF}/r_0}$
1	-	-	$120 \rightarrow 20$	-
2	-	-	-	-
3	-	-	-	-
4	6.2	3.3	-	-
5	$6.2 \rightarrow 21.6$	$3.3 \rightarrow 1.3$	-	-
6	$21.6 \rightarrow 29.7$	$1.3 \rightarrow 0.98$	-	-
7	$29.7 \rightarrow 37.8$	$0.98 \rightarrow 0.77$	$60 \rightarrow 40$	$3.1 \rightarrow 1.8$
8	$37.8 \rightarrow 53.5$	$0.77 \rightarrow 0.38$	$40 \rightarrow 15$	$1.8 \rightarrow 1.1$
9	53.5	0.38	$15 \rightarrow 8.5$	$1.1 \rightarrow 0.2$
10	$53.5 \rightarrow 30.2$	0.38 (approx. const)	$8.5 \rightarrow 4$	$0.2 \rightarrow 0.8$
11	30.2	0.38	$3.1 \rightarrow 2.5$	$0.4 \rightarrow 0.1$

Table 7.1: The parameters in the optimised evaporative cooling ramps used to produce a Bose-Einstein condensate.

truncation parameter was kept at around $\eta = 6$ to maximise the evaporation efficiency. This first evaporation stage increased the phase space density by a factor of approximately 20, with a decrease in atom number from 5.2×10^7 to 3.6×10^7.

7.4.3 RF Evaporation

Following the stage of cooling with the locus of field zero, the radius at which the RF is resonant with the atoms, r_{RF}, was brought inside the circle of death of the TOP trap. From this point on, the evaporation proceeded through RF evaporation alone, and the value of r_0 was kept fixed at 0.38 mm. The evaporation at this stage was well inside the runaway evaporation regime, giving a continually increasing elastic collision rate. This meant that the rate of cooling of the cloud could be increased, thereby reducing the losses due to inelastic collisions and increasing the evaporation efficiency. To this end, the ramp in RF frequency was split into multiple stages with the rate of reduction of the RF frequency increasing in each successive stage. The efficiency of each of the separate stages was optimised by adjusting the end parameters and the ramp rate to give the biggest increase in phase space density for a given decrease in atom number. At the same time, care was taken to ensure that the truncation parameter remained close to the optimum value, $\eta = 6$.

7.4.4 Observing the BEC transition

In a harmonic trap the transition to BEC occurs for a peak phase space density, $\rho(0) \simeq 2.61$. This transition point occurred at an RF frequency of approximately 2.95 MHz. At this frequency the cloud parameters were: $\rho(0) = 2.7$, $N = 2.2 \times 10^6$, and $T = 252$ nK. This temperature matches the value for the critical temperature predicted by equation 2.50, $T_c = 270$ nK, reasonably well.

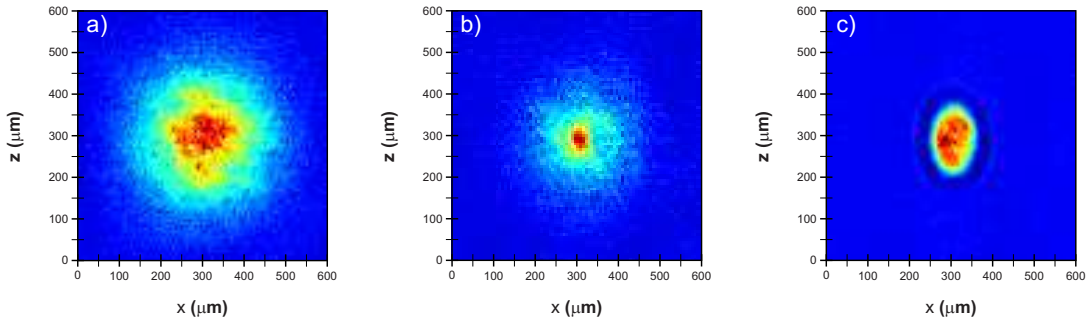

Figure 7.3: Absorption images of the atom cloud around the BEC transition in the final stages of RF evaporation in the TOP trap: a) At $T \sim T_c$ ($\nu_{RF} = 2.9\,\mathrm{MHz}$), b) at $T \sim 0.7T_c$ ($\nu_{RF} = 2.65\,\mathrm{MHz}$), and c) at $T < 0.5T_c$, ($\nu_{RF} = 2.5\,\mathrm{MHz}$). In all three shots the cloud was imaged after 24 ms time of flight. In a) the cloud is still thermal. In b) the onset of condensation is evidenced by the dense, condensed fraction surrounded by a more diffuse thermal component. Finally, in c) no discernible thermal component remains and the atoms are in a pure condensate with $N \sim 5.5 \times 10^5$.

The transition was evidenced by the appearance of a characteristic high density peak in the centre of the atom cloud surrounded by a lower density thermal fraction of atoms as the RF frequency was lowered below 2.8 MHz (see figure 7.3). The high density feature signifies the onset of macroscopic occupation of the ground energy state. Cutting further to 2.5 MHz gave a pure condensate of approximately 5.5×10^5 atoms, with no remaining thermal fraction. Quantum degeneracy was confirmed by the characteristic anisotropic expansion of the condensate when released from the trapping potential. The aspect ratio of the expanded condensate was inverted relative to the in-trap condensate, with the time-of-flight diameter largest in the more tightly confined axial direction (see figure 7.3 (c)). This should be contrasted with the isotropic expansion of a thermal cloud (shown in figure 7.3 (a)), and indicates that the expansion was dominated by the interactions within the condensate. In addition, the in-trap distribution of the atoms changed from gaussian to parabolic as the temperature was reduced below T_c, following the predictions of the mean-field theory outlined in subsection 2.4.4.

The final atom number in the pure condensate was relatively stable, typically

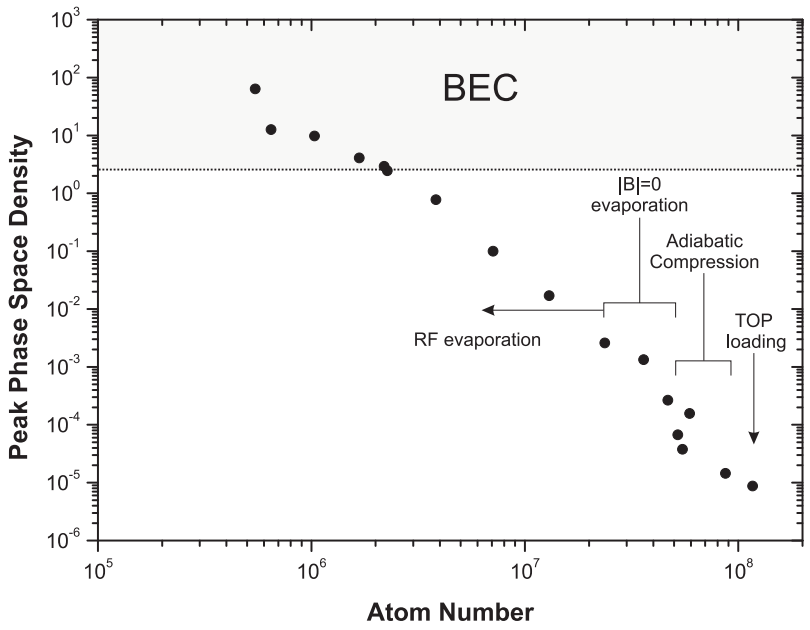

Figure 7.4: Peak phase space density versus atom number in the evaporative cooling ramps in the TOP trap.

varying by about $10-20\%$ between experimental runs. This variation was largely due to variations in the atom number initially loaded into the MOT.

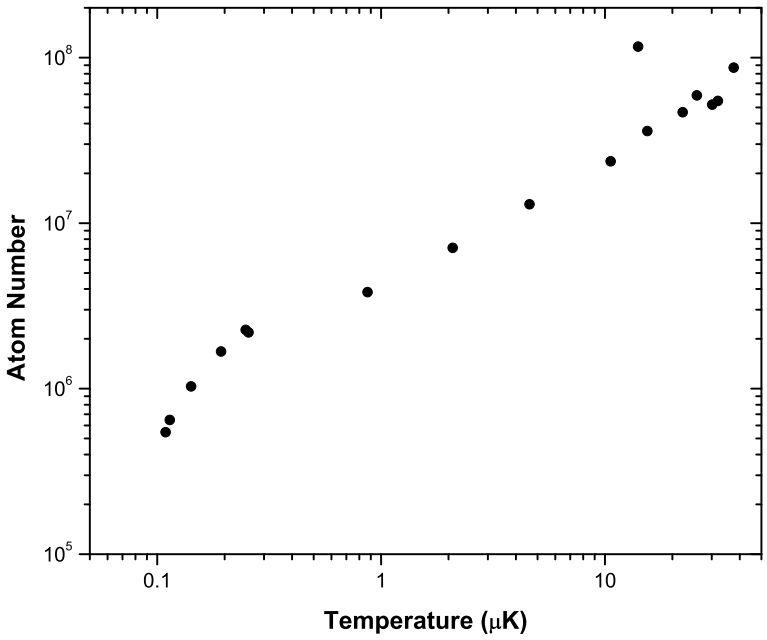

Figure 7.5: Atom number versus temperature in the evaporative cooling ramps in the TOP trap.

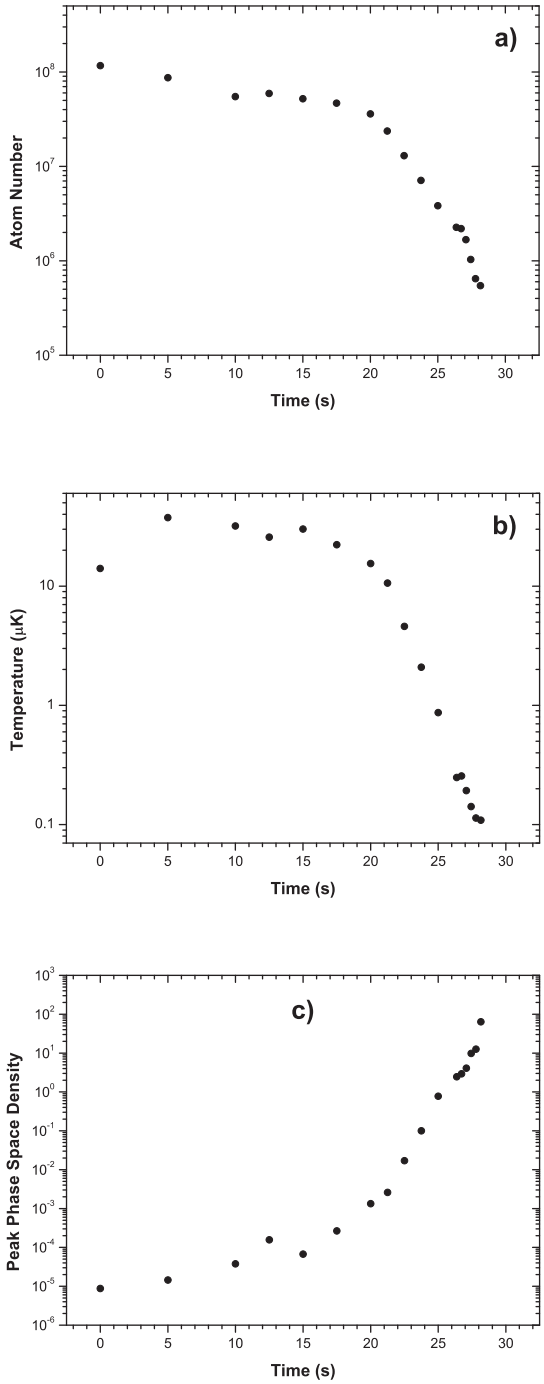

Figure 7.6: a) Atom number, b) temperature, and c) peak phase space density versus time in the evaporative cooling ramps in the TOP trap. The point at 0 s was taken just after loading into the TOP trap.

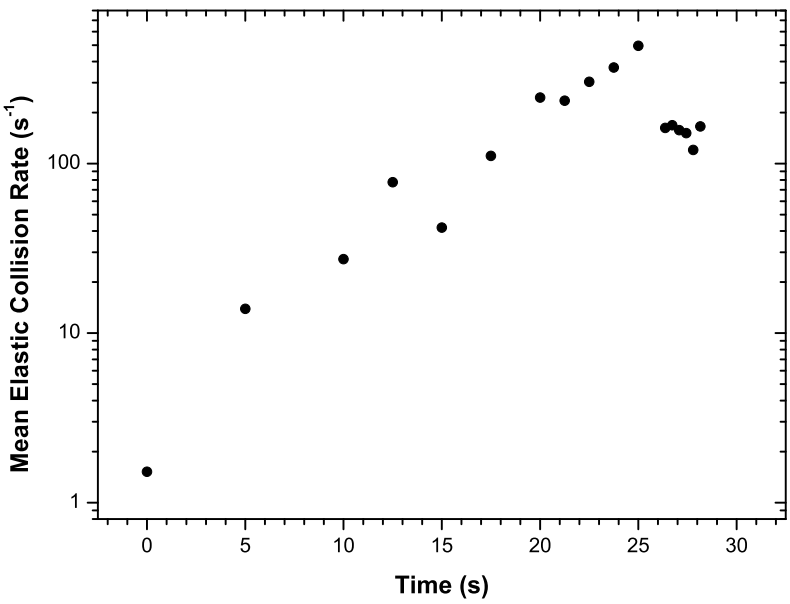

Figure 7.7: Mean elastic collision rate versus time during the evaporative cooling ramps in the TOP trap. The point at 0 s was taken just after loading into the TOP trap.

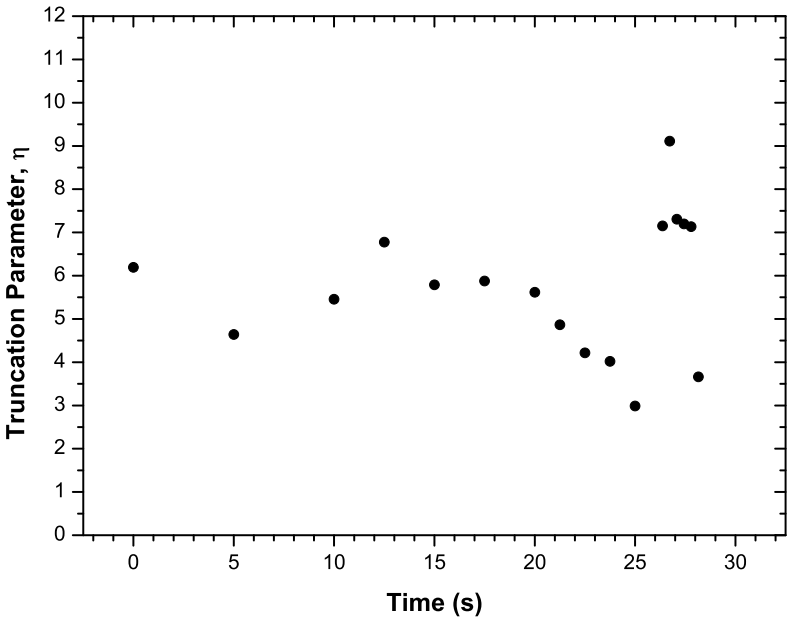

Figure 7.8: The truncation parameter, η, versus time during the evaporative cooling ramps in the TOP trap. The point at 0 s was taken just after loading into the TOP trap.

Chapter 8

Conclusions and Outlook

8.1 Summary

This thesis has presented the design, construction and optimisation of an apparatus to produce Bose-Einstein condensates. The key change from previous experiments is that the design includes a high resolution imaging system, capable of resolving single atoms. In order to incorporate this imaging system into the apparatus it was necessary to have a transport stage in which the atoms were moved $\sim 50\,\mathrm{cm}$ from the magneto-optical trap, where they were initially captured and cooled, to the final magnetic trap where the BEC is produced. In addition, several improvements were made to the final magnetic trap to increase the range of possible experiments; namely the maximum magnetic field gradient from the final trapping coils was increased and an optimised set of magnetic coils was included for creating RF-dressed potentials. The trapping configurations afforded by these versatile potentials make it possible to carry out experiments on low-dimensional quantum gases and on rapidly rotating BECs in which strongly correlated states emerge as

the condensate enters the fractional quantum Hall regime. A brief overview of the theory behind the rapid rotation experiment is given in section 8.2, along with an outline of the proposed implemetation in our apparatus. Below, concluding remarks on the separate components of the experiment are given.

Magneto-Optical Trap

The magneto-optical trap used in the apparatus involved a new design for our group: a pyramid MOT was used as the sole, main MOT. The atoms were then magnetically captured and transported out of the MOT to the science cell in a pair of moving anti-Helmholtz coils in the atom transport stage.

The optimised MOT could be loaded with around 3×10^9 atoms, in a loading time of 20 s. Approximately half this number of atoms – those in the $|\mathrm{F} = 1, m_F = -1\rangle$ magnetic substate – were then consistently captured in a purely magnetic trap prior to atom transport. The atom number loaded into the MOT was robust to small misalignments of the MOT input laser beam and the position of the centre of the magnetic field used to form the MOT. As a result, it has been possible to use the MOT for several months without the need for any major realignment. This robustness of operation makes the large pyramid design highly suitable as the source of ultracold atoms in an atom transport experiment.

A difficulty was encountered when optimising the stage of magnetic capture following MOT loading. The necessary rapid change in magnetic field caused eddy currents to be induced in the metal components surrounding the trapped atoms. These eddy currents produced rapid perturbations in the position of the atom cloud which resulted in heating of the atoms. We suspect that the site of the eddy currents was in the metal blocks used to mount the MOT mirrors. With this in mind, any future experiment which uses a pyramid MOT as the main MOT should

be made so that the mounting of the mirrors uses only non-conducting materials such as glass. A possible solution would be to use glass blocks that fit together into a pyramid, the surfaces of which could be coated to produce the MOT mirrors.

Atom Transport

Two methods of atom transport have been demonstrated in this thesis. The first used a pair of moving anti-Helmholtz coils to move the atoms the whole distance between the MOT and the science cell. The second used a hybrid approach where atoms were moved part of the distance in the moving coils and the rest by switching the current in a chain of fixed coils. This hybrid method was designed to provide optical access for the high resolution imaging system in the final configuration of the apparatus.

The optimised moving coils method allowed $\sim 30\%$ of the atoms initially magnetically captured from the MOT to be consistently transferred to the science cell (and it should be noted that the high optical density of the cloud in the final magnetic trap meant that this figure is likely to be an underestimate of the true fraction transported to the science cell). The atom number following transport was relatively insensitive to changes in the movement profile of the translation stage used to move the magnetic transport coils. The only significant finding was that the final atom number was larger for larger values of the acceleration and cruising velocity in this movement profile. We suspect that this is because at these larger values the atom cloud spends less time in the relatively bad vacuum inside the MOT chamber. An upper limit to the acceleration of the coils was imposed by unavoidable perturbations to the laser locking system caused by vibrations from the translation stage. The temperature of the transported atom cloud was found to be insensitive to the movement profile of the transport coils. The moving coils

method gave a final atom cloud with sufficiently high atom number and phase space density to produce a large BEC following evaporative cooling.

The second, hybrid transport system allowed $\sim$ 18% of the atoms initially magnetically captured from the MOT to be consistently transferred to the science cell. As yet, this system has not been thoroughly optimised, however, as a proof-of-principle demonstration has been used in conjunction with a stage of evaporative cooling to produce BEC. The next stages of experimental work will be to optimise this system further and install the high resolution imaging system.

Magnetic Trapping and BEC

The magnetic field gradient provided by the final trapping coils was made larger than in our previous experiments by using higher currents through the coils ($\sim$300 A) and by moving the coils closer to the atoms. The resulting maximum achievable axial quadrupole field gradient was around 800 G cm^{-1}; approximately double that in the previous experimental apparatus.

An RF evaporation sequence was employed which first cooled the atoms in a bare quadrupole potential before further cooling following loading of the atoms into a time-orbiting potential (TOP) trap. Around 1×10^8 atoms were consistently loaded into the TOP trap with a mean temperature and phase space density: $T = 20\,\mu$K, $\rho = 3 \times 10^{-6}$.

The optimised evaporative cooling sequence in the TOP trap lasted 28 s and allowed the consistent production of pure BECs with around 5×10^5 atoms in the $|\mathrm{F} = 1, m_F = -1\rangle$ magnetic substate. This atom number is around three times larger than in the old apparatus and reflects the increased efficiency of the evaporative cooling ramps afforded by the increased magnetic field gradient and trapping frequencies. This relatively large atom number in the BEC gives a good starting

condition for loading RF-dressed potentials.

RF-dressed Potentials

During the completion of this thesis, experimental work on the apparatus has continued and resulted in the successful formation of RF-dressed potentials. The first of these to be formed was the shell trap. The increased axial field gradient and the possibility of using different RF frequencies extends the scope of the RF experiments that can be carried out. In particular, it should now be possible to trap more atoms in the quasi-2D regime in the shell trap. In addition, it should be possible to enter the quasi-1D regime using the ring potential formed by dressing a biased quadrupole trap.

The first demonstration of the time-averaged adiabatic potential (TAAP) trap has also been made in our apparatus [95]. This scheme has been used to create both a double-well potential and a ring-shaped potential which were loaded with atoms at a temperature of approximately 700 nK. BEC has been achieved in the double-well potential by evaporatively cooling the atoms following loading into the potential. This new means of creating potentials will allow higher frequency trapping than previously achieved in purely magnetic potentials, and will be used in the rapid rotation experiment described below.

8.2 Rapidly Rotating Condensates: the Fractional Quantum Hall Regime

The majority of experiments done to date with BECs have operated in a regime in which the system is well approximated by mean-field theory. This theoretical approach gives good agreement with the general superfluid and collective properties

of BECs. However, there is an increasing interest in strongly correlated systems of ultracold bosonic gases in which a mean-field approach can no longer be used and a true many-body theory must be employed. These systems have been summarised in a recent review [118] and include the superfluid to Mott-insulator transition of atoms in an optical lattice [18] and the strongly correlated states which emerge upon rapid rotation of a BEC. Here, the second case is considered.

The rapid rotation of BECs results in states which are analogous to the fractional quantum Hall (FQH) states first observed in two-dimensional electron gases in semiconductors [119]. The controlled and relatively weakly-interacting nature of dilute gas condensates makes them theoretically accessible and thus rapidly rotating condensate experiments promise to give valuable insights into their condensed matter counterparts. In the following, the relevant background theory of rotating condensates is outlined followed by our proposed experimental scheme for rapidly rotating a BEC and observing the resulting strongly correlated states.

The superfluid nature of a BEC means that its response to rotation is fundamentally different from that of a classical fluid. The velocity of a superfluid is given by [104]:

$$\mathbf{v} = \frac{\hbar}{m}\nabla\phi \tag{8.1}$$

where ϕ is the phase of the condensate wavefunction. From this it can be seen that:

$$\nabla \times \mathbf{v} = 0. \tag{8.2}$$

Therefore the velocity field of a condensate is irrotational except where its order parameter is zero. As a result, unlike a classical fluid, a condensate does not undergo bulk rotational flow when its confining potential is rotated and instead can only gain angular momentum through the formation of vortices which are

lines of singularity in the velocity field around which the phase of the condensate wavefunction varies by multiples of 2π. The circulation, χ, of the velocity field around a closed contour is given by:

$$\chi = \oint \mathbf{v}.d\mathbf{l}. \tag{8.3}$$

This circulation is quantised in a superfluid, such that:

$$\chi = j\frac{h}{m} \tag{8.4}$$

where j is an integer. Above a critical rotation frequency the condensate gains an additional vortex for every additional unit of circulation imparted to it.

The detection of vortices in a BEC was one of the first confirmations of the superfluid nature of the condensate [120,121]. At high rotation rates, when several vortices are present in the condensate, they take on a triangular lattice formation [122], analogous to the Abrikosov lattice of flux lines in a type-II superconductor [123].

The rate of rotation of the condensate can be characterised by the *filling factor*, ν, which is the ratio of the number of atoms in the system to the number of vortices, N_v:

$$\nu = \frac{N}{N_v}. \tag{8.5}$$

At low rotation rates the filling factor is large, and the system is well approximated by the mean-field description of the Gross-Pitaevskii equation. The ground state of the system remains that of a BEC with a macroscopic wavefunction and the system forms a well-ordered vortex lattice. As the rotation rate is increased so that $\Omega_{rot} \rightarrow \omega_r$, the average angular momentum per particle becomes large compared to $\hbar$. A different description of the gas is then useful: the Landau level approach.

This approach demonstrates that a rapidily rotating neutral atom in a harmonic trap is equivalent to a charged particle in a uniform magnetic field, which can be appreciated by comparing the Hamiltonians of the two systems.

The Hamiltonian of a non-interacting neutral atom in a harmonic potential is modified in a frame rotating at an angular velocity, $\boldsymbol{\Omega_{rot}}$:

$$\begin{aligned} H_{\Omega_{rot}} &= H_0 - \boldsymbol{\Omega_{rot}}.\mathbf{L} && (8.6) \\ &= \frac{1}{2m}\left(\mathbf{p} - m\boldsymbol{\Omega_{rot}} \times \mathbf{r}\right)^2 + \frac{1}{2}m\left({\omega_r}^2 - \Omega_{rot}^2\right)(x^2+y^2) + \frac{1}{2}m\omega_z^2 z^2 && (8.7) \end{aligned}$$

In the limit $\Omega_{rot} \rightarrow \omega_r$, the centripetal term cancels the radial trapping so that the Hamiltonian resembles that of an electron in a magnetic field:

$$H = \frac{1}{2m}\left(\mathbf{p} + \frac{e}{2}\mathbf{B} \times \mathbf{r}\right)^2 = \frac{1}{2m}(\mathbf{p} + e\mathbf{A})^2 \qquad (8.8)$$

where the chosen magnetic vector potential $\mathbf{A} = \frac{1}{2}\mathbf{B} \times \mathbf{r}$. The simulation of a magnetic field is based on the equivalence $e\mathbf{B} \longleftrightarrow -2m\boldsymbol{\Omega_{rot}}$.

The eigenstates of $H_{\Omega_{rot}}$ form a series of near-degenerate single particle energy levels termed the Landau levels. Since, for $\Omega_{rot} \rightarrow \omega_r$, the radial trapping of the condensate is very small, the condensate spreads out in the $xy-$plane and its density drops. The condensate then approaches the quasi-2D regime (and hence z does not appear in equation 8.8). As a result, the interaction energy per particle is small compared to the gap between the Landau levels and therefore the system is typically in the lowest Landau level (LLL).

In a recent experiment at JILA, the LLL regime was attained in a condensate by rotating it at $> 99\%$ of the centrifugal limit [124]. In that experiment the typical filling factor was ~ 500. At this value of ν, and generally for $\nu \gg 1$, the condensate is in the mean-field LLL regime and contains an ordered vortex lattice.

As the filling factor is reduced to ~ 10 it is predicted that the vortex lattice will 'melt': quantum fluctuations in the condensate increase to the point where they destroy the vortex lattice [125, 126]. A reduction in the elastic shear modulus of the vortex lattice was observed for the lowest filling factors achieved in the JILA experiment indicating the onset of the melting of the vortex lattice.

For $\nu < 10$, the condensate can no longer be described using mean-field theory; it is predicted that following melting of the vortex lattice the condensate will undergo transitions to a series of strongly correlated vortex liquid states similar to the fermionic fractional quantum Hall (FQH) states observed in superconductors [125]. At very low filling factors; $\nu \sim 1$, a series of exotic states are predicted with quasiparticle excitations which obey fractional statistics, including the Laughlin state which is obtained when $\nu = 1/2$ [118]. The transitions to these strongly correlated states are of great interest since they are fundamentally different from typical phase transitions. The FQH states are not describable in terms of the standard theoretical explanations of traditional condensed matter physics such as long-range order and symmetry breaking. Instead, these states have a new kind of order, known as topological order, such that the degeneracy of the ground state depends on the topology of space.

An obvious difficulty with making $\Omega_{rot} \rightarrow \omega_r$ is that the lack of radial confinement will mean the atoms will fly out of the trap as a result of the unbalanced centrifugal force on the atoms. A solution is to apply a small non-harmonic trapping potential to the atoms. This was demonstrated in [127], where, through the addition of a blue-detuned laser beam, a small quartic component was added to the harmonic magnetic trapping potential. This approach allows the $\Omega_{rot} \sim \omega_r$ regime to be explored.

The intention in the new apparatus is to use the RF-dressed potentials outlined

in chapter 3 to confine the atoms during rapid rotation. As discussed in section 3.8, the RF shell potential may be time-averaged by applying a positional modulation in the radial plane, thereby increasing the radial confinement. In addition, by using appropriate RF parameters a quartic component can be added to the resulting potential. The barrier rotation scheme outlined in subsection 3.7.2 may then be used to spin-up the atoms to the $\Omega_{rot} \rightarrow \omega_r$ limit. The rate of rotation of the cloud may also be increased by applying evaporative RF to selectively remove atoms of higher than average energy but lower than average angular momentum.

A suitable scheme for imaging atoms in the FQH regime is primarily determined by the strict constraint on atom number required to reach this regime. This number can be estimated by considering the following limit for the breakdown of the mean-field regime and entry into the FQH regime [118]:

$$\frac{\omega_r - \Omega_{rot}}{\omega_r} < \frac{8a_s}{Na_z} \tag{8.9}$$

where $a_z = \sqrt{\hbar/m\omega_z}$ is the axial harmonic oscillator length.

The time-averaging in the TAAP trap smoothes out asymmetries in the trapping potential ensuring a high degree of cylindrical symmetry. The difference $\omega_x - \omega_y$ sets the lower limit for $\omega_r - \Omega_{rot}$. Assuming an asymmetry of 0.5%: $(\omega_r - \Omega_{rot})/\omega_r = 0.005$, and $\omega_r/2\pi = 200\,\mathrm{Hz}$, and $\omega_z/2\pi = 2000\,\mathrm{Hz}$, condition 8.9 becomes:

$$N < 33. \tag{8.10}$$

In addition to this constraint on number, the thermal energy of the atoms must be less than the chemical potential of the system to observe the quantum effects of the FQH regime. The 3D chemical potential was given in equation 2.62, and

this expression may be approximated by:

$$\mu \simeq \frac{\hbar^2 a_s}{m} \frac{N}{a_z N_v r_v^2} = \frac{\hbar \omega_r a_s \nu}{a_z} \tag{8.11}$$

where r_v is the vortex core radius. For the trapping parameters assumed above and for $\nu = 1$: $\mu \simeq 0.2\,\mathrm{nK}$. Since the required final atom number is so small, nanokelvin temperatures can be reached using the standard evaporative cooling techniques.

In order to image the required low atom number calculated above it will be necessary to use the high resolution imaging system outlined in subsection 5.8.3. This system will provide sufficiently high resolution and signal-to-noise for single atom imaging. As described in subsection 5.8.3, imaging will be achieved by ramping up a deep red-detuned lattice to trap and cool the atoms following rotation in the RF-dressed potential. The fluorescent light will then be captured using a high numerical aperture microscope objective. The strongly correlated states of the FQH regime can be detected by measuring their density distribution. For example, in the Laughlin state an anti-correlation between particles is predicted leading to a flat-topped distribution [128] as opposed to the inverted parabolic BEC distribution.

Bibliography

[1] A. Kastler. Optical methods of atomic orientation and of magnetic resonance. *J. Opt. Soc. Am.*, 47(6):460, 1957.

[2] W. Paul. Electromagnetic traps for charged and neutral particles. *Rev. Mod. Phys.*, 62(3):531, 1990.

[3] A. L. Migdall, J. V. Prodan, W. D. Phillips, T. H. Bergeman, and H. J. Metcalf. First observation of magnetically trapped neutral atoms. *Phys. Rev. Lett.*, 54(24):2596, 1985.

[4] T. H. Maiman. Stimulated optical radiation in ruby. *Nature*, 187(4736):493, 1960.

[5] T. W. Hänsch, I. S. Shahin, and A. L. Schawlow. High-resolution saturation spectroscopy of the sodium D lines with a pulsed tunable dye laser. *Phys. Rev. Lett.*, 27(11):707, 1971.

[6] T. W. Hänsch and A. L. Schawlow. Cooling of gases by laser radiation. *Opt. Commun.*, 13(1):68, 1975.

[7] D. J. Wineland and H. Dehmelt. Proposed $10^{14}\delta\upsilon < \upsilon$ laser fluorescence spectroscopy on T1+ mono-ion oscillator III. *Bull. Am. Phys. Soc.*, 20(4):637, 1975.

[8] W. D. Phillips and H. Metcalf. Laser deceleration of an atomic beam. *Phys. Rev. Lett.*, 48(9):596, 1982.

[9] S. Chu, L. Hollberg, J. E. Bjorkholm, A. Cable, and A. Ashkin. Three-dimensional viscous confinement and cooling of atoms by resonance radiation pressure. *Phys. Rev. Lett.*, 55(1):48, 1985.

[10] E. L. Raab, M. Prentiss, A. Cable, S. Chu, and D. E. Pritchard. Trapping of neutral sodium atoms with radiation pressure. *Phys. Rev. Lett.*, 59(23):2631, 1987.

[11] S. Bose. Plancks Gesetz und Lichtquantenhypothese. *Z. Phys.*, 26:178, 1924.

[12] A. Einstein. Quantentheorie des einatomigen idealen Gases. *Sitzungsber. Preuss. Akad. Wiss.*, 18–25:3, 1925.

[13] M. H. Anderson, J. R. Ensher, M. R. Matthews, C. E. Wieman, and E. A. Cornell. Observation of Bose-Einstein condensation in a dilute atomic vapor. *Science*, 269(5221):198, 1995.

[14] K. B. Davis, M.-O. Mewes, M. R. Andrews, N. J. van Druten, D. S. Durfee, D. M. Kurn, and W. Ketterle. Bose-Einstein condensation in a gas of sodium atoms. *Phys. Rev. Lett.*, 75(22):3969, 1995.

[15] C. C. Bradley, C. A. Sackett, J. J. Tollett, and R. G. Hulet. Evidence of Bose-Einstein condensation in an atomic gas with attractive interactions. *Phys. Rev. Lett.*, 75(9):1687, 1995. *ibid.* 79(6):1170, 1997.

[16] M. Greiner, C. A. Regal, and D. S. Jin. Emergence of a molecular Bose-Einstein condensate from a Fermi gas. *Nature*, 426(6966):537, 2003.

[17] C. A. Regal, M. Greiner, and D. S. Jin. Observation of resonance condensation of fermionic atom pairs. *Phys. Rev. Lett.*, 92(4):040403, 2004.

[18] M. Greiner, O. Mandel, T. Esslinger, T. W. Hänsch, and I. Bloch. Quantum phase transition from a superfluid to a Mott insulator in a gas of ultracold atoms. *Nature*, 415(6867):39, 2002.

[19] W. H. Heathcote, E. Nugent, B. T. Sheard, and C. J. Foot. A ring trap for ultracold atoms in an RF-dressed state. *New J. Phys.*, 10(4):043012, 2008.

[20] W. H. Heathcote. *A toroidal trap for ultracold atoms in a RF-dressed state.* D.Phil. thesis, University of Oxford, 2007.

[21] E. Nugent. *Novel traps for Bose-Einstein condensates.* D.Phil. thesis, University of Oxford, 2009.

[22] M. Greiner, I. Bloch, T. W. Hänsch, and T. Esslinger. Magnetic transport of trapped cold atoms over a large distance. *Phys. Rev. A*, 63(3):031401, 2001.

[23] P. N. Lebedev. Experimental examination of light pressure. *Ann. der Physik*, 6:433, 1901.

[24] E. F. Nichols and G. F. Hull. The pressure due to radiation (second paper). *Phys. Rev. (Series I)*, 17(1):26, 1903.

[25] C. Cohen-Tannoudji, J. Dupont-Roc, and G. Grynberg. *Atom-Photon Interactions: Basic Processes and Applications*. Wiley, New York, 1st edition, 1992.

[26] C. Cohen-Tannoudji, J. Dupont-Roc, and G. Grynberg. *Photons and atoms: introduction to quantum electrodynamics*. Wiley, New York, 1st edition, 1989.

[27] C. J. Foot. *Atomic Physics*. Oxford University Press, 1st edition, 2005.

[28] P. D. Lett, R. N. Watts, C. I. Westbrook, W. D. Phillips, P. L. Gould, and H. J. Metcalf. Observation of atoms laser cooled below the Doppler limit. *Phys. Rev. Lett.*, 61(2):169, 1988.

[29] P. D. Lett, W. D. Phillips, S. L. Rolston, C. E. Tanner, R. N. Watts, and C. I. Westbrook. Optical molasses. *J. Opt. Soc. Am. B*, 6(11):2084, 1989.

[30] J. Dalibard and C. Cohen-Tannoudji. Laser cooling below the Doppler limit by polarization gradients: simple theoretical models. *J. Opt. Soc. Am. B*, 6(11):2023, 1989.

[31] P. J. Ungar, D. S. Weiss, E. Riis, and S. Chu. Optical molasses and multilevel atoms: theory. *J. Opt. Soc. Am. B*, 6(11):2058, 1989.

[32] S. A. Hopkins and A. V. Durrant. Parameters for polarization gradients in three-dimensional electromagnetic standing waves. *Phys. Rev. A*, 56(5):4012, 1997.

[33] C. Salomon, J. Dalibard, W. D. Phillips, A. Clairon, and S. Guellati. Laser cooling of cesium atoms below 3 μk. *Europhys. Lett.*, 12(8):683, 1990.

[34] A. M. Steane, M. Chowdhury, and C. J. Foot. Radiation force in the magneto-optical trap. *J. Opt. Soc. Am. B*, 9(12):2142, 1992.

[35] H. J. Metcalf and P. van der Straten. *Laser cooling and trapping*. Springer, London, 1st edition, 1999.

[36] K. I. Lee, J. A. Kim, H. R. Noh, and W. Jhe. Single-beam atom trap in a pyramidal and conical hollow mirror. *Opt. Lett.*, 21(15):1177, 1996.

[37] C. Monroe, W. Swann, H. Robinson, and C. Wieman. Very cold trapped atoms in a vapor cell. *Phys. Rev. Lett.*, 65(13):1571, 1990.

[38] F. Reif. *Fundamentals of statistical and thermal physics*. McGraw-Hill Higher Education, New York, 1st edition, 1965.

[39] K. E. Gibble, S. Kasapi, and S. Chu. Improved magneto-optic trapping in a vapor cell. *Opt. Lett.*, 17(7):526, 1992.

[40] D. W. Sesko, T. G. Walker, and C. E. Wieman. Behavior of neutral atoms in a spontaneous force trap. *J. Opt. Soc. Am. B*, 8(5):946, 1991.

[41] K. Lindquist, M. Stephens, and C. Wieman. Experimental and theoretical study of the vapor-cell Zeeman optical trap. *Phys. Rev. A*, 46(7):4082, 1992.

[42] W. Petrich, M. H. Anderson, J. R. Ensher, and E. A. Cornell. Stable, tightly confining magnetic trap for evaporative cooling of neutral atoms. *Phys. Rev. Lett.*, 74(17):3352, 1995.

[43] C. G. Townsend, N. H. Edwards, C. J. Cooper, K. P. Zetie, C. J. Foot, A. M. Steane, P. Szriftgiser, H. Perrin, and J. Dalibard. Phase-space density in the magneto-optical trap. *Phys. Rev. A*, 52(2):1423, 1995.

[44] T. Walker, D. Sesko, and C. Wieman. Collective behavior of optically trapped neutral atoms. *Phys. Rev. Lett.*, 64(4):408, 1990.

[45] G. L. Gattobigio, T. Pohl, G. Labeyrie, and R. Kaiser. Scaling laws for large magneto-optical traps. *Physica Scripta*, 81(2):025301, 2010.

[46] G. Hillenbrand, K. Burnett, and C. J. Foot. Effect of scattered radiation on sub-Doppler cooling. *Phys. Rev. A*, 52(6):4763, 1995.

[47] M. Drewsen, Ph. Laurent, A. Nadir, G. Santarelli, A. Clairon, Y. Castin, D. Grison, and C. Salomon. Investigation of sub-Doppler cooling effects

in a cesium magneto-optical trap. *Applied Physics B: Lasers and Optics*, 59(3):283, 1994.

[48] W. Ketterle, K. B. Davis, M. A. Joffe, A. Martin, and D. E. Pritchard. High densities of cold atoms in a dark spontaneous-force optical trap. *Phys. Rev. Lett.*, 70(15):2253, 1993.

[49] C. G. Townsend, N. H. Edwards, K. P. Zetie, C. J. Cooper, J. Rink, and C. J. Foot. High-density trapping of cesium atoms in a dark magneto-optical trap. *Phys. Rev. A*, 53(3):1702, 1996.

[50] M. T. Depue, S. Lukman Winoto, D. J. Han, and D. S. Weiss. Transient compression of a MOT and high intensity fluorescent imaging of optically thick clouds of atoms. *Opt. Commun.*, 180(1–3):73, 2000.

[51] J. R. Ensher. *The First Experiments with Bose-Einstein Condensation of* ^{87}*Rb*. Ph.D. thesis, JILA, 1998.

[52] J. Arlt. *Experiments on Bose-Einstein condensation*. D.Phil. thesis, University of Oxford, 2000.

[53] G. Smirne. *Experiments with Bose-Einstein condensates in optical traps*. D.Phil. thesis, University of Oxford, 2005.

[54] A. Harsono. *Dipole trapping and manipulation of ultra-cold atoms*. D.Phil. thesis, University of Oxford, 2006.

[55] P. D. D. Schwindt. *Magnetic traps and guides for Bose-Einstein condensates on an atom chip: progress toward a coherent atom waveguide beamsplitter*. Ph.D. thesis, JILA, 2003.

[56] W. H. Wing. On neutral particle trapping in quasistatic electromagnetic fields. *Progress in Quantum Electronics*, 8(3–4):181, 1984.

[57] T. Bergeman, G. Erez, and H. J. Metcalf. Magnetostatic trapping fields for neutral atoms. *Phys. Rev. A*, 35(4):1535, 1987.

[58] D. E. Pritchard. Cooling neutral atoms in a magnetic trap for precision spectroscopy. *Phys. Rev. Lett.*, 51(15):1336, 1983.

[59] T. Esslinger, I. Bloch, and T. W. Hänsch. Bose-Einstein condensation in a quadrupole-Ioffe-configuration trap. *Phys. Rev. A*, 58(4):R2664, 1998.

[60] K. Huang. *Statistical Mechanics*. Wiley, New York, 2nd edition, 1987.

[61] V. Bagnato, D. E. Pritchard, and D. Kleppner. Bose-Einstein condensation in an external potential. *Phys. Rev. A*, 35(10):4354, 1987.

[62] F. Dalfovo, S. Giorgini, L. P. Pitaevskii, and S. Stringari. Theory of Bose-Einstein condensation in trapped gases. *Rev. Mod. Phys.*, 71(3):463, 1999.

[63] N. N. Bogoliubov. On the theory of superfluidity. *J. Phys. (Moscow)*, 11:23, 1947.

[64] E. P. Gross. Structure of a quantized vortex in boson systems. *Nuovo Cimento*, 20(3):454, 1961.

[65] L. P. Pitaevskii. Vortex lines in an imperfect Bose gas. *Sov. Phys. JETP*, 13:451, 1961.

[66] D. S. Petrov. *Bose-Einstein Condensation in Low-Dimensional Trapped Gases*. Ph.D. thesis, University of Amsterdam, 2003.

[67] J. M. Kosterlitz and D. J. Thouless. Ordering, metastability and phase transitions in two-dimensional systems. *J. Phys. C.*, 6:1181, 1973.

[68] V. L. Berenzinskii. Destruction of long-range order in one-dimensional and two-dimensional systems having a continuous symmetry group: II. Quantum systems. *Sov. Phys. JETP*, 34:610, 1972.

[69] D. S. Petrov, M. Holzmann, and G. V. Shlyapnikov. Bose-Einstein condensation in quasi-2D trapped gases. *Phys. Rev. Lett.*, 84(12):2551, 2000.

[70] T. P. Simula and P. B. Blakie. Thermal activation of vortex-antivortex pairs in quasi-two-dimensional Bose-Einstein condensates. *Phys. Rev. Lett.*, 96(2):020404, 2006.

[71] T. Esslinger and G. Blatter. Quantum physics – atomic gas in flatland. *Nature*, 441(7097):1053, 2006.

[72] D. J. Bishop and J. D. Reppy. Study of the superfluid transition in two-dimensional ^{4}He films. *Phys. Rev. Lett.*, 40(26):1727, 1978.

[73] D. J. Resnick, J. C. Garland, J. T. Boyd, S. Shoemaker, and R. S. Newrock. Kosterlitz-Thouless transition in proximity-coupled superconducting arrays. *Phys. Rev. Lett.*, 47(21):1542, 1981.

[74] A. I. Safonov, S. A. Vasilyev, I. S. Yasnikov, I. I. Lukashevich, and S. Jaakkola. Observation of quasicondensate in two-dimensional atomic hydrogen. *Phys. Rev. Lett.*, 81(21):4545, 1998.

[75] Z. Hadzibabic, P. Krüger, M. Cheneau, B. Battelier, and J. Dalibard. Berezinskii-Kosterlitz-Thouless crossover in a trapped atomic gas. *Nature*, 441(7097):1118, 2006.

[76] P. Krüger, Z. Hadzibabic, and J. Dalibard. Critical point of an interacting two-dimensional atomic Bose gas. *Phys. Rev. Lett.*, 99(4):040402, 2007.

[77] P. Cladé, C. Ryu, A. Ramanathan, K. Helmerson, and W. D. Phillips. Observation of a 2D Bose gas: From thermal to quasicondensate to superfluid. *Phys. Rev. Lett.*, 102(17):170401, 2009.

[78] V. Schweikhard, S. Tung, and E. A. Cornell. Vortex proliferation in the Berezinskii-Kosterlitz-Thouless regime on a two-dimensional lattice of Bose-Einstein condensates. *Phys. Rev. Lett.*, 99(3):030401, 2007.

[79] W. Ketterle and N. J. van Druten. Bose-Einstein condensation of a finite number of particles trapped in one or three dimensions. *Phys. Rev. A*, 54(1):656, 1996.

[80] B. Paredes, A. Widera, V. Murg, O. Mandel, S. Fölling, I. Cirac, G. V. Shlyapnikov, T. W. Hänsch, and I. Bloch. Tonks-Girardeau gas of ultracold atoms in an optical lattice. *Nature*, 429(6989):277, 2004.

[81] A. Görlitz, J. M. Vogels, A. E. Leanhardt, C. Raman, T. L. Gustavson, J. R. Abo-Shaeer, A. P. Chikkatur, S. Gupta, S. Inouye, T. Rosenband, and W. Ketterle. Realization of Bose-Einstein condensates in lower dimensions. *Phys. Rev. Lett.*, 87(13):130402, 2001.

[82] N. L. Smith, W. H. Heathcote, G. Hechenblaikner, E. Nugent, and C. J. Foot. Quasi-2D confinement of a BEC in a combined optical and magnetic potential. *J. Phys. B*, 38(3):223, 2005.

[83] O. Zobay and B. M. Garraway. Two-dimensional atom trapping in field-induced adiabatic potentials. *Phys. Rev. Lett.*, 86(7):1195, 2001.

[84] T. Schumm, S. Hofferberth, L. M. Andersson, S. Wildermuth, S. Groth, I. Bar-Joseph, J. Schmiedmayer, and P. Krüger. Matter-wave interferometry in a double well on an atom chip. *Nature Physics*, 1(1):57, 2005.

[85] S. Hofferberth, I. Lesanovsky, B. Fischer, J. Verdu, and J. Schmiedmayer. Radiofrequency-dressed-state potentials for neutral atoms. *Nature Physics*, 2(10):710, 2006.

[86] Ph. W. Courteille, B. Deh, J. Fortagh, A. Guenther, S. Kraft, C. Marzok, S. Slama, and C. Zimmermann. Highly versatile atomic micro traps generated by multifrequency magnetic field modulation. *Jour. Phys. B*, 39(5):1055, 2006.

[87] T. Fernholz, R. Gerritsma, P. Krüger, and R. J. C. Spreeuw. Dynamically controlled toroidal and ring-shaped magnetic traps. *Phys. Rev. A*, 75(6):063406, 2007.

[88] A. J. Leggett. Superfluidity. *Rev. Mod. Phys.*, 71(2):S318, 1999.

[89] L. D. Landau. Zur Theorie der Energieübertragung II. *Phys. Z. Sowjetunion*, 2:46, 1932.

[90] C. Zener. Non-adiabatic crossing of energy levels. *Proceedings of the Royal Society of London, Series A*, 137(833):696, 1932.

[91] Y. Colombe, E. Knyazchyan, O. Morizot, B. Mercier, V. Lorent, and H. Perrin. Ultracold atoms confined in rf-induced two-dimensional trapping potentials. *Europhys. Lett.*, 67(4):593, 2004.

[92] O. Morizot, Y. Colombe, V. Lorent, H. Perrin, and B. M. Garraway. Ring trap for ultracold atoms. *Phys. Rev. A*, 74(2):023617, 2006.

[93] C. Ryu, M. F. Andersen, P. Cladé, Vasant Natarajan, K. Helmerson, and W. D. Phillips. Observation of persistent flow of a Bose-Einstein condensate in a toroidal trap. *Phys. Rev. Lett.*, 99(26):260401, 2007.

[94] I. Lesanovsky and W. von Klitzing. Time-averaged adiabatic potentials: Versatile matter-wave guides and atom traps. *Phys. Rev. Lett.*, 99(8):083001, 2007.

[95] M. Gildemeister, E. Nugent, B. E. Sherlock, M. Kubasik, B. T. Sheard, and C. J. Foot. Trapping ultracold atoms in a time-averaged adiabatic potential. *Phys. Rev. A*, 81(3):031402, 2010.

[96] M. A. Kasevich, E. Riis, S. Chu, and R. G. DeVoe. RF spectroscopy in an atomic fountain. *Phys. Rev. Lett.*, 63(6):612, 1989.

[97] C. J. Myatt, N. R. Newbury, R. W. Ghrist, S. Loutzenhiser, and C. E. Wieman. Multiply loaded magneto-optical trap. *Opt. Lett.*, 21(4):290, 1996.

[98] M. J. Renn, D. Montgomery, O. Vdovin, D. Z. Anderson, C. E. Wieman, and E.A. Cornell. Laser-guided atoms in hollow-core optical fibers. *Phys. Rev. Lett.*, 75(18):3253, 1995.

[99] K. Gibble, S. Chang, and R. Legere. Direct observation of s-wave atomic collisions. *Phys. Rev. Lett.*, 75(14):2666, 1995.

[100] H. Lewandowski. *Coherences and correlations in an ultracold Bose gas*. Ph.D. thesis, JILA, 2002.

[101] T. L. Gustavson, A. P. Chikkatur, A. E. Leanhardt, A. Görlitz, S. Gupta, D. E. Pritchard, and W. Ketterle. Transport of Bose-Einstein condensates with optical tweezers. *Phys. Rev. Lett.*, 88(2):020401, 2001.

[102] M. E. Gehm, K. M. O'Hara, T. A. Savard, and J. E. Thomas. Dynamics of noise-induced heating in atom traps. *Phys. Rev. A*, 58(5):3914, 1998.

[103] M. Theis. *Optical Feshbach resonances in a Bose-Einstein condensate*. Ph.D. thesis, Innsbruck University, 2005.

[104] C. J. Pethick and H. Smith. *Bose-Einstein condensation in dilute gases*. Cambridge University Press, 2nd edition, 2008.

[105] E. A. Burt, R. W. Ghrist, C. J. Myatt, M. J. Holland, E. A. Cornell, and C.E. Wieman. Coherence, correlations, and collisions: What one learns about Bose-Einstein condensates from their decay. *Phys. Rev. Lett.*, 79(3):337, 1997.

[106] J. M. Goldwin. *Quantum degeneracy and interactions in the ^{87}Rb – ^{40}K Bose-Fermi mixture*. Ph.D. thesis, JILA., 2005.

[107] N. S. Harris. *Modern vacuum practice*. McGraw-Hill, 1st edition, 1989.

[108] R. K. Raj, D. Bloch, J. J. Snyder, G. Camy, and M. Ducloy. High-frequency optically heterodyned saturation spectroscopy via resonant degenerate four-wave mixing. *Phys. Rev. Lett.*, 44(19):1251, 1980.

[109] J. H. Shirley. Modulation transfer processes in optical heterodyne saturation spectroscopy. *Opt. Lett.*, 7(11):537, 1982.

[110] Linear Positioners Documentation. Parker-Hannifin.
url: www.parker.com/support/product_manuals/404xr_406xr_manual.pdf.

[111] G. Zürn. Project report, University of Oxford, High current control for magnetic transport of cold atoms, 2008.

[112] B. Fletcher. *A rotating optical lattice for ultracold atoms*. D.Phil. thesis, University of Oxford, 2008.

[113] Y. Castin and R. Dum. Bose-Einstein condensates in time dependent traps. *Phys. Rev. Lett.*, 77(27):5315, 1996.

[114] H. J. Lewandowski, D. M. Harber, D. L. Whitaker, and E. A. Cornell. Simplified system for creating a Bose-Einstein condensate. *Journal of Low Temperature Physics*, 132(5-6):309, 2003.

[115] W. Ketterle and N. J. VanDruten. Evaporative cooling of trapped atoms. *Advances in Atomic, Molecular, and Optical Physics*, 37:181, 1996.

[116] W. Ketterle, D. S. Durfee, and D. M. Stamper-Kurn. Making, probing and understanding Bose-Einstein condensates. *Proceedings of the Enrico Fermi International School of Physics*, 140:67, 1999.

[117] E. Hodby. *The superfluid properties of a Bose-Einstein condensed gas*. D.Phil. thesis, University of Oxford, 2002.

[118] I. Bloch, J. Dalibard, and W. Zwerger. Many-body physics with ultracold gases. *Rev. Mod. Phys.*, 80(3):885, 2008.

[119] D. C. Tsui, H. L. Stormer, and A. C. Gossard. Two-dimensional magnetotransport in the extreme quantum limit. *Phys. Rev. Lett.*, 48(22):1559, 1982.

[120] M. R. Matthews, B. P. Anderson, P. C. Haljan, D. S. Hall, C. E. Wieman, and E. A. Cornell. Vortices in a Bose-Einstein condensate. *Phys. Rev. Lett.*, 83(13):2498, 1999.

[121] K. W. Madison, F. Chevy, W. Wohlleben, and J. Dalibard. Vortex formation in a stirred Bose-Einstein condensate. *Phys. Rev. Lett.*, 84(5):806, 2000.

[122] J. R. Abo-Shaeer, C. Raman, J. M. Vogels, and W. Ketterle. Observation of vortex lattices in Bose-Einstein condensates. *Science*, 292(5516):476, 2001.

[123] J. F. Annett. *Superconductivity, superfluids and condensates.* Oxford University Press, 1st edition, 2004.

[124] V. Schweikhard, I. Coddington, P. Engels, V. P. Mogendorff, and E. A. Cornell. Rapidly rotating Bose-Einstein condensates in and near the lowest Landau level. *Phys. Rev. Lett.*, 92(4):040404, 2004.

[125] N. R. Cooper, N. K. Wilkin, and J. M. F. Gunn. Quantum phases of vortices in rotating Bose-Einstein condensates. *Phys. Rev. Lett.*, 87(12):120405, 2001.

[126] J. Sinova, C. B. Hanna, and A. H. MacDonald. Quantum melting and absence of Bose-Einstein condensation in two-dimensional vortex matter. *Phys. Rev. Lett.*, 89(3):030403, 2002.

[127] V. Bretin, S. Stock, Y. Seurin, and J. Dalibard. Fast rotation of a Bose-Einstein condensate. *Phys. Rev. Lett.*, 92(5):050403, 2004.

[128] N. R. Cooper, F. J. M. van Lankvelt, J. W. Reijnders, and K. Schoutens. Quantum Hall states of atomic Bose gases: density profiles in single-layer and multilayer geometries. *Phys. Rev. A*, 72(6):063622, 2005.